Carnegie Mellon University
MELLON COLLEGE OF SCIENCE

THESIS

SUBMITTED IN PARTIAL FULFILLMENT OF THE REQUIREMENTS
FOR THE DEGREE OF

DOCTOR OF PHILOSOPHY IN THE FIELD OF PHYSICS

TITLE: **"**Coalescence of sessile drops: the role of gravity, interfacial tension and surface wettability."

PRESENTED BY: Ying Zhang

ACCEPTED BY THE DEPARTMENT OF PHYSICS

STEPHEN GAROFF	5/12/16
STEPHEN GAROFF, CHAIR PROFESSOR	DATE

STEPHEN GAROFF	5/12/16
STEPHEN GAROFF, DEPT HEAD	DATE

APPROVED BY THE COLLEGE COUNCIL

FRED GILMAN	5/12/16
FRED GILMAN, DEAN	DATE

CARNEGIE MELLON UNIVERSITY

COALESCENCE OF SESSILE DROPS: THE ROLE OF GRAVITY, INTERFACIAL TENSIONS AND SURFACE WETTABILITY

Submitted in partial fulfillment of the requirements for
the degree of
Doctor of Philosophy
in
the Department of Physics

Ying Zhang

B.S., Physics, University of Science and Technology of China

M.S., Physics, Carnegie Mellon University

Acknowledgments

I would first like to thank my thesis advisors, Professor Stephen Garoff and Professor Shelley Anna. Without their patience, guidance and help, I would not be able to achieve the goals that I dreamt of. In the fourth year, when I was lost in the pursuit of thesis research, Prof. Garoff spent half an hour every day to discuss questions and push me forward. I am grateful for his nerdy features driven by curiosity and devotion to help students, otherwise I would have owed him tons of consultation fees. Prof. Anna have always provided significant high level insights into the research, making us two diligent aimless physics ants on a surface to see the third dimensional path towards the engineering goal. This interdisciplinary approach is the best learning experience that I have ever had.

My gratitude goes to my committee members, Professor Lynn Walker and Professor Michael Widom. I really appreciate the WAG group meeting and journal club, especially Prof. Walker's random comments teasing Viet Lam and Nick Alvarez. Her questions in a joking way illustrates that research can be rational, fun and not serious at the same time. I tried so hard to come up with the jokes in the WAG meeting to mimic her with the aim that other people would also enjoy casual research. I also thank Prof. Widom who supplemented some serious research critique along the thesis. Both elements are greatly appreciated.

I have been very fortunate and received a lot of help from other professors and instructors at

CMU. Prof. Annette Jacobson, Prof. Susana Steppan have taught me CPS laboratory techniques and carefully provided feedback on my lab reports. Rosemary Frollini has maintained the CPS lab for students to perform experiments. A concrete part of my thesis research is attributed to all these CPS lab techniques. I would also like to thank Prof. Dominique Chatain, who taught me the Surface Evolver stimulation tools and guided me on the static configuration of sessile drops.

This work is partially supported by the National Science Foundation – United States (Grant No. CBET-1264552) and the Physics Department at Carnegie Mellon University.

It was an honor to meet and work with many colleague and friends at CMU: Ramankur Sharma, Amsul Khanal, Amy Stetten, Stephen Iasella, John Liow, Chris Nelson, Sharon Vuong, Anthony Kotula, Nick Alvarez and others. The visiting students from Darmstadt have added some extra diversity: Xiang Wang and Marcus Lopes. I also want to thank those undergraduate students who have worked in the group: Heidi Miller, Colin Richards, Ben Marinoff, Andrew Kojzar, Justin Yi, Kaomi Hashimoto. Professor Roni Rosenfeld introduced me to a lot of interesting ideas about social science and life.

Besides the thesis work, I really want to thank my friends in the Physics Department, who have shared part of the life journeys together with me. Special thanks go to Will Levine, who was my roommate for four years and educated me a lot about life, socialism, law and politics. Robert Haussman shared with me his wisdom to deal with gloomy days. I thank Dao Ho, Zhen Tang, Udom Sae-Ueng, Yutaro Iiyama, Yu Feng, Huizhong Xu, Patrick Mende and others for all

the memories of the golden days.

Finally, I would like to express my gratitude to my family, for being supportive regarding my decisions. My father worked in Africa for ten years to earn me a better education. My mother worked as a bricklayer to set an example that all stereotypes can be overcome by hardworking and determination. I am also very thankful for my grandparents for raising me up. I am very proud that my family members value education so much despite lacking proper education themselves.

Thank you again to everyone above and numerous helping people that I have missed.

Abstract

Coalescence of liquid drops is important in many natural and industrial processes, such as raining, inkjet printing and coating applications. The coalescence for sessile drops is more complicated due to the additional interplay between the drops and solid surface. This work examines the impact of gravity, interfacial tensions and wetting properties on both the static and dynamic aspects of the coalescence of sessile drops. In the presence of gravity, seven dimensionless parameters are identified to describe the axisymmetric configuration of a compound sessile drop after coalescence. A stability criterion is established based on the perturbation of Laplacian shape and the stability criterion is numerically evaluated in the zero Bond number limit. Surface Evolver simulations and experiments are performed for compound sessile drops at small and intermediate Bond numbers. Both simulations and experiments agree closely with the zero Bond number analysis, exhibiting a small discrepancy at intermediate Bond number. For the dynamics of sessile drop coalescence, experiments are performed for miscible fluids with similar surface tensions but different densities and viscosities. The coalescence behavior shows three distinctive stages with well separated timescales: an initial stage of fast bridge healing process, an intermediate stage of advective motion for fluids with different densities, and a final stage of diffusion. A dimensional analysis shows that the flow behavior for the advective motion resembles gravity current. A more detailed analytical model based on the lubrication approximation is conducted and demonstrates good qualitative agreement with the advective motion during the sessile drop coalescence.

Table of Contents

List of Tables

List of Figures

Chapter 1 Introduction

The field of capillarity, created in the first half of 19th century by Laplace and Young, studies the interfaces between two immiscible liquids or between a gas and a liquid.[1] Among the research subjects in capillarity, droplets are of significant interest to scientists and engineers because of their ubiquitous appearance in natural processes (raining, misting, skin dewetting, etc.) and industrial applications (pesticide spraying, combustion, etc.).[1–3] The static behaviors of liquid droplets were well modeled by theories of capillarity based on thermodynamics and statistical mechanics starting from the early 20th century.[4] The dynamic aspects of droplets have been examined more extensively since the advent of microfluidics research in the 1980s,[5, 6] when high-speed imaging techniques began to impact the study of experimental fluid mechanics.[7] The development of microfluidics was driven by the promise of large-scale automated chemistry and biology experiments to investigate processes such as the reaction kinetics and protein folding,[6, 8] in which reagents are consumed with high efficiency.[6, 9] Realization of large-scale automated experiments relies on a good understanding of both the formation[10–13] and coalescence[14–18] of drops.

The physics of two drops adds a new feature to the drop coalescence: the two drops can be either of the same liquid or different liquids (different liquids can be either miscible or immscible). When two drops composed of the same liquid contact, a fused drop is formed to reduce the total surface energy. However, when two immiscible drops contact, three different configurations can be formed depending on the three interfacial tensions; the three possible configurations are complete engulfing, partial engulfing and non-engulfing.[19–21] More interestingly, when two miscible sessile drops contact, even though the final static configuration

is a fused drop of uniform composition, the dynamics process to achieve the final configuration can be either fast or delayed, depending on the difference in surface tensions.[28–32] These different phenomena associated with two drops motivate us to study both the static and dynamic aspects of drop coalescence.

In this thesis, we focus on the coalescence of sessile drops, where drops are in contact with solid surfaces. Sessile drops allow well-controled drop sizes and positions while contact line dynamics add complexity to the coalescence.[22, 23] Both the statics and dynamics of a single drop in contact with a solid surface have been well studied and are summarized in review articles by de Gennes[24] and Bonn *et al*.[25] Since miscible drop coalescence yields a well-modeled final static configuration of a single drop, we first study the static stability of the configuration formed after the coalescence of two immiscible drops. Next we study the fluid flow during the coalescence of sessile drops of miscible liquids and eaxmine whether the dynamics lead to an advective motion within the merging drop beyond simple diffusion.

The first comprehensive analysis of the static configuration of a compound drop formed by coalescing two immiscible drops within another ambient immiscible phase was performed by Torza and Mason in the 1970s under the assumption of negligible gravity effects.[19] Other experiments and analyses studying compound drop configurations are summarized in the review article by Johnson *et al*.[20] and in the book by Sahdal *et al*.[21]

Since 2002, Mahadevan *et al*. and Neeson *et al*. proposed and analyzed different configurations of compound sessile drops, where another solid phase was added to the problem of compound drops.[26, 27] However, in these two papers, the configurations of compound sessile drops are also modeled in the absence of gravity, such that the calculations of geometric relations

are significantly simplified as all fluid/fluid interfaces have spherical cap shapes.

Neglecting gravity limits stability analysis of static configurations of compound sessile drops: all configurations are possible without preference to any orientation. But this is contradicted by a survey of the literature: in air, no static observation was ever made of a fluid drop resting on top of another drop, where the lower drop is in direct contact with a solid surface. A stability analysis of compound sessile drops therefore needs to be performed in the presence of gravity. In a different geometric configuration where the lower drop is extended to a bulk fluid, the phenomenon of a less dense drop floating on top of a more dense bulk liquid is ubiquitous in nature; and even observations of more dense drops floating on top of a less dense bulk liquid are made.[33, 34] A natural question arises, how is the concept of "floatability" revised when the lower bulk liquid is reduced to a sessile drop. This leads us to study the stability of an axisymmetric compound sessile drop, where gravity breaks the rotational symmetry, and the finite size of the lower drop breaks the translational symmetry.

Chapter 2 examines the stability of axisymmetric compound sessile drops in the presence of gravity. We first study the controlling parameters for the equilibrium configuration. Based on a perturbation approach, a stability criterion is determined in the limit of small drop sizes. This analysis suggests a possible realization of a stable axisymmetric compound sessile drop in air. The stability analysis of axisymmetric compound sessile drops contrasts with the concept of floatability on bulk fluid at a large scale. Through both simulations and experiments, we verify the stability criterion and show the transition from a stable configuration to an unstable configuration by tuning the density ratio of the two drops.

Though the extensive study on the static configuration of coalesced drops started in the 1970s,[19–21] research on the dynamic aspects of drop coalescence has lagged behind by almost 30 years, which is partly attributed to the lack of digital imaging technology.[7, 18] In spite of the considerable research in sessile drop coalescence during the past two decades, there are still many unanswered questions, e.g. the effects of the fluid properties and geometric parameters are not well understood.[18]

In Chapter 3, we examine how the flow during the sessile drop coalescence is affected by the fluid densities and viscosities. The density difference between two drops introduces an advective motion, dominating the effect of diffusion. By carefully varying the densities and viscosities of the fluid drops, we establish a scaling relation for the advective motion which agrees with the experimental observations. This scaling relation agrees with the physics of gravity currents[35–38], examples of gravity current including snow avalanches, sandstorms and the spreading of oil on the sea surface, which is typically observed at a much larger length scale. We compare simulations based on the gravity current model with observed fluid flow during drop coalescence. This gravity current model agrees qualitatively with the internal flow during the drop coalescence for different density fluids.

Chapter 2 Axisymmetric Compound Sessile Drop[1]

2.1 Introduction

The sessile drop problem, which determines the configuration of a fluid drop deposited on a horizontal solid surface, is governed by the Laplace equation. The numerical and asymptotic solutions to sessile drop configurations are well studied and further used to measure surface tensions of various fluids[39, 40]. If the lower solid surface is replaced by another fluid phase, the resulting configuration is a sessile lens. Pujado and Scriven examined both translationally symmetric and rotationally symmetric sessile lenses using numerical methods and approximate analytical solutions[41]. Contrary to sessile drops with Young's contact angle, the three interfacial tensions of a sessile lens at a liquid/liquid interface form a closed Neumann's triangle[41–43]. Furthermore, in sessile lens cases, typical observations are made for systems with subphases denser than the deposited drops to maintain the floatability condition. Recently, Phan *et al.* showed experimentally that more dense drops can float on less dense liquids for two different systems (water/oil, water/oil with surfactant) due to the distortion of fluid interfaces[33, 34]. Reduction of the lower fluid phase to a finite size drop breaks the translational symmetry of a sessile lens configuration, resulting in a different geometry called a compound drop[19].

A compound drop is typically produced when two immiscible drops are submerged in another ambient external fluid medium (air or another liquid). If one of the immiscible drops is in contact with a solid surface, the resulting configuration is then denoted as a compound sessile drop[26, 27, 44]. Neeson *et al.* experimentally realized a compound sessile drop with a tetradecane

[1] The contents of this chapter are based on a manuscript submitted to Journal of Colloid and Interface Science by Ying Zhang, Dominique Chatain, Stephen Garoff and Shelley L. Anna (2015)

drop on top of a perfluorooctane drop, with the lower drop in contact with a hydrophobic glass surface under water. This experimental realization utilized the flotation property; tetradecane is less dense than the ambient medium of water, preventing the tetradecane drop from sliding off the axisymmetric position[27]. However, a stable configuration was never reported in literature if both the immiscible drops are more dense than the ambient medium.

A question naturally arises: is it possible for other systems with two drops, both more dense than the ambient phase (e.g. air), to form a stable axisymmetric compound sessile drop? In this chapter, we first derive equations for the equilibrium configuration, and then present a stability criterion for forming an axisymmetric compound sessile drop. The analysis is further supplemented by Surface Evovler simulations and experimental verifications based on both high and low interfacial tension fluids.

2.2 Preliminaries and Related Work

2.2.1 Geometric configurations of compound drops in the absence of gravity

Earlier results on compound drops provide a fundamental understanding about compound sessile drop configurations, which has at least one drop in contact with the solid surface. Compound drops are typically observed in multiple drop processes in flow-focusing devices[45, 46], where the configuration was solved with the spherical cap shape assumption[19, 20].

Torza and Mason derived compound drop shapes in the absence of gravity in the 1970s, which were rederived by Mahadevan *et al*. and Neeson *et al*. independently about 30 years later[19, 26, 27]. As the derivation for the compound drop in Torza and Mason's paper is much more comprehensive, we here reproduce some of the geometric relations relevant for the calculation of stability of compound sessile drop in the next few sections. The notations may be slightly

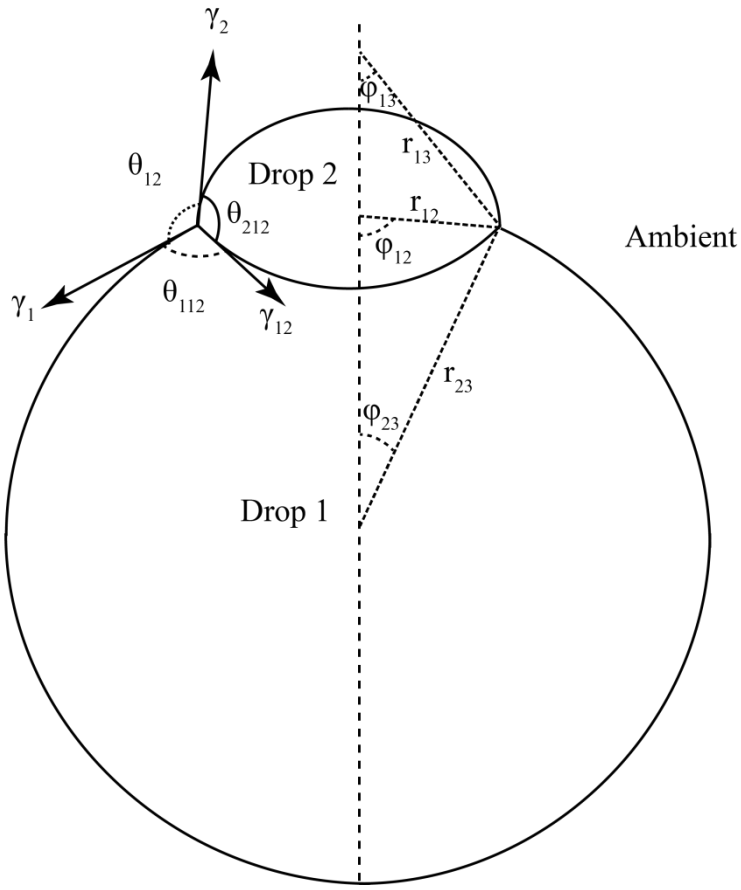

Figure 2.1 The configuration of a compound drop in the absence of gravity. The two drops denoted by Drop 1 and Drop 2 are in contact with each other and surrounded by another immiscible ambient phase. All the three interfaces are spherical caps. Interfacial tensions at the three phase contact line follows Neumann's triangle rule.

different from Torza and Mason's original paper[19].

As illustrated in Figure 2.1, Drop 1 and Drop 2 are in contact and are submerged in another ambient phase, with solid lines indicating the interfaces between different phases. Without gravity effects, all the three interfaces for compound drops are spherical caps such that the static configuration has minimum surface energy. The surface tensions of Drop 1 and Drop 2 are denoted by γ_1 and γ_2 respectively, while the interfacial tension between the two drops is denoted by γ_{12}. The radii of curvature for the Drop 2 surface, the Drop 1 surface and the

interface between Drop 2 and Drop 1 are r_{12}, r_{23} and r_{13} respectively, while the radii from the three phase contact line form three angles with the center line, $\varphi_{12}, \varphi_{23}$ and φ_{13}. The chord length of the intersecting spheres is denoted by $d = 2R$. The simple geometric relation by projecting the radii of curvature to the chord line yields,

$$r_{13}\sin\varphi_{13} = r_{12}\sin\varphi_{12} = r_{23}\sin\varphi_{23} = R. \tag{2.1}$$

The Laplace equation for pressure jumps across different interfaces gives,

$$\gamma_2 / r_{12} = \gamma_1 / r_{23} + \gamma_{12} / r_{13}. \tag{2.2}$$

And the projection of surface and interfacial tensions onto the chord line yields,

$$\gamma_2\cos\varphi_{12} + \gamma_1\cos\varphi_{23} = \gamma_{12}\cos\varphi_{13}. \tag{2.3}$$

Based on law of cosines, the Neumann's triangles shown in Figure 2.1 can be expressed as,

$$\begin{aligned} \theta_{112} &= \pi - \cos^{-1}\left(\frac{\Gamma_1^{\,2} - \Gamma_2^{\,2} + 1}{2\Gamma_1}\right) \\ \theta_{12} &= \pi - \cos^{-1}\left(\frac{\Gamma_1^{\,2} + \Gamma_2^{\,2} - 1}{2\Gamma_1\Gamma_2}\right) \end{aligned}. \tag{2.4}$$

Introducing dimensionless variables for interfacial tensions, $\Gamma_2 = \gamma_2 / \gamma_{12}$, $\Gamma_1 = \gamma_1 / \gamma_{12}$, and the dimensionless ratio of radii of curvature $R_{\text{ratio}} = r_{12} / r_{23}$, it follows that the three angles $\varphi_{12}, \varphi_{23}$ and φ_{13} can be simplified to be,

$$\begin{aligned} \sin\varphi_{12} &= \sqrt{\frac{4\Gamma_1^{\,2}\Gamma_2^{\,2} - \left(1 - \Gamma_1^{\,2} - \Gamma_2^{\,2}\right)^2}{4\Gamma_1\Gamma_2\left[\Gamma_1\Gamma_2\left(\mathrm{R}_{\text{ratio}}^2 + 1\right) - \mathrm{R}_{\text{ratio}}\left(\Gamma_1^{\,2} + \Gamma_2^{\,2} - 1\right)\right]}} \\ \sin\varphi_{13} &= (\Gamma_2 - \Gamma_1\mathrm{R}_{\text{ratio}})\sin\varphi_{12} \\ \sin\varphi_{23} &= \mathrm{R}_{\text{ratio}}\sin\varphi_{12} \end{aligned} \tag{2.5}$$

The volumes for Drop 1 and Drop 2 can be expressed as a sum of spherical caps,

$$\begin{aligned} V_1 &= \frac{1}{3}\pi\left(r_{23}^3\left(2+\cos\varphi_{23}\left(3-\cos^2\varphi_{23}\right)\right)-r_{13}^3\left(2-\cos\varphi_{13}\left(3-\cos^2\varphi_{13}\right)\right)\right) \\ V_2 &= \frac{1}{3}\pi\left(r_{12}^3\left(2-\cos\varphi_{12}\left(3-\cos^2\varphi_{12}\right)\right)+r_{13}^3\left(2-\cos\varphi_{13}\left(3-\cos^2\varphi_{13}\right)\right)\right) \end{aligned}, \quad (2.6)$$

Given the volumes of the two drops and the three interfacial tensions, different parameters of the compound drops can only be solved numerically because of the transcendental nature of Equation (2.6). The configuration of a compound drop in the absence of gravity is fully specified by Equations (2.1)-(2.6) as described in Torza and Mason's paper[19].

Since the Neumann triangle rule dictates that a compound drop can only exist if $\gamma_1 - \gamma_2 < \gamma_{12} < \gamma_1 + \gamma_2$, the normalized interfacial tension ratio $(\gamma_{12} - \gamma_1)/\gamma_2$ achieves values in the range of -1 to 1. Figure 2.2 shows the dependence of Neumann angles on different ratios of surface and interfacial tensions. The normalized interfacial tension ratio $(\gamma_{12} - \gamma_1)/\gamma_2$ being close to -1 represents almost the perfect wetting of the two drops while $(\gamma_{12} - \gamma_1)/\gamma_2$ being close to 1 represents the dewetting of the two drops. In Figure 2.2, each subplot is obtained for a fixed surface tension ratio γ_2/γ_1, while the horizontal axis represents the value of $(\gamma_{12} - \gamma_1)/\gamma_2$ and the vertical axis represents the value of Neumann angles as defined in Figure 2.1. In Figure 2.2a, when the surface tensions of Drop 1 and Drop 2 are equal, the angles θ_{112} and θ_{212} are the same because of the symmetry condition in Equation (2.4). The Neumann angle θ_{12} monotonically decreases from 180º to 0º with the increasing value of $(\gamma_{12} - \gamma_1)/\gamma_2$ because of the balance of the three interfacial tension vectors. Due to the broken symmetry $\gamma_1 \neq \gamma_2$, other subplots in Figure 2.2 have a different feature from Figure 2.2a, i.e. the angle θ_{212} can be of any value in the range of 0º to 180º, instead of the range of 90º to 180º. The angle θ_{212} is a monotonic increasing function with respect to $(\gamma_{12} - \gamma_1)/\gamma_2$. In contrast, the angle θ_{112} is not a

monotonic function of $(\gamma_{12}-\gamma_1)/\gamma_2$ and attains the limiting value of 180º for both the largest and smallest interfacial tension values, i.e. $(\gamma_{12}-\gamma_1)/\gamma_2 \sim \pm 1$. This geometry is supported by the fact that when $\gamma_2 < \gamma_1$, in either limit of $\gamma_{12}=\gamma_1-\gamma_2$ or $\gamma_{12}=\gamma_1+\gamma_2$, the interfacial tension γ_{12} is always anti-parallel to the surface tension γ_1. These relations of Neumann's angles are important in determining the stability of a compound sessile drop in the presence of gravity.

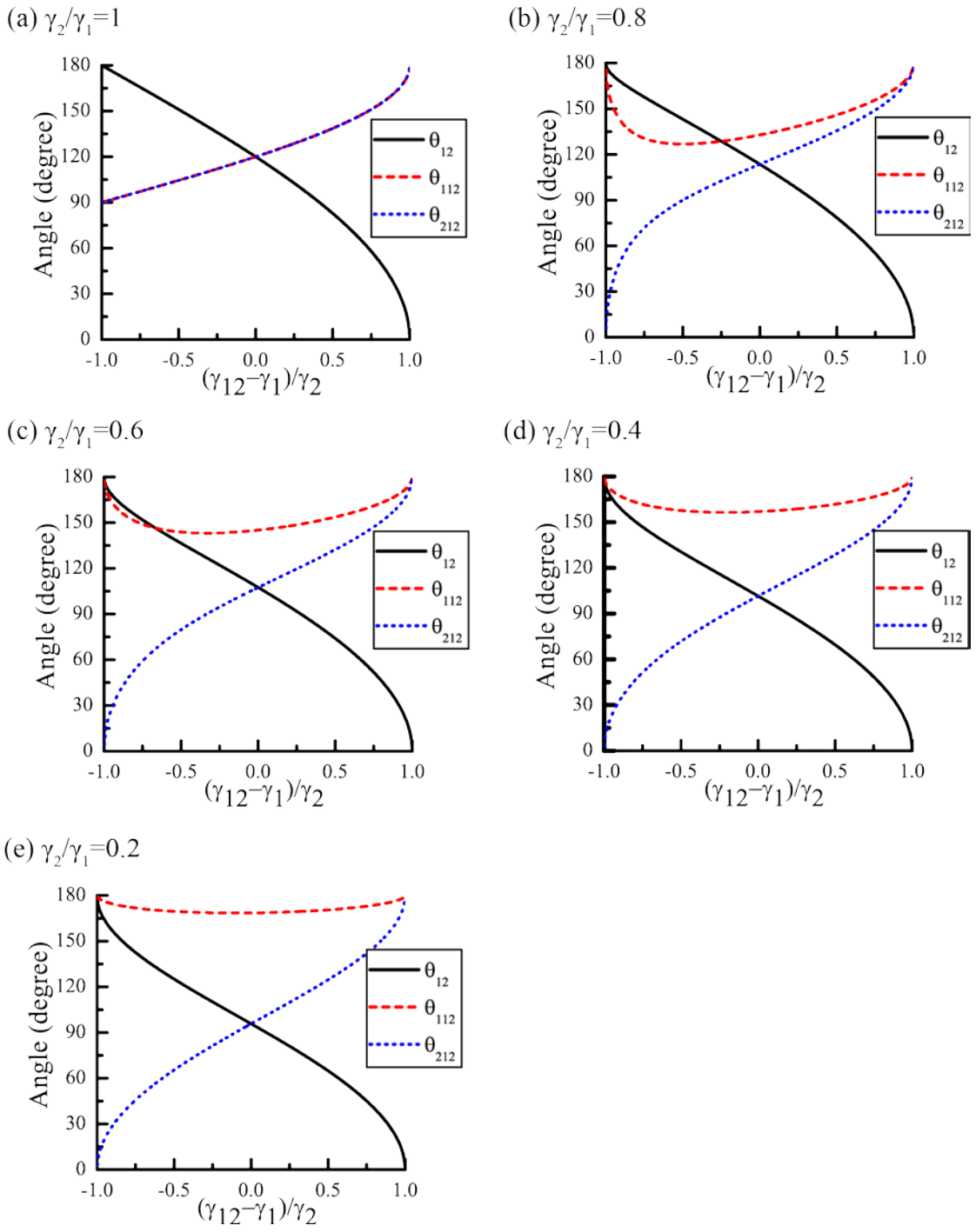

Figure 2.2. Dependence of Neumann angles on the ratio of surface and interfacial tensions. Each subplot (a)-(e) is obtained for fixed surface tension ratio γ_2/γ_1 with values 1, 0.8, 0.6, 0.4 and 0.2 respectively. The angles θ_{12}, θ_{112} and θ_{212} are represented with three different curves. Note, in subplot (a) the values of , θ_{112} and θ_{212} overlap with each other due to symmetry.

2.2.2 Governing equations for a single axisymmetric sessile drop

The shape of an axisymmetric sessile drop (Figure 2.3) deposited on a nondeformable solid substrate is dependent on both capillary and gravitational forces[1, 3, 40, 47]. The capillary forces include three interfacial tensions: solid-liquid interfacial tension γ_{SL}, solid-vapor interfacial tension γ_{SV} and liquid-vapor interfacial tension (or surface tension) γ. The gravitational forces on the sessile drop are dependent on the air density ρ_A, the fluid density of the drop ρ_L and the gravitational acceleration *g*. The drop configuration is subjected to a volume constraint *V*. Independent parameters can be determined for the static configuration, by writing down the governing equations for a single sessile drop.

The coordinate system is defined in Figure 2.3 with the direction of the vertical coordinate defined as positive in the direction of the gravitational acceleration. The height of drop is denoted by $h(r)$, where $h_r = \partial h / \partial r$ and $h_{rr} = \partial^2 h / \partial r^2$ are the first and second order partial derivatives. The hydrostatic equilibrium condition for an axisymmetric sessile drop is given by,

$$P_0 + \gamma\left(\frac{1}{r}\frac{h_r}{(1+h_r^2)^{1/2}} + \frac{h_{rr}}{(1+h_r^2)^{3/2}}\right) + \Delta\rho g h^0 = P_0 + \gamma\kappa^0 + \Delta\rho g h, \tag{2.7}$$

where P_0 is the atmospheric pressure, κ^0 is the curvature at the apex, $\Delta\rho = \rho_L - \rho_A$ is the density difference between the fluid drop ρ_L and the air ρ_A, and h^0 is the height at the axis of symmetry. Also the contact angle α at the three phase line has to obey Young's law: $\gamma_{SV} = \gamma_{SL} + \gamma\cos\alpha$. Equation (2.7) simplifies to the Laplace equation,

$$\left(\frac{1}{r}\frac{h_r}{(1+h_r^2)^{1/2}} + \frac{h_{rr}}{(1+h_r^2)^{3/2}}\right) - \kappa^0 = +\frac{\Delta\rho g}{\gamma}(h - h^0), \tag{2.8}$$

subject to the boundary conditions,

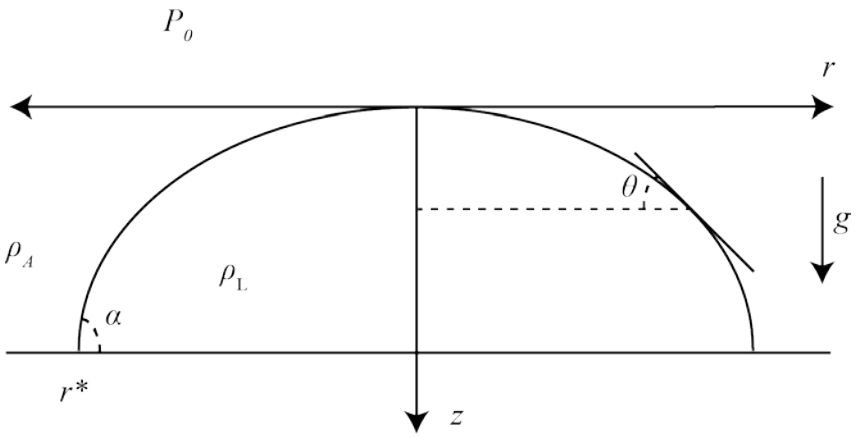

Figure 2.3 Shape of an axisymmetric sessile drop on a solid surface. The vertical downward direction is the gravitational acceleration. The radius of contact with the solid surface is r^*.

$$\begin{aligned} h &= h^0 \quad \text{at } r = 0 \\ h_r &= 0 \quad \text{at } r = 0 \\ h_r &= \tan\alpha \quad \text{at } r = r^* \end{aligned} \quad , \tag{2.9}$$

where r^* is the contact radius of the sessile drop.

Integration of Equation (2.8) gives the drop height $h = h(\kappa_0, C_1, C_2, \Delta\rho g/\gamma)$ as a function of the curvature κ^0 and the capillary length $(\gamma/\Delta\rho g)^{1/2}$ with two integration constants C_1 and C_2. The three boundary conditions (Equation (2.9)) specify the three unknown variables κ^0, C_1 and C_2 by solving Equation (2.8), with the input parameters of the contact angle α, the contact radius of the drop r^*, the apex height h^0 and the capillary length $(\gamma/\Delta\rho g)^{1/2}$. The volume of the drop is an output quantity by integrating the drop shape profile $V = \int_0^{r^*} 2\pi r h(r) dr,$ which is dependent on the input parameters. Table 2.1 lists the four input dimensional parameters to specify the shape of an axisymmetric sessile drop.

Equation (2.8) can be written in dimensionless form by expressing the radial and axial coordinates in terms of dimensionless variables,

Table 2.1 Input parameters for a sessile drop on a solid substrate

	Dimensional parameter	Dimensionless parameter
Input parameter to fully specify the drop shape	Contact angle α Contact radius $r*$ Reference height h^0 Capillary length $(\gamma/\Delta\rho g)^{1/2}$	Contact angle α Contact radius $r*/(\gamma/\Delta\rho g)^{1/2}$
Output	Volume V	Volume $V/(\gamma/\Delta\rho g)^{3/2}$

$$x \equiv r/a = r/(\gamma/\Delta\rho g)^{1/2},$$

$$z \equiv (h-h^0)/a + \kappa^0 a = (h-h^0)/(\gamma/\Delta\rho g)^{1/2} + \kappa^0(\gamma/\Delta\rho g)^{1/2},$$

where $a \equiv (\gamma/\Delta\rho g)^{1/2}$ is the capillary length. Substituting these dimensionless variables in Equation (2.8) gives,

$$\left(\frac{1}{x}\frac{z_x}{(1+z_x^{\,2})^{1/2}} + \frac{z_{xx}}{(1+z_x^{\,2})^{3/2}}\right) = z \tag{2.10}$$

The boundary conditions in dimensionless form now reduce to,

$$\begin{aligned} z &= \kappa^0 a \quad \text{at } x = 0 \\ z_x &= 0 \quad\;\; \text{at } x = 0 \\ z_x &= \tan\alpha \;\; \text{at } x = r*/(\gamma/\Delta\rho g)^{1/2} \end{aligned} \tag{2.11}$$

The second order differential equation yields 2 unknown integration constants. The boundary conditions (Equation (2.11)) has 3 dimensionless variables $\kappa^0 a$, α and $r*/(\gamma/\Delta\rho g)^{1/2}$. Therefore, 2 input parameters are required: α and $r*/(\gamma/\Delta\rho g)^{1/2}$ to fully specify the dimensionless drop shape. The dimensionless volume $V/(\gamma/\Delta\rho g)^{3/2} = \int_0^{r*/(\gamma/\Delta\rho g)^{1/2}} 2\pi x z(x)dx$ is

an output by integration. Table 2.1 also lists the required parameters to specify the shape of an axisymmetric sessile drop in dimensionless form. Alternatively, if the input parameters are the dimensionless volume $V/(\gamma/\Delta\rho g)^{3/2}$ and the contact angle α, then the output would be the dimensionless contact radius $r*/(\gamma/\Delta\rho g)^{1/2}$.

The shape of a single axisymmetric sessile drop can be solved through asymptotic expansion using perturbation approach at either small or large surface tension limit[39]. The general shape of a sessile drop with arbitrary surface tension can only be solved numerically[47].

2.2.3 Compound sessile drop results in the zero Bond number limit

For a single drop, the Bond number *Bo* measures the relative importance of the surface tension force to the gravitational force on the shape of a drop. The Bond number is defined as $Bo = L^2/(\gamma/\Delta\rho g)$, where $\Delta\rho$ is the density difference between the drop and the ambient liquid, $L = V^{1/3}$ is the characteristic length of the drop estimated from the drop volume *V*, and γ is the interfacial tension between drop and ambient phase. Compared to compound drops within another liquid phase, compound sessile drops in air can have much larger Bond numbers because of the increased density difference $\Delta\rho$. Therefore, even though the spherical cap approximation works well in solving the shapes of the compound drops, to apply this approximation for compound sessile drops in air, the drop sizes should be very small to maintain small Bond numbers.

Compound sessile drops have more potential geometrical configurations than compound drops because at least one drop is in contact with a solid surface. For example, Janus configurations (two partially engulfing drops both in contact with the solid surface) and axisymmetric configurations were observed and analyzed previously[26, 27, 44, 48]. The equilibrium

shapes for the Janus configurations were solved using phase field model by integrating the wetting properties, which demonstrated good agreements with the experimental results[48]. The equilibrium shapes for the axisymmetric configurations were examined analytically in the absence of gravity[26, 27] which were similar to the compound drop calculations by Torza and Mason[19].

Berthier and Brakke showed that rotationally symmetric configurations of drops or fluid surfaces tend to have lower energy than arbitrary shapes using the Steiner symmetrization process, even though the Steiner symmetrization itself does not produce the minimum energy configuration.[9, 49] However, the Steiner symmetrization does not indicate whether the rotationally symmetric state is an energy minimum or energy maximum, i.e. the question of the stability of an axisymmetric compound sessile drop is yet to be determined.

In the rest of the current chapter, we will first determine the parameters which govern the axisymmetric compound sessile drop shapes. These parameters provide a criterion for the stability of the axisymmetric configuration which is solved in the limit of zero Bond number where gravity force is still present (this is the zero size drop limit). Lastly, the zero Bond number limit calculation is compared with Surface Evolver simulations and experiments to verify the general conditions for the stability of the axisymmetric compound sessile drops.

2.3 Theory for Equilibrium Configuration and Stability Analysis

2.3.1 Governing equations and input parameters for compound sessile drops

Figure 2.4 shows the schematic diagram of a compound sessile drop. The lower drop which is in direct contact with solid surface is denoted as Drop 1, while the upper drop is denoted as Drop 2. The ambient phase can be any phase (vacuum, air or another fluid) which is immiscible

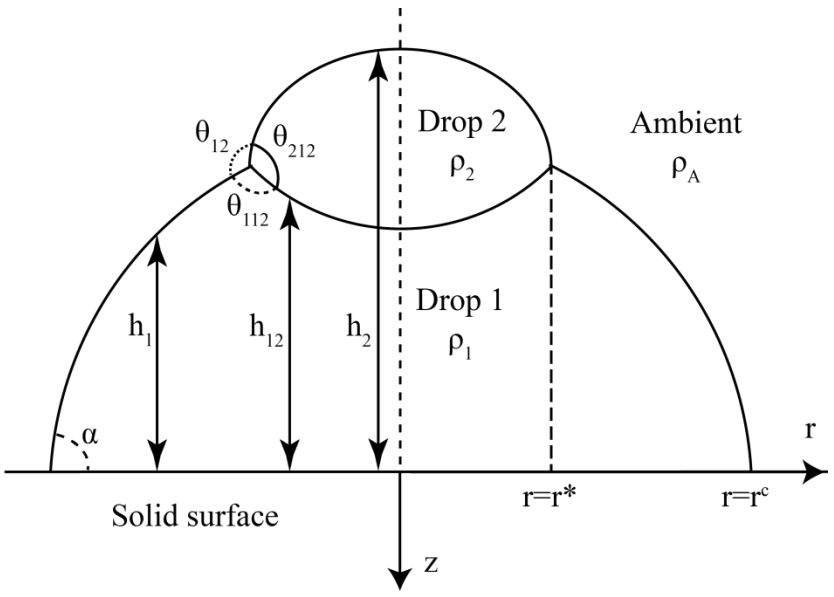

Figure 2.4 Schematic diagram of an axisymmetric compound sessile drop. The lower drop denoted as Drop 1 is in direct contact with the solid surface. The upper drop is denoted as Drop 2. The ambient fluid with density ρ_A can be either air or another fluid.

with both Drop 1 and Drop 2. The center of the basal plane of Drop 1 is the origin of the coordinate system and the downward vertical direction is defined to be positive. The densities of the three fluid phases are denoted as ρ_1, ρ_2 and ρ_A, respectively. The symbol h_1 denotes the distance from the basal plane to the phase boundary between the ambient phase and Drop 1; h_2 denotes the distance to the boundary between Drop 2 and the ambient phase; and h_{12} denotes the distance to the boundary between Drop 1 and Drop 2. The contact angle of Drop 1 with the solid surface is denoted by angle α, which can be any value ranging between the advancing contact angle and the receding contact angle for the system of Drop 1 and the solid surface. The first and second order derivatives of the Drop 1 interface with respect to the radius are expressed using simplified notation as $h_{1,r} = \partial h_1 / \partial r$ and $h_{1,rr} = \partial^2 h_1 / \partial r^2$, respectively. The derivatives of other variables are defined in the same fashion.

The derivation for the compound sessile drop configuration is similar to the calculation of the sessile lens between two infinite fluid phases outlined by Pujado and Scriven[41], with different boundary conditions. At equilibrium, the three phase boundaries for the compound sessile drop each satisfy the Laplace equation,

$$\begin{aligned}
&(\frac{1}{r}\frac{h_{1,r}}{(1+h_{1,r}{}^2)^{1/2}}+\frac{h_{1,rr}}{(1+h_{1,r}{}^2)^{3/2}})-\kappa_1^0=\frac{\Delta\rho_{1A}g}{\gamma_{1A}}(h_1-h_1^0)\\
&(\frac{1}{r}\frac{h_{2,r}}{(1+h_{2,r}{}^2)^{1/2}}+\frac{h_{2,rr}}{(1+h_{2,r}{}^2)^{3/2}})-\kappa_2^0=\frac{\Delta\rho_{2A}g}{\gamma_{2A}}(h_2-h_2^0) \quad ,\\
&(\frac{1}{r}\frac{h_{12,r}}{(1+h_{12,r}{}^2)^{1/2}}+\frac{h_{12,rr}}{(1+h_{12,r}{}^2)^{3/2}})-\kappa_{12}^0=\frac{\Delta\rho_{12}g}{\gamma_{12}}(h_{12}-h_{12}^0)
\end{aligned} \tag{2.12}$$

where h_1^0, h_2^0 and h_{12}^0 represent the heights of different interfaces (or extended interface for h_{12}) at the symmetry axis; κ_1^0, κ_2^0 and κ_{12}^0 represent the curvature of the interfaces (or extended interface for h_{12}) on the symmetry axis; $\Delta\rho_{1A}=\rho_1-\rho_A$, $\Delta\rho_{2A}=\rho_2-\rho_A$ and $\Delta\rho_{12}=\rho_1-\rho_2$ represent the density differences of the phases; and γ_{1A}, γ_{2A} and γ_{12} are the three interfacial tensions between different phases. In the remainder of Chapter 2, we refer to any interface shape that satisfies the Laplace equation, i.e., that is subject to a balance of gravity and surface tension forces, as a Laplacian shape.

The three fluid phase contact line has to satisfy the Neumann's triangle condition at $x = r^*$,

$$\begin{aligned}
\cos(\theta_{12})&=-\frac{\gamma_{1A}^2+\gamma_{2A}^2-\gamma_{12}^2}{2\gamma_{1A}\gamma_{2A}}\\
\cos(\theta_{112})&=-\frac{\gamma_{12}^2+\gamma_{1A}^2-\gamma_{2A}^2}{2\gamma_{12}\gamma_{1A}}
\end{aligned}, \tag{2.13}$$

where θ_{12} is the angle formed by the interfaces of h_1 and h_2, and θ_{112} is the angle formed

by the interfaces of h_1 and h_{12}. The other Neumann angle θ_{212} formed by the interface of h_2 and h_{12} can be expressed as $\theta_{212} = 2\pi - \theta_{12} - \theta_{112}$ as the sum of three angles is 360º.

In addition to the typical boundary conditions for geometric relations, there is a pressure jump condition for the equilibrium compound sessile drop,

$$\gamma_{1A}\kappa_1^0 - \rho_{1A}gh_1^0 + \gamma_{2A}\kappa_2^0 - \rho_{2A}gh_2^0 + \gamma_{12}\kappa_{12}^0 - \rho_{12}gh_{12}^0 = 0\,,$$

which can be interpreted as the pressure change across interface h_1 is equal to the pressure change across interface h_2 and h_{12} through a different path of calculation.

Similar to the calculation for a single sessile drop in Section 2.2.2, the Laplace equations (Equation (2.12)) can be written in dimensionless form by defining dimensionless variable in the cylindrical coordinate,

$$x \equiv r / a_{1A} = r / (\gamma_{1A} / \Delta\rho_{1A}g)^{1/2}\,,$$

where $a_{1A} \equiv (\gamma_{1A} / \Delta\rho_{1A}g)^{1/2}$ is the capillary length for the interface of h_1. The heights of three interfaces can be written in dimensionless form with the same reference height $-h_1^0 / a_{1A} + \kappa_1^0 a_{1A}$,

$z_1 \equiv h_1 / a_{1A} - h_1^0 / a_{1A} + \kappa_1^0 a_{1A}$, $z_2 \equiv h_2 / a_{1A} - h_1^0 / a_{1A} + \kappa_1^0 a_{1A}$ and $z_{12} \equiv h_{12} / a_{1A} - h_1^0 / a_{1A} + \kappa_1^0 a_{1A}$.

Substituting the dimensionless variables in Equation (2.12) yields,

$$\left(\frac{1}{x}\frac{z_{1,x}}{(1+z_{1,x}{}^2)^{1/2}} + \frac{z_{1,xx}}{(1+z_{1,x}{}^2)^{3/2}}\right) = z_1 \qquad (2.14.a)$$

$$\left(\frac{1}{x}\frac{z_{2,x}}{(1+z_{2,x}{}^2)^{1/2}} + \frac{z_{2,xx}}{(1+z_{2,x}{}^2)^{3/2}}\right) = \left(\frac{a_{1A}}{a_{2A}}\right)^2\left[z_2 + \frac{1}{a_{1A}}(a_{2A}^2\kappa_2^0 - h_2^0) + \frac{1}{a_{1A}}(a_{1A}^2\kappa_1^0 - h_1^0)\right]\,. \qquad (2.14.b)$$

$$\left(\frac{1}{x}\frac{z_{12,x}}{(1+z_{12,x}{}^2)^{1/2}} + \frac{z_{12,xx}}{(1+z_{12,x}{}^2)^{3/2}}\right) = \left(\frac{a_{1A}}{a_{12}}\right)^2\left[z_{12} + \frac{1}{a_{1A}}(a_{12}^2\kappa_{12}^0 - h_{12}^0) + \frac{1}{a_{1A}}(a_{1A}^2\kappa_1^0 - h_1^0)\right] \qquad (2.14.c)$$

The corresponding boundary conditions in dimensionless form are:

$$z_{2,x} = 0 \qquad \text{at } x = 0 \tag{2.15.a}$$

$$z_{12,x} = 0 \qquad \text{at } x = 0 \tag{2.15.b}$$

$$z_{1,x} = \tan\alpha \qquad \text{at } x = r^c / (\gamma_{1A} / \Delta\rho_{1A} g)^{1/2} \tag{2.15.c}$$

$$\tan^{-1}(z_{1,x}) = \tan^{-1}(z_{2,x}) + \theta_{21} - \pi \qquad \text{at } x = r^* / (\gamma_{1A} / \Delta\rho_{1A} g)^{1/2}. \tag{2.15.d}$$

$$\tan^{-1}(z_{2,x}) = \tan^{-1}(z_{12,x}) + \theta_{212} \qquad \text{at } x = r^* / (\gamma_{1A} / \Delta\rho_{1A} g)^{1/2} \tag{2.15.e}$$

$$z_1 = z_2 \qquad \text{at } x = r^* / (\gamma_{1A} / \Delta\rho_{1A} g)^{1/2} \tag{2.15.f}$$

$$z_2 = z_{12} \qquad \text{at } x = r^* / (\gamma_{1A} / \Delta\rho_{1A} g)^{1/2} \tag{2.15.g}$$

Equation (2.15.a) and (2.15.b) state that the slopes of the interfaces h_2 and h_{12} are zero at the symmetry axis. Equation (2.15.c) specifies the contact angle at the solid-liquid contact line. Equation (2.15.d) and (2.15.e) specify the slopes of interfaces h_1 and h_2 at the three phase contact line. Equation (2.15.f) and (2.15.g) specify that the height of interface h_1, h_2 and h_{12} are the same at the three phase contact line r^*. Also, the pressure jump condition in the dimensionless form gives,

$$\frac{1}{a_{1A}}(a_{1A}^2\kappa_1^0 - h_1^0) + \frac{\rho_{2A}}{\rho_{1A}}\frac{1}{a_{1A}}(a_{2A}^2\kappa_2^0 - h_2^0) + \frac{\rho_{12}}{\rho_{1A}}\frac{1}{a_{1A}}(a_{12}^2\kappa_{12}^0 - h_{12}^0) = 0. \tag{2.15.h}$$

Because of the method of nondimensionalization, the heights of interfaces at the axis of symmetry x=0 are,

$$z_1(0) = h_1^0 / a_{1A} + (\kappa_1^0 a_{1A}^2 - h_1^0) / a_{1A} \tag{2.15.i}$$

$$z_2(0) = h_2^0 / a_{1A} + (\kappa_1^0 a_{1A}^2 - h_1^0) / a_{1A} \tag{2.15.j}$$

$$z_{12}(0) = h_{12}^0 / a_{1A} + (\kappa_1^0 a_{1A}^2 - h_1^0) / a_{1A} \tag{2.15.k}$$

There are 6 unknown integration constants to be determined in Equation (2.14). The boundary conditions specified in Equation (2.15) have 13 unknown dimensionless quantities: $(a_{1A}^2\kappa_1^0 - h_1^0)/a_{1A}$, $(a_{2A}^2\kappa_2^0 - h_2^0)/a_{1A}$, $(a_{12}^2\kappa_{12}^0 - h_{12}^0)/a_{1A}$, a_{1A}/a_{2A}, a_{1A}/a_{12}, θ_{21}, θ_{212}, α, $r^c/(\gamma_{1A}/\Delta\rho_{1A}g)^{1/2}$, $r^*/(\gamma_{1A}/\Delta\rho_{1A}g)^{1/2}$, h_1^0/a_{1A}, h_2^0/a_{1A} and h_{12}^0/a_{1A}. There are 11 equations in boundary conditions Equation (2.15) and 19 dimensionless variables to be determined for the

Table 2.2 Input parameters to fully specify an axisymmetric compound sessile drop

	Dimensionless equations	
Input parameters	Neumann angles	θ_{212}, θ_{21}
	Contact angle	α
	Dimensionless radii	$r^c / (\gamma_{1A} / \Delta\rho_{1A} g)^{1/2}$, $r^* / (\gamma_{1A} / \Delta\rho_{1A} g)^{1/2}$
	Ratios of capillary length	a_{12} / a_{1A}, a_{2A} / a_{1A}
	Reference height	$h_1^0 / a_{1A} = 0$
Output	Dimensionless volume	$V_1 / (\gamma_{1A} / \Delta\rho_{1A} g)^{3/2}$, $V_2 / (\gamma_{2A} / \Delta\rho_{2A} g)^{3/2}$

axisymmetric compound sessile drop. Thus once we specify the 8 dimensionless variables: $\theta_{21}, \theta_{212}, \alpha, r^c / (\gamma_{1A} / \Delta\rho_{1A} g)^{1/2}, r^* / (\gamma_{1A} / \Delta\rho_{1A} g)^{1/2}, a_{12} / a_{1A}, a_{2A} / a_{1A}, h_1^0 / a_{1A}$, the shape of the axisymmetric compound sessile drop can be determined in dimensionless form. Once the shape is determined, the volumes of the two drops can be calculated by integrating the interfaces.

All the dimensionless parameters are summarized in Table 2.2. The set of input parameters can be changed in different ways. For example, the two dimensionless radii can be the output parameters if both the dimensionless volumes are selected as input parameters; two of the Neumann angles can be replaced by the specified ratios of interfacial tensions $\gamma_{1A} / \gamma_{2A}$ and $\gamma_{1A} / \gamma_{12}$. Note that the Laplace equations (Equation (2.14)) and boundary conditions (Equation (2.15)) only depends on the density differences and pressure jumps due to curvature. This

suggests that the ambient density ρ_A and the ambient pressure P_0, can be treated as reference quantities, and the system can be taken to have zero ambient pressure, zero ambient density, and the reduced densities $\rho_1 - \rho_A$ and $\rho_2 - \rho_A$ for Drop 1 and Drop 2 respectively.

The differential equations (Equation (2.14)) subject to the boundary conditions (Equation (2.15)) do not have a closed-form solution. Furthermore, since the shape of the compound sessile drop is governed by 7 parameters (8 parameters including reference height), it is difficult to obtain physical intuition from the numerical solutions. Thus, we consider the zero Bond number limit to reduce the number of governing parameters and gain insight into the stability of the axisymmetric configuration. In the zero Bond number limit, drop shapes do not depend on capillary lengths (the Laplace equation yields spherical cap solutions), thus the parameters governing the drop shape reduce to four dimensionless parameters γ_{12}/γ_{1A}, γ_{2A}/γ_{1A}, V_2/V_1 and α. In contrast, compound drop shapes in the zero Bond number limit only depend on $\gamma_{12}/\gamma_1, \gamma_2/\gamma_1$ and V_2/V_1.[19]

2.3.2 Stability of compound sessile drops of Laplacian shapes

The equilibrium profile of the compound sessile drop in the absence of gravity was solved by Mahadevan *et al*[26] and by Neeson *et al*[27] independently, with similar approximations applied in the earlier work of Torza and Mason[19]. However, in determining the stability criteria for the compound sessile drop, neither the forces arising from gravity (the weight of the drop itself) nor buoyancy (displacement of the bottom fluid by the top drop) can be omitted; otherwise, the compound sessile drop is stable at any orientation. The assumption of spherical cap drop shapes is incompatible with the presence of a gravity field.[50] Hydrostatic pressure as a function of height within a drop results in a curvature difference at different heights; therefore, neither the gravity

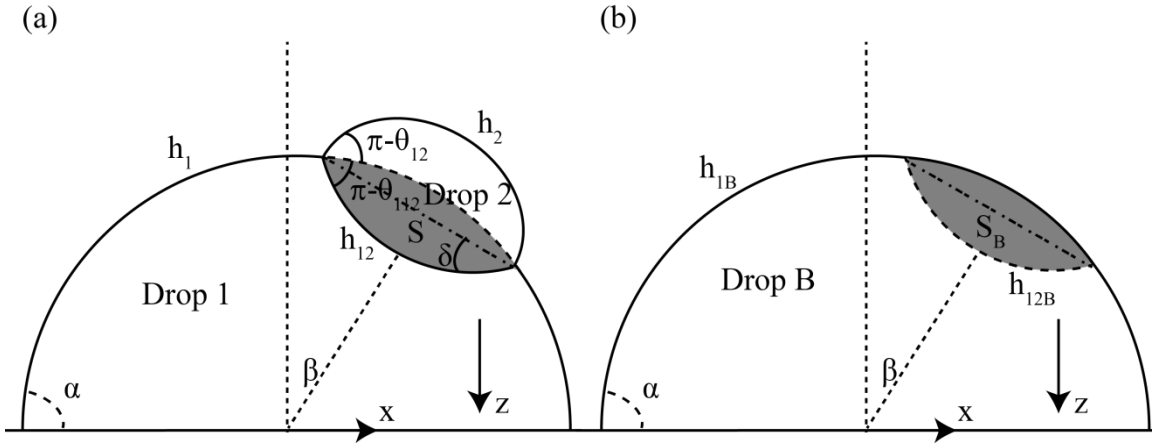

Figure 2.5 Stability of a compound sessile drop. (a) Top drop (Drop 2) offset from the axisymmetric position and bottom drop is still of Laplacian shape. The net force exerted on the top drop can be calculated to determine the stability of the axisymmetric equilibrium. Shaded region S has volume V_S. (b) One sessile drop on top of a solid surface with the same shape of Drop 1. The dashed line h_{12B} is be drawn to be identical to the interface h_{12}, and the shaded region S_B also has volume V_S.

force nor the buoyancy force are defined in spherical cap drops.

In the cases of one sessile[51, 52] or pendant drop[53, 54] in contact with a solid surface, difficulty arises in stability analysis because the perturbed shape can be any generic function, not necessarily restricted to the family of Laplacian shapes; i.e., perturbation analysis for liquid drops lies in the mathematical formulation of functional analysis, beyond the traditionally better understood realm of energy minimization based on convex analysis[55]. Because of this difficulty, we limit the stability analysis presented here to the subset of Laplacian drop shapes. In contrast to the typical stability analysis for mechanical equilibrium based on the second derivative of the potential energy at the extremum (or the first derivative of a conservative force)[56, 57], we directly calculate the force on the top drop when it is perturbed away from the axisymmetric position while interfaces are constrained to be of Laplacian shape.

Figure 2.5a shows a perturbed compound sessile drop where the top drop (Drop 2 of

Laplacian shape) is perturbed by an angle β away from the axisymmetric position. The bottom drop (Drop 1) is assumed to be of a continuous Laplacian shape, such that the extension of Drop 1 surface (dashed line) follows the same Laplace equation as the Drop 1 surface (solid line). The extension of Drop 1 surface and the interface between Drop 1 and Drop 2 (h_{12}) encloses a shaded region *S*, with volume V_S as shown in Figure 2.5a. The forces exerted on Drop 2 (enclosed by h_{12} and h_2) include the gravitational force and the forces exerted by Drop 1 through contact, i.e., the pressure force and the surface tension force. The total force exerted through contact will be calculated by constructing an identical Laplacian shape of a single sessile drop.

Figure 2.5b shows a single sessile drop denoted as Drop B, which has the identical shape to Drop 1 including the continuation of the surface of Drop 1; thus, the volume of Drop B is equal to the sum of volumes of Drop 1 and the shaded volume, $V_B = V_1 + V_S$. In Drop B, the dashed line h_{12B} shown in Figure 2.5b is identical to the interface h_{12} (in Figure 2.5a) to create the identical shaded volume region *S* in this single sessile drop case. Since both Drop 1 and Drop B have the same Laplacian shape, pressure fields along the interfaces h_{12} and h_{12B} are identical, and the surface tension forces along the three phase contact line (the intersection line of h_1 and h_{12} and the intersection line of h_{1B} and h_{12B}) are also identical in the two different configurations. Therefore the force exerted on Drop 2 through contact in the compound drop case is identical to the force exerted on the shaded region S_B (Figure 2.5b) through contact in the single drop case: $\vec{F}_{2,contact} = \vec{F}_{S_B,contact}$.

The force exerted on the shaded region through contact in the single drop case can be derived based on the properties of Laplacian shapes. Within a drop of Laplacian shape, fluid is in hydrostatic equilibrium[40, 50], i.e., any material body drawn experiences zero net force. The net

force on the material body of the shaded region in Figure 2.5b is the sum of the gravitational force and the force through contact: $\vec{F}_{S_B,net} = \vec{G}_{S_B} + \vec{F}_{S_B,contact} = 0$. Thus, the force through contact is of the same magnitude as the weight of shaded region S_B, but with opposite sign $\vec{F}_{S_B,contact} = -\vec{G}_{S_B} = -\rho_1 g V_S \hat{z}$.

The net force exerted on Drop 2 can be obtained by summing the gravity force and force through contact,

$$\begin{aligned} \vec{F}_{2,net} &= \vec{G}_2 + \vec{F}_{2,contact} = \vec{G}_2 + \vec{F}_{S_B,contact} \\ &= (\rho_2 g V_2 - \rho_1 g V_S)\hat{z} \end{aligned}, \tag{2.16}$$

where V_2 is the volume of Drop 2. This equation shows that the net force exerted on Drop 2 contains only a vertical component. There is no closed form expression for an arbitrary Laplacian shape enclosing the volumes of Drop 2 and the shaded region S (V_2 and V_S).

An interesting result from Equation (2.16) is that a more dense drop resting on top of a less dense is never stable. This can be stated even though there is no closed form expression for the volumes. A net upward force on Drop 2 restores it to the axisymmetric position, producing a stable axisymmetric equilibrium configuration; but Equation (2.16) predicts that for a more dense drop resting on top, the net force on Drop 2 once perturbed is always downward for the following reason. In Figure 2.5a, because of Neumann's triangle rule, the angle θ_{12} is always smaller than π; therefore the volume of Drop 2 is always larger than the volume of the shaded region S, i.e. $V_2 > V_S$. The net force on a more dense Drop 2 $\vec{F}_{2,net} = (\rho_2 g V_2 - \rho_1 g V_S)\hat{z}$ is always in the positive z direction (downward) due to the conditions $\rho_2 > \rho_1$ and $V_2 > V_S$.

This result that a more dense drop cannot rest stably on top of a less dense drop seems to be in contrast with the experimental findings of Phan *et al.*[33, 34], where more dense drops can float

on top of less dense flat fluid interface. In the case of a flat interface, the configuration of a more dense drop floating on top of a flat lower fluid has translational symmetry in the sense that the denser drop can be stable at any position if it is translated horizontally to any position without changing the total gravitational energy. In contrast, for compound sessile drops, the translational symmetry is broken and instead replaced with axisymmetry in the equilibrium configuration. Thus, the apex is intrinsically a unique position at the maximum height, even if a very large bottom drop can appear to have a nearly flat surface near the apex. Therefore, in the case of a compound sessile drop, a more dense drop cannot float stably on top of a less dense drop even though more dense drops are observed to float on top of a less dense flat fluid interface.

2.3.3 Stability criterion of Laplacian shape drops in the zero Bond number limit

To obtain an analytical expression, calculations are performed in the zero Bond number limit for both Drop 1 and Drop 2. In the zero Bond number limit, where the drop is much smaller than the capillary length, but gravity is still present, the shape is well approximated by a spherical cap to first order accuracy in the Bond number.[39]

In Figure 2.5a, δ is the angle between the base of the spherical cap and the interface between Drop 1 and Drop 2. In the zero Bond limit, the volume of Drop 2 is the sum of two spherical caps with basal angles δ and $2\pi - \theta_{112} - \theta_{12} - \delta$, where the angles θ_{12} and θ_{112} are the Neumann angles first introduced in Figure 2.1. Therefore the volume of Drop 2 is the sum of the two spherical caps,

$$V_2 = q(\delta)R^3 + q(2\pi - \theta_{112} - \theta_{12} - \delta)R^3,$$

where $q(\theta) = (2 - 3\cos(\theta) + \cos^3(\theta))\csc(\theta)^3\pi/3$ is a function representing the volume of a spherical cap with basal angle θ and unit basal radius; R is the basal radius of the spherical cap.

In the zero Bond number limit, the angle δ is determined based on geometric relationships to be a function of the volume ratio and the ratios of interfacial tensions as in Section 2.1.1. The volume V_S of the shaded region S is calculated similarly as the combination of two spherical caps with basal angles δ and $\pi - \theta_{12} - \delta$:

$$V_s = q(\pi - \theta_{12} - \delta)R^3 + q(\delta)R^3 .$$

Thus the net force exerted on the top drop (Equation (2.16)) is given by:

$$\vec{F}_{2,net} = R^3\{\rho_2 g[q(\delta) + q(2\pi - \theta_{112} - \theta_{12} - \delta)] - \rho_1 g[q(\pi - \theta_{12} - \delta) + q(\delta)]\}\hat{z} . \qquad (2.17)$$

Setting the net force equal to zero gives a critical condition for the density ratio:

$$\frac{\rho_2}{\rho_1}|_{critical} = \frac{q(\pi - \theta_{12} - \delta) + q(\delta)}{q(\delta) + q(2\pi - \theta_{112} - \theta_{12} - \delta)} . \qquad (2.18)$$

Since angles θ_{12} and angle θ_{112} are the Neumann's angles determined by ratios of interfacial tensions and angle δ depends on the volume ratio and contact angle through geometric relationships[19], the critical density ratio is then dependent on the volume ratio, the two interfacial tension ratios, and the contact angle at the solid surface.

A net upward force on Drop 2 restores it to the axisymmetric position, producing an energy minimum or a stable axisymmetric equilibrium configuration. When the density ratio is less than the critical value given in Equation (2.18), the axisymmetric configuration is stable. A net downward force on Drop 2 causes it to slide further away from the axisymmetric position, producing an energy maximum or an unstable axisymmetric configuration. Thus when the density ratio is greater than the critical density ratio, the axisymmetric configuration is unstable. In the following sections, we will use simulations and experiments to verify the stability conditions.

The derivation of the net force on Drop 2 does not depend on the value of β, the angle by

which Drop 2 is perturbed from the axisymmetric position. Therefore for compound sessile drops of Laplacian shapes in the zero Bond number limit, if the density ratio is not equal to the critical value, then there will be no equilibrium configuration other than the axisymmetric configuration without any topological changes such that only one drop is in contact with the solid surface. In this case the axisymmetric configuration is a unique extremum which is either a global minimum or a global maximum. At the energy maximum, any finite perturbations will cause Drop 2 to fall away from the apex. At the energy minimum, any finite perturbations that do not cause Drop 2 to touch the solid surface will restore it to the axisymmetric configuration.

The stability criterion (Eq. (2.18)) in the zero Bond number limit depends on the volume ratio of the two drops V_2/V_1, two interfacial tension ratios γ_{2A}/γ_{1A} and γ_{12}/γ_{1A}, and the contact angle α implicitly as described earlier. Figure 2.6 shows the dependence of the critical density ratio on the interfacial tension ratios with fixed volume ratio $V_2/V_1 = 0.2$, and fixed contact angle $\alpha = 90°$ as an example. The numerical code for obtaining the critical density ratio can be found in the Appendix 2.1 of this chapter. Each curve represents the critical density ratio as a function of the ratio $(\gamma_{12}-\gamma_{1A})/\gamma_{2A}$ for fixed ratio γ_{2A}/γ_{1A}. Since the three phase contact line between Drop 1, Drop 2 and the ambient phase must obey the Neumann condition, the allowed range of γ_{12}/γ_{1A} values is different for each γ_{2A}/γ_{1A} value, but the allowed values of $(\gamma_{12}-\gamma_{1A})/\gamma_{2A}$ lie between (-1, 1) for any given surface tension ratio γ_{2A}/γ_{1A}. For a fixed surface tension ratio γ_{2A}/γ_{1A}, the critical density ratio is a monotonically decreasing function of the ratio of interfacial tensions $(\gamma_{12}-\gamma_{1A})/\gamma_{2A}$. For fixed surface tensions, this parameter effectively represents the interfacial tension between Drop 1 and Drop 2. The critical density ratio is close to unity for a surface tension ratio of unity and the interfacial tension ratio near

$(\gamma_{12}-\gamma_{1A})/\gamma_{2A} \approx -1$. For a fixed value of $(\gamma_{12}-\gamma_{1A})/\gamma_{2A}$, the critical density ratio decreases with increasing surface tension ratio γ_{2A}/γ_{1A}. The inset of Figure 2.6 shows the rescaled critical density ratio based on the linear function, $\text{rescaled ratio} = (\text{ratio} - \text{ratio}_{\min})/(\text{ratio}_{\max} - \text{ratio}_{\min})$, where $\text{ratio}_{\min}$ and $\text{ratio}_{\max}$ represent the minimum and maximum critical density ratios within the allowed range of $(\gamma_{12}-\gamma_{1A})/\gamma_{2A}$ values. The rescaled critical density ratio lies between 0 and 1. The systematic deviation of the rescaled ratio (not collapsing to a single curve) suggests that the critical density ratio is not a simple function of the two ratios, $(\gamma_{12}-\gamma_{1A})/\gamma_{2A}$ and γ_{2A}/γ_{1A}, but rather that both are important in determining the critical conditions for the stability of a compound sessile drop.

In Figure 2.6, (a), (b), (c) and (d) denote the configurations of compound sessile drops with spherical cap shapes and Neumann's angle conditions resulting from the specified interfacial

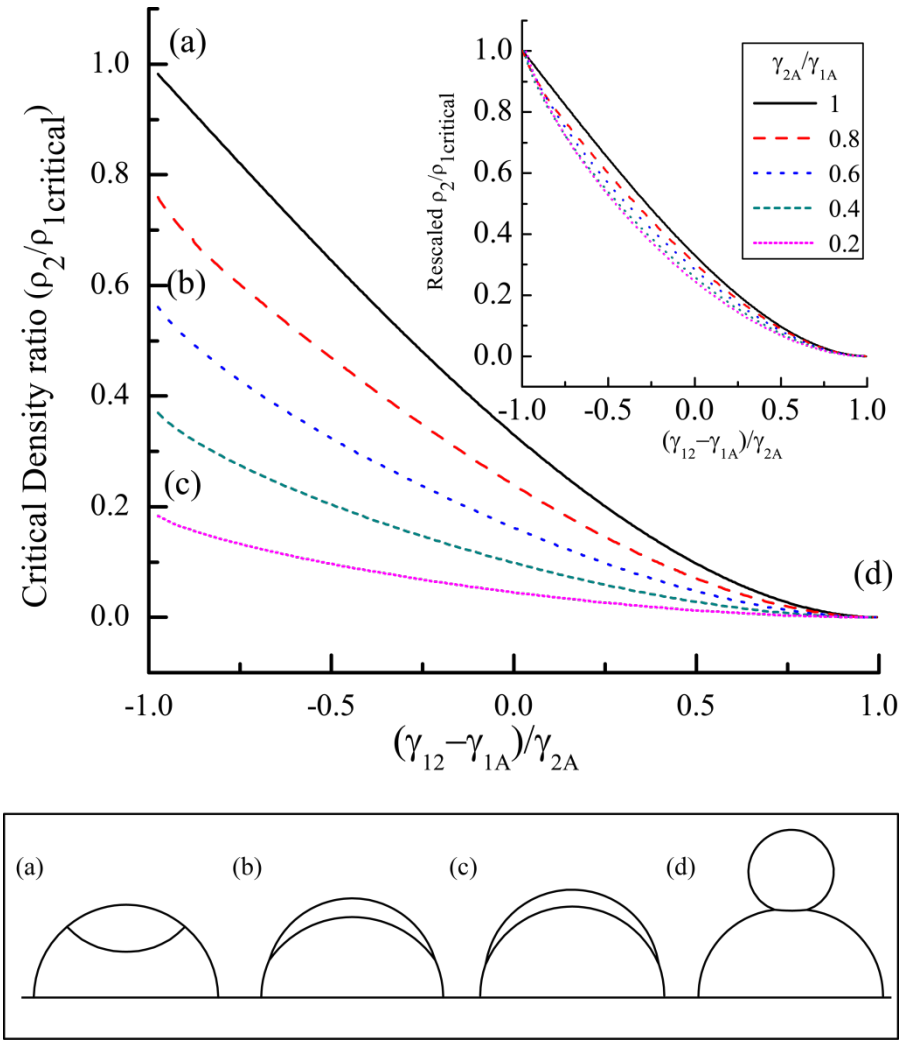

Figure 2.6 Critical density ratio as a function of surface and interfacial tensions with fixed volume ratio $V_2/V_1 = 0.2$, and fixed contact angle $\alpha = 90°$. Legend denotes the ratio of the top surface tension divided by the bottom surface tension. (a),(b), and (c) indicate the configurations of spherical cap shapes with Neumann's angles calculated for the corresponding interfacial tensions. ((a)γ_{2A}/γ_{1A}=1, (b) γ_{2A}/γ_{1A}=0.6, (c) γ_{2A}/γ_{1A}=0.2. For (a), (b) and (c), the value $(\gamma_{12}-\gamma_{1A})/\gamma_{2A}$ =-0.98 is kept constant. The configuration for (d) is obtained for dewetting drops with γ_{2A}/γ_{1A}=1 and $(\gamma_{12}-\gamma_{1A})/\gamma_{2A}$ =0.98.

tension ratios. In Section 2.1, we have described the Neumann's angle dependence on the surface and interfacial tensions. The surface tension ratios for configurations (a), (b) and (c) are γ_{2A}/γ_{1A} =1, 0.6, and 0.2 respectively while the interfacial tension ratio is fixed at

$(\gamma_{12}-\gamma_{1A})/\gamma_{2A}=-0.98$, indicating nearly the smallest interfacial tension achievable while still obeying the Neumann's triangle condition. Configuration (d) represents dewetting drops with very large interfacial tension $(\gamma_{12}-\gamma_{1A})/\gamma_{2A}=0.98$, and surface tension ratio $\gamma_{2A}/\gamma_{1A}=1$. However even for other values of γ_{2A}/γ_{1A}, the shapes obtained remain quite similar to that shown in (d) because the angle between the two surfaces is close to zero, while the angles between the surfaces and the interface are both close to 180º. These configurations agree with the physical intuition that dewetting drops are nominally less stable. This intuition is supported by the calculation that the critical density ratio is close to zero in this limit. For drops with small interfacial tensions, near $(\gamma_{12}-\gamma_{1})/\gamma_{2}=-0.98$, the drop shapes favor more contact of the two phases, therefore promoting greater stability.

Figure 2.6 suggests that the critical density ratio is larger for low interfacial tension systems and smaller for high interfacial tension systems. From the point of view of real systems, combinations of organic liquids (oil) and inorganic liquids (water) typically exhibit large interfacial tensions, while separated phases obtained by mixing partially miscible fluids exhibit relatively small interfacial tension values[58]. In the following sections we will consider both small and large interfacial tension systems separately in both simulation and experiments. While the derivation of the stability criterion is based on drops of Laplacian shape in the zero Bond number limit, we will see in the simulation and experimental results that the stability criterion for the limiting case provides a reasonable estimate even when the drop shapes are not constrained to Laplacian shapes, and even when the Bond number increases.

2.4 Simulations using Surface Evolver

The zero Bond number analysis shows that the critical density ratio separating the energy

maxima from the energy minima depends on the interfacial tension: larger interfacial tension yields a smaller critical density ratio. To verify the stability criterion, we conduct numerical simulations for both high and low interfacial tension systems. Because real experimental systems typically have fluid and interfacial properties that cannot be varied independently, simulations allow the independent roles of these properties to be isolated. Further, simulations can be used to examine finite Bond number situations.

The Laplace equation can be derived using a variational method based on the minimization of Gibbs free energy[50, 59–61]. Thus the configuration of a compound sessile drop satisfying the three Laplace differential equations can be solved numerically in this framework by minimizing the free energy. We utilize the open access software package Surface Evolver developed by Brakke[62, 63], which models the liquid surface shapes subject to various forces or constraints. We developed the code within the software adapted to the compound sessile drop geometry. The detailed code can be found in the appendix of this chapter. Appendix 2.2 lists the initial setup of the compound sessile drop geometry and procedures to represent the perturbations applied to the compound sessile drop.

As shown in Figure 2.7, we present some cases to verify that the shapes of the axisymmetric configurations at equilibrium are the same if the seven governing dimensionless parameters are kept fixed while varying the dimensional values of the physical properties. Figure 2.7a and Figure 2.7b shows two cases of compound sessile drops with the same volume but different values of densities, surface tensions and interfacial tensions, while the dimensionless variables as listed in Table 2.2 are kept the same. These two cases yield the same dimensionless configuration. Figure 2.7c and Figure 2.7d shows two cases of compound sessile drops with the same density but different values of volumes, surface tensions and interfacial tensions, while the

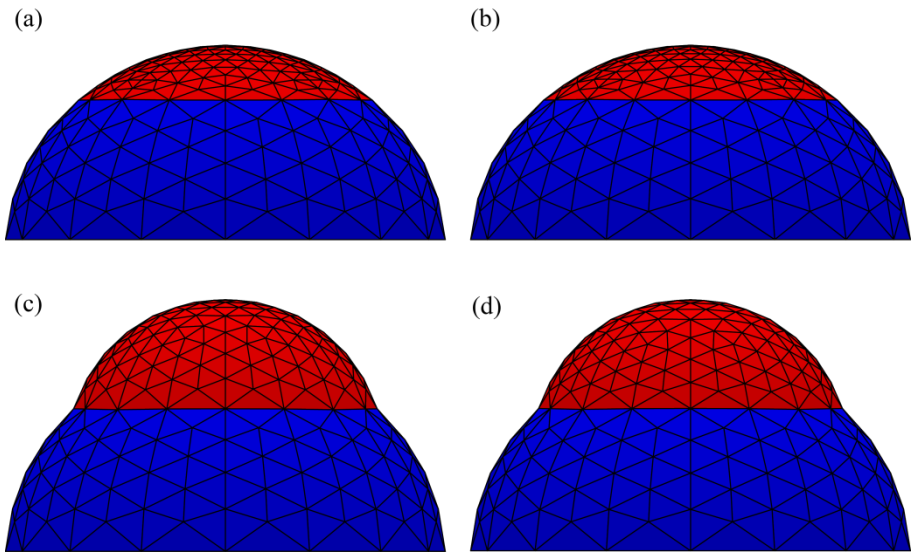

Figure 2.7 Equilibrium configurations for axisymmetric compound sessile drops. Same configurations are observed if the seven dimensionless paramters are kept fixed. All the bottom drops have 90º contact angle with the solid surface. (a) A compound sessile drop with the physical paprameters γ_{1A} = 41 mN/m, γ_{2A} = 40 mN/m, γ_{12} = 3 mN/m, ρ_1 = 1.4 g/ml, ρ_2 = 1.3 g/ml, V_1 = 5 μL and V_2 = 1 μL. (b) A compound sessile drop with physical paprameters γ_{1A} = 82 mN/m, γ_{2A} = 80 mN/m, γ_{12} = 6 mN/m, ρ_1 = 2.8 g/ml, ρ_2 = 2.6 g/ml, V_1 = 5 μL and V_2 = 1 μL. (c) A compound sessile drop with physical paprameters γ_{1A} = 70 mN/m, γ_{2A} = 30 mN/m, γ_{12} = 48 mN/m, ρ_1 = 1.4 g/ml, ρ_2 = 1.07 g/ml, V_1 = 5 μL, V_2 = 1 μL. (d) A compound sessile drop with physical paprameters γ_{1A} = 140 mN/m, γ_{2A} = 60 mN/m, γ_{12} = 96 mN/m, ρ_1 = 1.4 g/ml, ρ_2 = 1.07 g/ml, V_1 = 14.4 μL, V_2 = 2.88 μL.

dimensionless variables as listed in Table 2.2 are the same. These two cases also yield the same dimensionless configuration. In contrast, for cases with different input dimensionless parameters (Figure 2.7a vs. Figure 2.7c), the dimensionless configurations are different.

2.4.1 Simulation methods using Surface Evolver

Unlike the zero Bond number stability analysis in which we assumed the drops have Laplacian shape, in Surface Evolver we examine drop shapes that are perturbed with spherical cap shapes. This slightly different type of perturbation can provide a complementary perspective as to the influence of different perturbations on the stability.

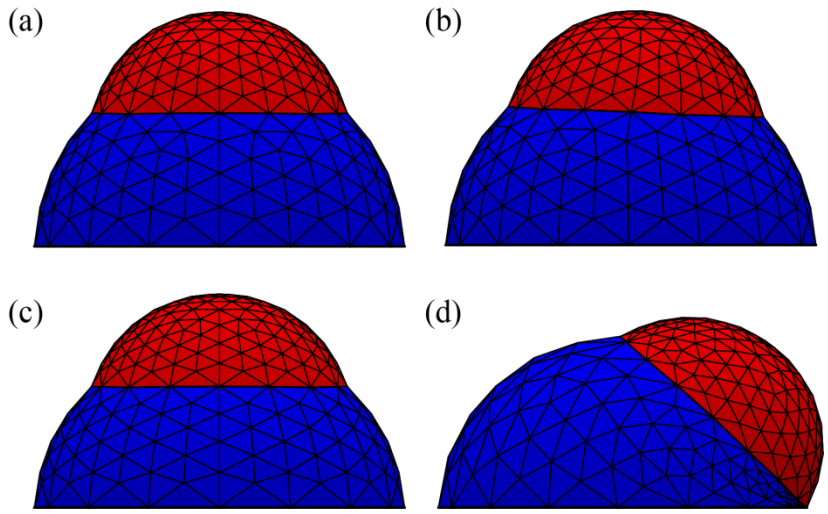

Figure 2.8. Protocol for determining whether the axisymmetric state is an energy maximum or minimum using Surface Evolver. (a) Initial axisymmetric equilibrium shape without gravity. (b) Top drop displaced from the vertical axis by about 3 degrees without gravity. (c) Upon application of gravity at small density ratios, the top drop returns to the apex position, indicating a minimum energy system. (d) Upon application of gravity at large density ratios, the top drop

The procedure for examining the stability of the axisymmetric configuration of the compound sessile drop is outlined in Figure 2.8. The equilibrium axisymmetric configuration is first obtained in a zero gravity environment, and then the top drop is displaced away from the axisymmetric position. Lastly, gravity is applied, and the evolution of the top drop is monitored. If the top drop slides off it is recorded as an unstable configuration, and if it restores to the apex it is considered stable. This perturbation bears some similarity to experiments in which the top drop is perturbed using a pipette tip, where gravity is always present. However, in simulation, the starting configuration of the perturbed drop shapes are constrained to spherical caps, while in experiments the perturbed drop shape is affected by the wetting properties of the pipette. The convergence of simulations is supported by the nearly constant energy output and scale after multiple runs as well as mesh refinement. As Surface Evolver uses a gradient descent method[62] to search for the energy minimum, it may occur that the final configuration is a local minimum

instead of the global minimum. However, the identification of a local minimum is sufficient to specify the stability at the axisymmetric configuration. Based on the gradient search direction, evolution away from the apex position indicates that the axisymmetric configuration is unstable while evolution toward the apex indicates that the axisymmetric configuration is stable.

In Figure 2.8, the surface tension of the smaller drop is $\gamma_{2A} = 25\,\text{mN/m}$, the surface tension of the larger drop is $\gamma_{1A} = 72\,\text{mN/m}$, and the interfacial tension is $\gamma_{12} = 52\,\text{mN/m}$. These surface and interfacial tension values correspond to a dodecane drop resting on a water drop in air; however, in simulations the fluid densities are varied. The dimensionless surface tension ratios for this case are $\gamma_{2A}/\gamma_{1A} = 0.35$ and $(\gamma_{12} - \gamma_{1A})/\gamma_{2A} = -0.8$. The contact angle for the larger drop against the solid substrate is fixed at $\alpha = 90°$. The volumes of the two drops are 1 μL and 5 μL, respectively. Figure 2.8a shows the equilibrium shape of the axisymmetric compound sessile drop obtained in zero gravity. In the absence of gravity, the shapes obtained from Surface Evolver are similar to the compound drop cases with no solid substrate examined by Guzowski *et al*[64], which are found to be independent of the fluid densities.

To examine the stability of the equilibrium axisymmetric position, the top drop is displaced about 3º from the vertical axis and allowed to equilibrate without gravity as shown in Figure 2.8b. Gravity is then applied to this perturbed state to examine the stability. By varying the densities of the two drops, we expect that the application of gravity will cause the interface to evolve in one of two ways: either it will restore to the axisymmetric configuration (Figure 2.8c), or it will slide off to the side, away from the apex (Figure 2.8d). Note that the configuration shown in Figure 2.8d does not represent the equilibrium state. In the current setup, Surface Evolver does not allow for a change of topology to accommodate the contact of the smaller drop with the solid surface. In real systems, when the deposited top drop contacts the solid surface, a “Janus”

configuration is formed, e.g., for the combination of perfluooctane and mercury[27]. The equilibrium configuration of a Janus type compound sessile drop has been modeled using a phase field modeling approach, which is capable of depicting the different wetting properties of the fluids on the solid surface.[48] As we are presently interested in the stability of the axisymmetric configuration, the movement of the second drop away from the axisymmetric position is sufficient to demonstrate the lack of stability of the configuration.

As shown in Figure 2.8c and d, depending on the densities at fixed surface tensions, interfacial tension, contact angle and volumes, the axisymmetric equilibrium can be categorized as either an energy minimum or an energy maximum. Note that the drop shapes shown in Figure 2.8c are flattened compared with those of Figure 2.8a owing to the presence of gravity. Note that when the density ratio used in simulation is close to the critical density ratio, the convergence rate for evolution of the interface is very slow. Thus to further narrow in on the dividing line, for density ratios close to the critical value, unstable cases have been repeated with a smaller perturbation of 1º from the apex. Only those configurations that remain unstable at a 1º displacement are marked as energy maxima.

2.4.2 Simulation results using Surface Evolver

Figure 2.9a summarizes the simulation results for the high interfacial tension system. The densities of the two drops are varied to achieve different ratios as well as different Bond numbers. In Figure 2.9a, the stability of each configuration is noted as a function of the density ratio and the Bond number of Drop 1, for a fixed volume ratio of 0.2. Stable configurations are marked by open symbols, while unstable configurations are marked by filled symbols. The simulations result in stable configurations at lower density ratios and unstable configurations at higher

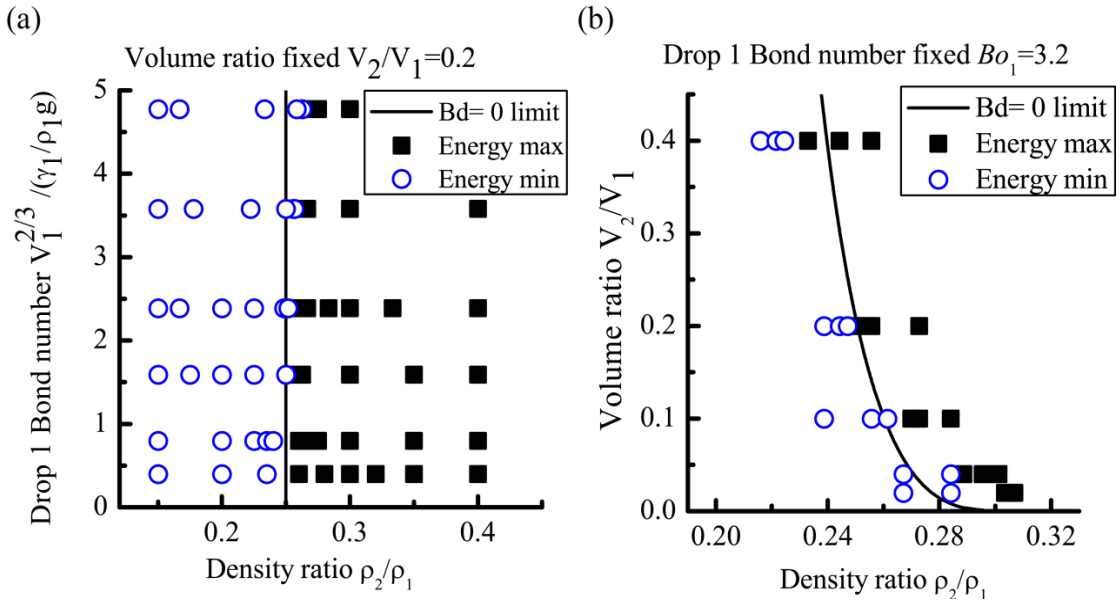

Figure 2.9. The energy maximum and minimum states obtained from Surface Evolver for a high interfacial tension system (γ_{1A} = 72 mN/m, γ_{2A} = 25 mN/m and γ_{12} = 52 mN/m). (a) The volume of the top drop is 1 μL and the bottom drop is 5 μL. The densities of the two drops are varied to achieve different density ratios and Bond numbers. The critical density ratio deviates from the zero Bond number asymptotic prediction as the Bond number increases. (b) The Bond number of the bottom drop is fixed at an intermediate value of 5.8 and the transition from an energy minimum to an energy maximum deviates slightly from the zero-Bond number model at various volume ratios.

density ratios, with a clear transition between the two regions. The vertical line indicates the predicted critical density ratio for this system at fixed volume ratio of 0.2 using the zero Bond number calculation. The figure shows that the zero Bond number approximation predicts the transition from an energy minimum to an energy maximum reasonably well at small Bond number, while a small deviation is observed at increasing Bond number. At a Bond number of $Bo_1 \approx 5$ for Drop 1, the deviation from the zero Bond number predictions is about 4%. This small deviation results from the gravity-driven flattening of the bottom drop, which tends to stabilize the axisymmetric configuration up to a slightly larger critical density ratio.

Based on the earlier dimensional analysis, the critical density ratio also depends on the

volume ratio. Figure 2.9b examines the stability of the axisymmetric configuration for a fixed Bond number of Drop 1 Bo_1 = 3.2, plotting the stability of individual configurations on a plot of volume ratio versus density ratio. As in Figure 2.9a, the stable configurations are found at lower density ratios, while unstable configurations are found at higher density ratios, with a clear transition between the two regions. In this case, the stability transition depends on volume ratio, shifting to lower critical density ratio values for larger volume ratios. The solid line represents the critical density ratio predicted in the zero Bond number limit. While the same trend is observed, the simulations exhibit a small deviation from this limit. The deviation arises from the slight gravity-induced flattening of both the top and bottom drops at non-zero Bond numbers. The deviation observed in Figure 2.9b at zero Bond number is about 2% of the critical density ratio.

Figure 2.10 summarizes the simulation results for a low interfacial tension system to compare whether the predicted critical density ratio obtained from the zero Bond number approximation.. In this case, the surface tension is $\gamma_{2A} = 40\,\text{mN/m}$ for the smaller drop and $\gamma_{1A} = 41\,\text{mN/m}$ for the larger drop. The interfacial tension is $\gamma_{12} = 3\,\text{mN/m}$. The dimensionless surface tension ratios for this case are $\gamma_{2A}/\gamma_{1A} = 0.98$ and $(\gamma_{12} - \gamma_{1A})/\gamma_{2A} = -0.95$. The contact angle for the larger drop against the solid substrate is fixed at $\alpha = 90°$.

In Figure 2.10a, the volume ratio is held fixed at a value of 0.2, and the stable and unstable configurations are marked with open and filled symbols, respectively, as a function of the Bond number of Drop 1 and the density ratio. The simulation results demonstrate the same features as for the high interfacial tension case: i.e., the stable configurations are organized at lower density ratios, while the unstable configurations are organized at higher density ratios, with a clear transition between the two regions. The zero Bond number approximation, denoted by the

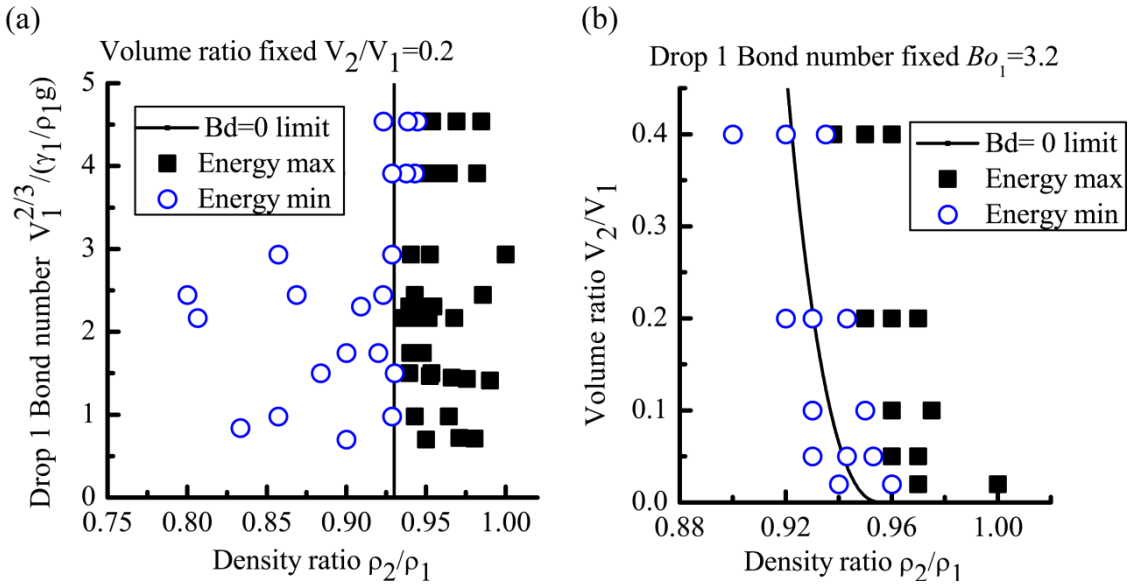

Figure 2.10. The energy maximum and minimum states obtained from Surface Evolver for a low interfacial tension system (γ_{1A} = 41 mN/m, γ_{2A} = 40 mN/m and γ_{12} = 3 mN/m). (a) The volume ratio of the top drop to the bottom drop is fixed at 0.2, and the densities of the two drops are varied to achieve different Bond numbers, yielding different maximum and minimum energy states. The critical density ratio deviates from the zero Bond number asymptotic prediction as the Bond number increases. (b) The Bond number of the bottom drop is fixed at an intermediate value of 5.8 and the transition from an energy minimum to an energy maximum deviates from the zero-Bond number limit at all volume ratios.

vertical line, agrees well with the critical density ratio observed in simulations. The critical value found in simulations deviates about 2% from the zero Bond number value at $Bo_1 \approx 5$ for Drop 1. In Figure 2.10b, the Bond number of Drop 1 is held fixed at Bo_1 =3.2, while the volume ratio varies. In this case, the critical density ratio resulting from the simulations is always larger than the critical density ratio predicted at zero Bond number. This is in contrast to the results shown in Figure 2.9b, where the critical density ratio from simulation is larger than the zero Bond number value at smaller volume ratios, and smaller than the zero Bond number value at large volume ratios.

The deviation of the critical density ratio in simulations compared with the zero Bond

number limit can be attributed to the finite Bond number of Drop 2, $Bo_2 = V_2^{3/2} / (\gamma_2 / \Delta\rho_2 g)$. In Figure 2.9b, the ratio of the Bond numbers near the transition line is $Bo_2 / Bo_1 = 0.72(V_2 / V_1)^{2/3}$, while the ratio of Bond numbers in Figure 2.10b is $Bo_2 / Bo_1 = 0.95(V_2 / V_1)^{2/3}$. Thus, even though the volume ratios for the high and low interfacial tension cases are set to the same value, the Bond number ratios are different as a result of the surface and interfacial tension differences. Nevertheless, the predicted critical density ratio at zero Bond number and the critical density ratio resulting from simulation are only 2 – 4% different, suggesting that the zero Bond number approximation captures the major factors controlling the transition from an energy maximum to an energy minimum.

The simulations show that the critical density ratio is close to the zero Bond number limit for both high and low interfacial tension systems, with merely 2 – 4% deviation for Bond number $Bo_1 \approx 5$. For the high interfacial tension system to reach a stable axisymmetric configuration, the density ratio of the two drops must be smaller than 0.25. For the low interfacial tension system to reach a stable axisymmetric configuration, the density ratio must be smaller than 0.93. In the following section we conduct experiments for real systems in which we tune the density ratios and realize both stable and unstable axisymmetric configurations.

2.5 Experimental Methods and Fluid Properties

The previous analysis and simulations demonstrate that the stability of a compound sessile drop depends strongly on the magnitudes of the surface and interfacial tensions. Validating the predicted critical density ratio in real systems is challenging since fluid and interfacial properties typically cannot be varied independently. In the case of compound metal drops, the density ratio has been adjusted by varying temperature[44]. In aqueous systems, cesium chloride salt can be

Table 2.3. Densities, surface tensions and interfacial tensions of dodecane and aqueous CsCl solutions.

Fluid	Density (g/ml)	Surface tension (mN/m)	Interfacial tension with dodecane (mN/m)
Water	0.9946 ± 0.0032	72.4 ± 0.5	52.2 ± 0.3
20%w/w CsCl	1.1677 ± 0.0035	73.5 ± 0.4	50.1 ± 0.5
40%w/w CsCl	1.4136 ± 0.0027	74.1 ± 0.5	53.9 ± 0.3
60%w/w CsCl	1.7780 ± 0.0023	75.1 ± 0.6	58.3 ± 0.4
Dodecane	0.7431 ± 0.0035	25.3 ± 0.4	–

added to vary the density with minimal viscosity and surface tension changes[65, 66]. To experimentally verify the stability criterion, we examine two liquid pairs, one with high interfacial tension and one with low interfacial tension. In each case the density is varied using different concentrations of cesium chloride salt added to the aqueous phase, allowing the critical density ratio to be determined for a (almost) fixed set of surface and interfacial tension values.

The high interfacial tension system consists of dodecane paired with aqueous cesium chloride (CsCl, purchased from Sigma-Aldrich with purity ≥ 99%, used as received) solutions. Dodecane and water systems have previously been used to verify the Neumann's angle calculation[67] and exhibit relatively large interfacial tension values of about 52 mN/m. The fluid and interfacial properties of each liquid considered are listed in Table 2.3. Dodecane (Sigma-Aldrich, purity ≥

99%) is further purified using column chromatography over aluminum oxide and silica. The chromatography materials are obtained from Sigma-Aldrich and used as received. The CsCl solutions are prepared by mixing deionized water (Milli-Q, 18MΩ-cm, organic content < 10 ppb) with an appropriate mass of CsCl. Densities are determined by measuring the mass (Denver Instrumental Company Balance, Model XE-100A, accuracy 10^{-4} g) of a known volume contained in a volumetric flask (Pyrex No. 5640, 25 ± 0.03 ml). Experimental uncertainty is estimated based on propagation of error from different experimental sources, including instrumental error from the volumetric flask of about 0.1% with statistical error is about 0.05%, and instrumental error from the mass balance of about 0.02% with statistical error about 0.03%. Estimated uncertainties are in the fourth decimal place of the reported density values. Surface and interfacial tension values are measured using a Du Noüy ring tensiometer[68]. The measured values for dodecane and water agree well with reported literature values[67].

The low interfacial tension system is obtained by inducing phase separation of partially miscible fluids[58, 69]. Low interfacial tension values are common in colloid-polymer[70–74] and polymer-polymer[75–78] mixtures that undergo phase separation, leading to two immiscible liquid components with interfacial tension values as low as 1 μN/m. Mixing water with alcohols such as benzyl alcohol or 1-butanol leads to phase separation into water-rich and alcohol-rich liquid phases with interfacial tension values of 1 – 4 mN/m.[58, 69, 79] Although the phase diagram of the 1-butanol–water mixture is well characterized[79] and the interfacial tension value is only 1.8 mN/m[58], 1-butanol has a relative high vapor pressure of 665 Pa at 20 ºC [80]. To avoid evaporation in the compound sessile drops, we select benzyl alcohol, which exhibits a low vapor pressure of 12 Pa at 25 ºC[81]. The benzyl alcohol is obtained from Sigma-Aldrich (purity ≥ 99%) and used as received. To form the immiscible liquid pairs, aqueous CsCl solutions are mixed with benzyl

Table 2.4. Density of each liquid component collected from the phase-separated mixture of benzyl alcohol and aqueous CsCl solution with similar volumes.

Liquid pair	Water rare phase (g/ml)	Water rich phase (g/ml)
Benzyl-OH & water	1.0344 ± 0.0025	0.9968 ± 0.0034
Benzyl-OH & 6%w/w CsCl	1.0386 ± 0.0021	1.0470 ± 0.0022
Benzyl-OH & 10%w/w CsCl	1.0389 ± 0.0021	1.0869 ± 0.0023
Benzyl-OH & 14%w/w CsCl	1.0402 ± 0.0020	1.1253 ± 0.0023
Benzyl-OH & 18%w/w CsCl	1.0404 ± 0.0021	1.1658 ± 0.0027
Benzyl-OH & 22%w/w CsCl	1.0402 ± 0.0021	1.2102 ± 0.0036
Benzyl-OH & 26%w/w CsCl	1.0422 ± 0.0020	1.2613 ± 0.0067

alcohol at similar volumes. Upon equilibration, the mixture separates into two phases, one that is water and salt rich, and one that is water and salt rare. Agreeing with the results by Phan *et al.* [33, 34], multiple drops of the more dense phase are observed to float on the less dense phase in bulk. The floatability of more dense drops on top of the less dense phase in bulk is achieved by the distortion of the lower fluid phase. The two phases are collected using a separation funnel. The water rich and water rare phases are identified by miscibility: the water rich phase is miscible with addition of water, but separates into two phases if extra benzyl alcohol is added.

Table 2.4 lists the densities measured for each of the two liquid phases obtained by mixing different concentrations of CsCl solution with benzyl alcohol. The density is measured using the method described earlier. Note that the water rich phase obtained from the benzyl alcohol-water

mixture is of lower density than the water rare phase, because benzyl alcohol is denser than water. However, since CsCl salt is more soluble in the water rich phase, the water rich phase obtained from the benzyl alcohol-CsCl solution is denser than the water rare phase without CsCl, as seen in the second and third row of Table 2.4. The density ratio of the less dense fluid to that of the more dense fluid first increases from 0.964 to approximately 1, and then decreases to about 0.826 as the concentration of CsCl increases. The highest concentration of CsCl obtained in solution is 26%. For concentrations greater than 30%, we observe crystallization of CsCl upon mixing with benzyl alcohol, even though in principle saturation is not achieved until 60% CsCl in the two-element CsCl-water system[65].

The measurements of surface and interfacial tensions are listed in Table 2.5, where the water rich phase always exhibits a higher surface tension than the water rare phase. The interfacial tension between the water rare phase and water rich phase increases slightly as the concentration of CsCl increases.

Compound sessile drops are examined for the fluid pairs discussed, and are placed on solid hydrophobic surfaces exhibiting a contact angle of 102 ± 5 º with deionized water. The surfaces are prepared by applying Aquapel™ (PPG Industries) to microscope glass slides (Fisherbrand 12-567) following the manufacturer instructions. The surface is robust against rinsing with ethanol or acetone.

The formation and stability of compound sessile drops are recorded using a CCD camera (Q-See, Anaheim CA, model no. QPSCDNV, 30 fps mounted with a 55mm telecentric lens from Edmund Optics) oriented at a 45º angle to the horizontal surface. A first drop of specified volume (10 – 100 μL) is deposited on the hydrophobic surface using a pipette (Eppendorf 100 μL pipette with maximum systematic and random error of 0.8 ± 0.3 μL) and allowed to reach its

Table 2.5. Surface and interfacial tension measurements for the two liquid phases obtained from phase separated mixtures of benzyl alcohol and aqueous CsCl solutions with similar volumes.

Liquid pair	Surface tension of water rare phase (mN/m)	Surface tension of water rich phase (mN/m)	Interfacial tension of two phases (mN/m)
Benzyl-OH & water	39.5 ± 0.5	41.5 ± 0.6	3.0 ± 0.3
Benzyl-OH & 6%w/w CsCl	38.6 ± 0.4	40.2 ± 0.5	5.0 ± 0.3
Benzyl-OH & 10%w/w CsCl	38.9 ± 0.5	40.5 ± 0.5	5.1 ± 0.2
Benzyl-OH & 14%w/w CsCl	38.6 ± 0.5	41.0 ± 0.3	5.3 ± 0.3
Benzyl-OH & 18%w/w CsCl	39.0 ± 0.4	41.6 ± 0.4	5.8 ± 0.3
Benzyl-OH & 22%w/w CsCl	39.5 ± 0.3	41.9 ± 0.3	6.2 ± 0.2
Benzyl-OH & 26%w/w CsCl	39.3 ± 0.3	42.3 ± 0.5	6.6 ± 0.4

equilibrium configuration. A second drop of smaller volume (2 – 80 μL) is deposited using two different pipettes depending on the desired volume (Eppendorf 20 μL pipette with error 0.2 ± 0.1 μL, or Eppendorf 100 μL pipette with error 0.8 ± 0.3 μL). Upon deposition, if the second drop slides off the apex of the lower drop, then this combination is documented as an unstable configuration. If the second drop remains at the axisymmetric configuration, then the pipette tip is used to further perturb the top drop from the apex without permitting it to touch the solid substrate. If the second drop restores to the apex at least three times, then this combination is documented as a stable axisymmetric configuration. If the restoration cannot be repeated, the

combination is documented as an uncertain condition. The Bond number of the bottom drop is in the range of $1 < Bo_1 < 6$.

2.6 Experimental Results for the Stability of Compound Sessile Drops

Both the zero Bond number analysis and Surface Evolver simulations demonstrate that the stability of an equilibrium axisymmetric configuration can be predicted by comparing the density ratio of two drops with the critical density ratio calculated for the specified fluid system. The critical density ratio of a high interfacial tension system is significantly different from that of a low interfacial tension system. In this section, we first describe the experimental realization of stable and unstable compound sessile drops for both the low and high interfacial tension systems described in the previous section. The transition from stable to unstable configurations is then compared quantitatively with the asymptotic approximation and the simulations.

For the high interfacial tension system consisting of dodecane and aqueous CsCl solutions, all the experiments exhibit unstable axisymmetric configurations: once the smaller drop is deposited on top of the larger drop, it slides off to the side and forms a Janus configuration.

A typical experiment is shown in Figure 2.11. A dodecane drop of 2 μL is deposited on top of a 60% CsCl drop of 50 μL at t =12.5 s; and at time t = 12.93 s, the dodecane drop is slightly away from the apex position; by the time t = 13.03 s, the dodecane drop toches the solid glass surface with Aquapel coating; finally at t = 14.00 s, the Janus configuration is the equilibrium configuration of the compound sessile drop. From the zero Bond number analysis, the critical density ratio is approximately 0.24 – 0.30 for all of the volume ratios considered. However, experimentally, the accessible density ratio range is 0.41 – 0.75, well above the theoretical transition value. Thus, the observation that no stable axisymmetric configurations are

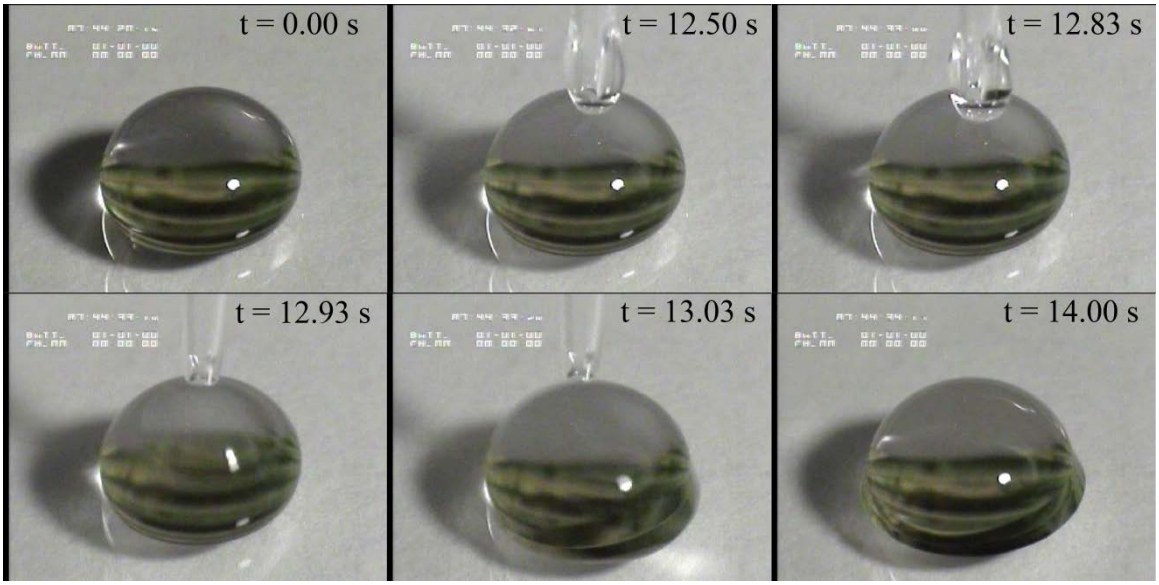

Figure 2.11. Janus shape of a compound sessile drop formed using dodecane and a 60% CsCl solution in water, with density ratio 0.42. Upon deposition using a pipette, the smaller drop slides off to the side.

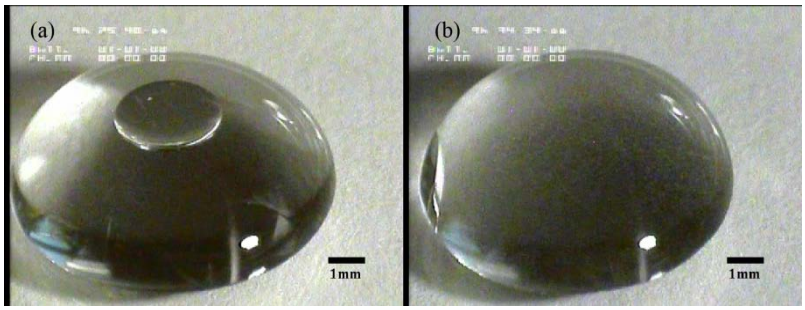

Figure 2.12. (a) Stable axisymmetric configuration using two liquid phases obtained from a phase separated mixure of aqueous 22% CsCl solution with benzyl alcohol, density ratio 0.859. (b) Janus shape of compound sessile drop using two liquid phases obtained from a phase separated mixture of aqueous 10% CsCl solution with benzyl alcohol, density ratio 0.955.

experimentally realized for the high interfacial tension system is in agreement with both analysis and simulations.

For the low interfacial tension system of the phase separated mixtures of benzyl alcohol and

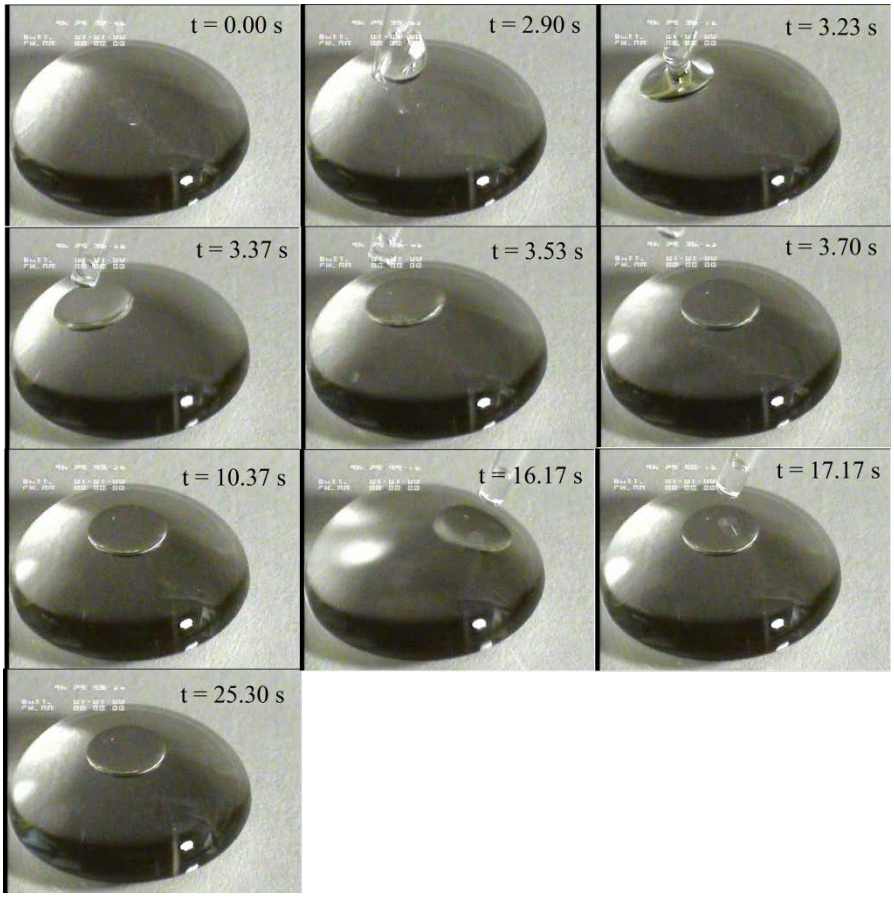

Figure 2.13 A stable axisymmetric compound drop configuration. With perturbations induced by pipette, the top drop still restores to the apex position. The fluids are two immiscible phases resulting from a mixure of 22% CsCl solution with benzyl alcohol, with density ratio of 0.859.

aqueous CsCl solutions, both unstable and stable axisymmetric configurations are observed. Figure 2.12 compares the final configurations for the two experiments of low interfacial tension fluid systems with difference in density ratio while surface and interfacial tensions are almost the same. Figure 2.12a shows a stable axisymmetric configuration while Figure 2.12b shows that the axisymmetric configuration is not stable and a Janus configuration forms after depositing one drop on top of another drop. Different frames of both the experiments are shown in Figure 2.13 and Figure 2.14.

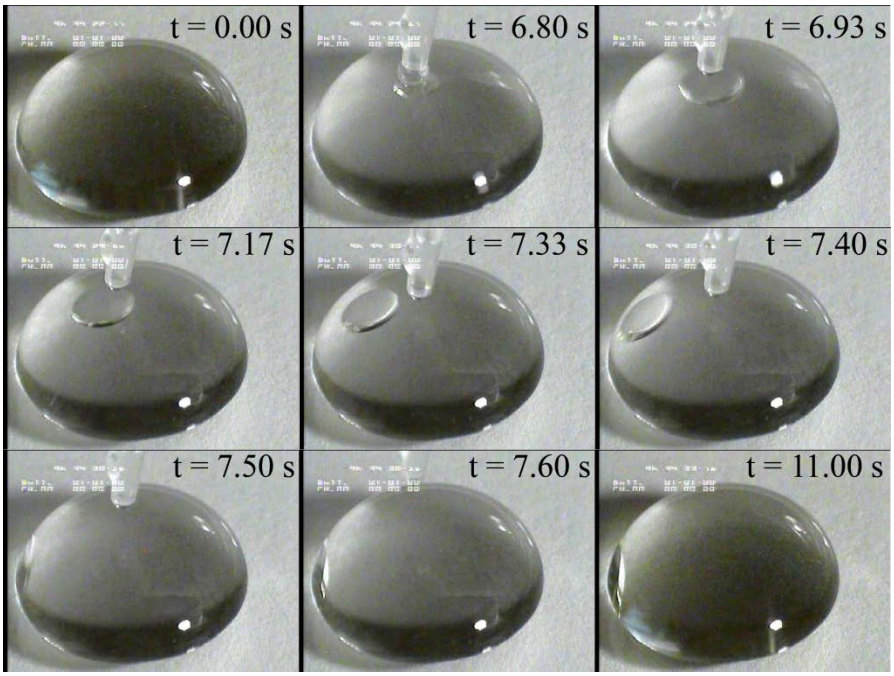

Figure 2.14. Janus shape of a compound sessile drop obtained using two immiscible phases obtained from a mixture of 10% CsCl in water with benzyl alcohol, with density ratio of 0.955. Upon deposition using a pipette, the smaller drop immediately slides off to the side.

Figure 2.13 shows a typical example of a stable configuration for the liquid pairs obtained by mixing benzyl alcohol and 22% aqueous CsCl solution. At time t = 2.90 s, a 2 μL drop of the water rare phase is deposited onto a 50 μL drop of the water rich phase; at time t = 3.37 s, the water rare phase drop is fully detached from the pipette tip; the water rare phase drop then slowly climbs to the apex position as seen at frames of t = 3.53 s and t = 3.70 s; the compound sessile drop assumes this stable axisymmetric position as depicted at t = 10.37 s. Even though a perturbation is applied to the top drop using the pipette tip at t = 16.17 s, the later frame at t = 17.17 s shows the water rare phase drop restores to the axisymmetric position and the compound drop maintains the axisymmetric equilibrium configuration until the end of the experiment t = 25.30 s. The experimental density ratio for the two drops is 0.859, less than the predicted critical

density ratio of $\rho_2 / \rho_{1\text{crit(ana)}} = 0.878$. This experimental phenomenon agrees with the theoretical analysis that deposition of a drop of the water rare phase onto a drop of the water rich phase results in an axisymmetric configuration that is stable against perturbations from the apex.

In contrast, as shown in Figure 2.14, the axisymmetric configuration is not stable for the liquid pairs obtained by mixing benzyl alcohol and 10% aqueous CsCl solution. A 2 μL drop of the water rare phase drop is deposited on the top of a 50 μL drop of the water rich phase at t =6.80 s; and at time t = 6.83 s, the water rare phase drop is slightly away from the apex position; the water rare phase drop quickly slides off to the side as shown in the time frames t = 7.17 s through t = 7.50 s; at time t = 7.60 s, the water rare phase drop touches the solid glass surface which is almost identical to the final equilibrium configuration at t = 11.00 s. The experimental density ratio is 0.955, greater than the predicted critical density ratio of $\rho_2 / \rho_{1\text{crit(ana)}} = 0.896$, which agrees with the analysis that deposition of a drop of the water rare phase onto a drop of the water rich phase yields an unstable axisymmetric configuration.

The observed transition from an energy minimum to an energy maximum encourages quantitative experimental comparisons with both the analysis and the simulations. Figure 2.15 summarizes the experiments including both stable and unstable axisymmetric configurations for the phase separated mixture of benzyl alcohol and varying concentrations of aqueous CsCl solution. Each symbol denotes a liquid pair obtained from the phase separated mixture with the specified concentration of CsCl. The open symbols represent stable axisymmetric configurations (energy minimum) and the filled symbols represent unstable axisymmetric configurations (energy maximum). The volumes of both drops are varied to achieve different Bond numbers of the bottom drop Bo_1 and different volume ratios. The Bond number of Drop 1 has a practical

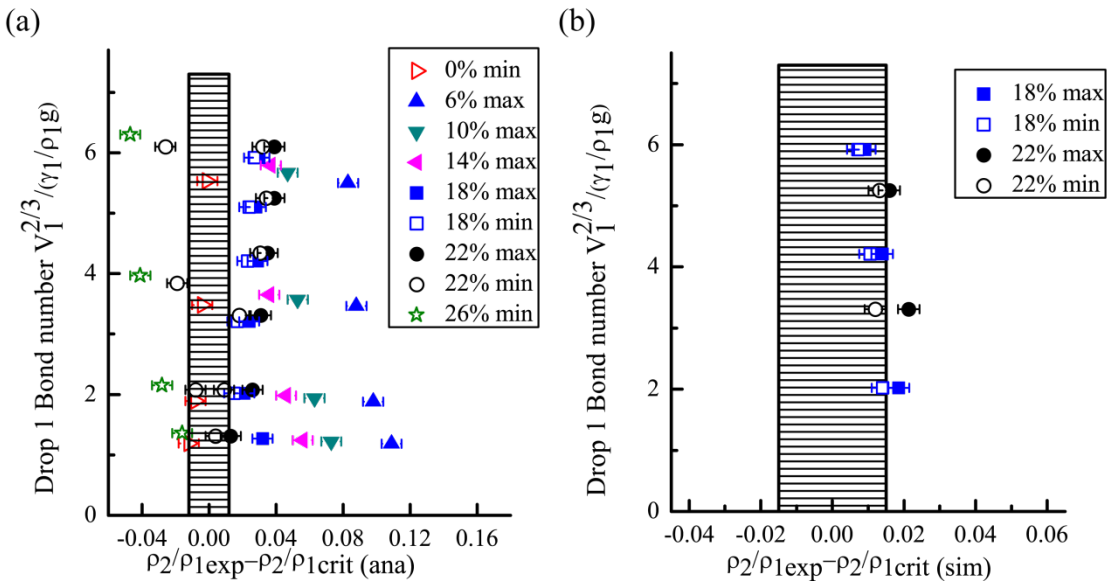

Figure 2.15. a) Summary plot of benzyl alcohol experiments compared with the zero Bond number analytical model. The vertical axis is the Bond number of Drop 1 and the horizontal axis represents the difference between the experimental density ratio and the critical density ratio predicted in the zero Bond number limit. The open symbols denote energy minima while the filled symbols denote energy maxima. b) Comparison of experimental results with Surface Evolver simulations for the systems using 18% and 22% CsCl solutions. The horizontal axis indicates the difference between the experimental density ratio and the critical density ratio obtained in simulations.

lower limit $Bo_1 \approx 1$, because smaller drops are difficult to deposit using the pipettes described earlier. All of the experiments in Figure 2.15 consider the deposition of a less dense fluid drop onto a more dense fluid drop. In the opposite case, deposition of a more dense drop onto a less dense drop always resulted in experimentally unstable configurations, which agrees with Equation (2.16).

Figure 2.15a compares the experimental results with the zero Bond number analysis. The critical density ratios in the zero Bond number limit ((Equation (2.18)) are calculated using the relevant experimental values of surface and interfacial tensions, volume ratios and contact angle

for each fluid pair. In the experiments, the experimental density ratio is determined once the fluid pair is selected; in contrast, the analysis formulates the critical density ratio as a function of the volume ratio. The horizontal axis of Figure 2.15a represents the difference between the experimental density ratio and the predicted critical density ratio from the zero Bond number analysis $\rho_2 / \rho_{1\text{exp}} - \rho_2 / \rho_{1\text{crit(ana)}}$. The vertical axis represents the Bond number of Drop 1 $Bo_1 = V_1^{2/3} / (\gamma_{1A} / \Delta\rho_{1A} g)$. For all of the drop volumes tested, the axisymmetric configurations for the liquid pairs obtained by mixing benzyl alcohol with 0% and 26% aqueous CsCl solutions are always stable. The axisymmetric configurations for the liquid pairs obtained by mixing benzyl alcohol with 6%, 10% and 14% aqueous CsCl solutions are always unstable. Transitions from an energy minimum to an energy maximum are observed for the liquid pairs obtained using 18% and 22% aqueous CsCl solutions. From the zero Bond number analysis, a positive value of the density ratio difference $\rho_2 / \rho_{1\text{exp}} - \rho_2 / \rho_{1\text{crit(ana)}}$ is expected to result in an energy maximum, while a negative value is expected to result in an energy minimum. The uncertainty in the experimental density ratio is about ± 0.003 due to the uncertainty in the density measurements. The vertical shaded area shown in Figure 2.15a near zero on the horizontal axis indicates the expected stable-to-unstable transition, reflecting the estimated uncertainty ($\approx \pm 0.012$) in calculating $\rho_2 / \rho_{1\text{crit(ana)}}$ based on the uncertainty in the surface and interfacial tensions and in the volume ratios used in Equation (2.18). For the cases in which the Bond number is near unity, $Bo_1 \approx 1$, the transition from an energy minimum to an energy maximum occurs at $\rho_2 / \rho_{1\text{exp}} - \rho_2 / \rho_{1\text{crit(ana)}} \approx 0$, suggesting that the experimental results agree well with the zero Bond number analysis. For the larger Bond number cases, $Bo_1 \approx 6$, the experimental transition occurs at $\rho_2 / \rho_{1\text{exp}} - \rho_2 / \rho_{1\text{crit(ana)}} \approx 0.03$, so the experiments deviate slightly from the zero

Bond number prediction.

The experimental results are also compared with finite Bond number Surface Evolver simulations in Figure 2.15b for the fluid systems obtained by mixing 18% and 22% aqueous CsCl solutions with benzyl alcohol. In this case, the horizontal axis represents the difference between the experimental density ratio and the critical density ratio obtained from simulations $\rho_2 / \rho_{1\text{exp}} - \rho_2 / \rho_{1\text{crit(sim)}}$. Appendix 2.3 lists all the simulation results for energy maximum and energy minimum in comparison with the experimental results. As before, the uncertainty in the experimental density ratio is ± 0.003. The uncertainty in the predicted critical density ratio from simulations, shown as the shaded region in Figure 2.15b, is ± 0.015. The uncertainty for the simulations is slightly larger than that of the zero Bond number prediction owing to the limited ability of Surface Evolver to resolve the critical value. The numerical gap in the density ratios of the nearest observed energy maximum and minimum configurations is approximately 0.003 – 0.004 in our Surface Evolver simulations. In Figure 2.15b, the experimentally realized transition from an energy maximum to an energy minimum overlaps well with the shaded region, demonstrating that the experimental results agree well with the simulations independent of the Bond number of the bottom drop. Although within uncertainty, it is noted that the critical density ratio difference tends to cluster at the positive edge of the shaded region, hinting that the spherical cap shape perturbations used in the simulations may yield a small systematic offset as compared with the experiments using pipettes to realize the perturbations. Further investigation of this possible systematic offset is beyond the scope of this paper and would require a more general stability analysis.

Similar experiments to examine the transition from energy minimum to energy maximum could also be performed using the phase-separated mixture of butanol and aqueous CsCl

solutions. Besides the advantage of the low vapor pressure of benzyl alcohol, which minimizes evaporation, benzyl alcohol also has a density greater than water. For mixtures of butanol and aqueous CsCl solutions, increasing the concentration of CsCl causes the experimental density ratio to monotonically decrease; therefore the axisymmetric configuration will be more stable as the CsCl concentration increases. In contrast, the density ratio obtained from the mixtures of benzyl alcohol and aqueous CsCl solutions first increases to approximately 1 and then decreases to about 0.826, indicating that the axisymmetric configuration first becomes less stable and then more stable as the concentration of CsCl increases. Thus the benzyl alcohol mixtures permit the stable-to-unstable transition to be realized more easily.

Figure 2.15 shows that the zero Bond number analysis, the Surface Evolver simulations, and the experiments all agree well in the observed and predicted transition from energy minimum to energy maximum compound drop configurations. At high Bond numbers, both the experiments and the Surface Evolver simulations indicate that the critical density ratio deviates from that obtained in the zero Bond number limit by approximately 3 – 4%. Perturbing the compound sessile drop using a pipette tip is more likely to represent a generic perturbation in which axisymmetry is broken, and interface shapes are not restricted to either spherical caps or Laplacian shapes. Nevertheless, good agreement is found when comparing the stability criterion obtained for each of the three types of perturbations.

2.7 Summary

In this chapter, we have determined the seven dimensionless parameters that govern the shape of an axisymmetric compound sessile drop using the Laplace equations. Following a Laplacian shape perturbation, a stability criterion for the axisymmetric configuration is

determined in the zero Bond number limit. This stability criterion is verified using both Surface Evolver simulations and experiments for both high and low interfacial tension systems.

For an axisymmetric compound drop to be stable, the density ratio must be smaller than a critical density ratio that depends on the surface and interfacial tensions, and the drop volumes. The critical density ratio is small for a high interfacial tension system, therefore stable axisymmetric configurations are rarely observed for organic/inorganic compound sessile drops in air. The critical density ratio is much larger for low interfacial tension systems, allowing the possibility for experimental realization of stable configurations. We successfully observed stable axisymmetric compound sessile drops using a low interfacial tension system obtained from phase-separated mixtures of benzyl alcohol and aqueous CsCl solutions. The low interfacial tension systems show a transition from energy minimum to energy maximum by varying the CsCl concentration, which varies the density ratio without significantly changing the surface and interfacial tensions. The critical condition for transition between the stable and unstable axisymmetric configurations agrees closely in the small Bond number cases for all three approaches: the zero Bond number analysis, the Surface Evolver simulations, and the experiments. The simulations and experiments exhibit a small deviation from the zero Bond number predictions at larger Bond numbers.

The ability to form a stable axisymmetric compound sessile drop may be useful in designing liquid lens systems for soft optics. Interestingly, the stability analysis predicts that a more dense drop resting on top of a less dense drop is never stable, even though a more dense drop is observed to float on top of a less dense bulk fluid using the low interfacial tension system obtained from phase separated mixtures of benzyl alcohol and aqueous CsCl solutions. Further investigation of this low interfacial tension system may provide a better understanding of the

flotation mechanism of dense objects through the distortion of surfaces.

Even though stable axisymmetric compound sessile drops were experimentally observed for the low interfacial tension system, these stable compound sessile drops are always achieved by depositing one drop on top of another drop. No stable axisymmetric configurations were obtained through side-to-side coalescences of the same fluid systems; only Janus configurations are observed. It is probable that side-to-side coalescence resulted in a lower energy minimum state of Janus configuration than the axisymmetric configuration. In the next chapter, we investigate the dynamics of drop coalescence, especially the side-to-side coalescence, to analyze the impact of gravitational force in the final drop configuration.

Appendix 2.1 Mathematica code for calculating critical density ratio

```
(* This command deletes the previous storage of variables and values*)
    ClearAll[gamma1,gamma2,gamma12,phi13,phi12,phi23,Rratio,radiusRatio,
        Rratiosol,gar2,gar1,volume2,volume1,radius,r12,r23,r13,theta12,theta112,
        delta,volumeRatio,densityratio,DensityRatio,angle,f,phi12angle,phi13angle,
        phi23angle]
(*Function returns the value of the critical density ratio for the case of 90 degree contact angle*)
(*Follow the derivation of compound sessile drop Chapter 2*)
(*gamma1 defines the surface tension of Drop 1*)
(*gamma2 denotes the surface tension of Drop 2*)
(*gamma12 denotes the interfacial tension between Drop 1 and Drop 2*)
(*volumeRatio denotes the ratio of the volume of Drop 2 to the volume of Drop 1*)
(*Rratio is the ratio of the radius of curvature of the top drop to that of the bottom drop*)
(*Note the Mason and Torza paper has defined r13 can be positive or negative, but in this
calculation, we assume r13 to be positive while phi13 can change sign, this results in the
difference from equation [16] in Torza and Mason's paper *)
(*we use the convention that the radius of curvature can only be positive*)
(*note as Drop 1 is in contact with solid surface, phi23 will always be positive*)
    DensityRatio[gamma1_,gamma2_,gamma12_,volumeRatio_]:= (
        gar2=gamma2/gamma12;
        gar1=gamma1/gamma12;
        theta12=Pi-ArcCos[(gar1^2+gar2^2-1)/(2gar1*gar2)];
        theta112=Pi-ArcCos[(1+gar1^2-gar2^2)/(2gar1)];
        phi23=ArcSin[Sqrt[4*gar2^2*gar1^2-(1-gar2^2-gar1^2)^2]/2/
            (gar1*gar2*(gar1*gar2(Rratio^2+1)-Rratio(gar1^2+gar2^2-1)))^0.5
            *Rratio];
        phi12=theta12-phi23;
        phi13=Pi-theta112-phi23;
        r12=radius/Sin[phi12];
        r13=radius/Abs[Sin[phi13]];
```

```
        r23=radius/Sin[phi23];
(*Note for the volume2 calculation, the angle for phi12 can be smaller or larger than 90 degree. For benzyl-oh system because the angle theta212 is very small, thus, the angle of phi12 is more than 90 degree*)
        volume2=Pi/3*(r12^3(2+Cos[phi12]*(3-Cos[phi12]^2))
            +r13^3(2-Cos[phi13]*(3-Cos[phi13]^2)))
            *phi13/Abs[phi13];
        volume1=Pi/3*(r23^3*Cos[phi23]*(3-Cos[phi23]^2)
            -r13^3(2-Cos[phi13]*(3-Cos[phi13]^2)))
            *phi13/Abs[phi13];
        Rratiosol=FindRoot[volume2/volume1-volumeRatio,{Rratio,0.3,0.943}];
(*Replace the Rratio with the solution from this numerical solution of Rratiosol*)
        radiusRatio=Rratio/.Rratiosol[[1]];
(*the Neumann angles between gamma1, gamma2,gamm12 and are denoted as theta12, theta112,theta12*)
(*delta is the angle as defined in Figure 2.1 and Figure 2.5*)
        delta=ArcSin[Sqrt[4*gar2^2*gar1^2-(1-gar2^2-gar1^2)^2]/
            2/(gar1*gar2*(gar1*gar2(radiusRatio^2+1)
            -radiusRatio(gar1^2+gar2^2-1)))^0.5*(gar2-radiusRatio*gar1)];
(*f[angle] is a function to calculate the dimensionless volume based on the basal angle*)
        f[angle_]:=(2-3*Cos[angle]+Cos[angle]^3)*Csc[angle]^3;
(*critical density ratio from Equation (2.18)*)
        densityratio=N[(f[Pi-theta112-delta]+f[delta])
            /(f[2*Pi-theta112-delta-theta12]+f[delta])];
(*output the predicted critical density ratio in this function*)
        Densityratio)
(*the function ends with a right parenthesis*)
(*test case for gamma1=1, gamma2=0.6, volume ratio=0.2 with different interfacial tensions*)
        table=Table[{x,DensityRatio[1,0.6,x,0.2]},{x,0.405,1.595,0.005}];
        Export["critical density ratio on interfacial tension 0.6.xls",table]
(*plot for the shape of critical density ratio for a different set of interfacial tensions*)
```

DiscretePlot[DensityRatio[1,0.4,x,0.2],{x,0.605,1.395,0.001}]

Appendix 2.2 Surface Evovler code for compound sessile drop stability

```
// Should refine and then remove small edges to make the grids more smooth and then run the
fall events to check. The command for refining is r, and the command for removing edges is t,
while the command for merging small triangles is w. A prompt command window may pop up
for the specified threshold of length or area. The command h gives the histograms
// Evolver data for drop of prescribed volume sitting on a deformable surface with gravity.
// the interface is defined on constraint 1, where z equals 0 at all time
// Contact angle with plane can be varied.
    PARAMETER angle1 = 90       // interior angle between plane and surface, degrees
    PARAMETER angle2 = 90       // interior angle between plane and surface, degrees
    parameter AA = 2            // initial drop size, mm
    parameter HH = 2            // external frame size, m
    parameter TT = 4            // external frame size
    gravity_constant 0          // start with gravity off

    #define WALLT1   (-cos(angle1*pi/180))   // virtual tension of facet on plane
    #define WALLT2   (-cos(angle2*pi/180))   // virtual tension of facet on plane
    #define alfa1    angle1*pi/180
    #define alfa2    angle2*pi/180
    #define gSL = (sin(pi-alfa1))/sin(pi-alfa2))          // solid liquid energy
    #define gSV = (sin(alfa1+alfa2))/sin(pi-alfa2))      // solid vapor energy
    constraint 1 /* the table top for Drop 1 */
    formula: x3 = 0          //this defines the contact angle
    energy:
    e1: -(WALLT1*y)
    e2: 0
    e3: 0
    vertices
    1     0.0    0.0 HH        /* 4 vertices on plane */
```

```
2      AA    0.0 HH
3      AA    AA    HH
4      0.0 AA    HH
5      0.0    0.0 TT
6      AA    0.0 TT
7      AA    AA TT
8      0.0    AA TT
15    0.0    0.0 0.0      constraint 1
16    AA    0.0 0.0      constraint 1
17    AA    AA 0.0      constraint 1
18    0.0    AA 0.0      constraint 1

edges    /* given by endpoints and attribute */
1      1 2              /* 4 edges on plane */
2      2 3
3      3 4
4      4 1
5      5 6
6      6 7
7      7 8
8      8 5
9      1 5
10    2 6
11    3 7
12    4 8
25 15 16      constraint 1
26 16 17      constraint 1
27 17 18      constraint 1
28 18 15      constraint 1
29    1 15
30    2 16
```

```
31    3 17
32    4 18
faces    /* given by oriented edge loop */
1      1 10 -5    -9      color red density 3.95
2      2 11 -6 -10 color red density 3.95
3      3 12 -7 -11 color red density 3.95
4      4    9 -8 -12 color red density 3.95
5      5    6    7      8 color red density 3.95
6      -1    29    25 -30 color blue density 4.19
7      -2    30    26 -31 color blue density 4.19
8      -3    31    27 -32 color blue    density 4.19
9      -4    32    28 -29 color blue    density 4.19
11    1 2 3 4 color green density 0.62
//17    33 34 35    36    no_refine density 7        color clear fixed /* table top for display */

bodies    /* one body, defined by its oriented faces */
1    6 11    9    7 8      volume 50        density 1.210
2    1 5    2 3 4 -11      volume 10        density 1.04

read                    // defining new commands for fast processing
re := {refine edges where on_constraint 1 }

gogo := {g 10; u; V 2;u; r;g 10; u; V; g 50; u; V 2; u; g 50; u; V 2;u; g 30; g 100; u; V 2; u ;
g 100; u; V; g 100; u;V 2; u; r; g 100;}
gogo2:=    {g 5; u; V; g 10; u; V; g 50; u; V; u; V; g 50; u; V; u; V; g 30; g 100; u; V; u; V;
g 100; u; V; g 100; u;V; u; V; g 100; u; V; g 50}

disp:={set vertex y y+0.1 where z>0.9;gogo2}    //Peturb the top drop to the side
fall:={G 0.98; gogo2 30}    //examine whether top drop slides off or recovers
```

Appendix 2.3 Summary table of Surface Evolver simulations

Table A.2.3.1 Simulation and experimental data for the fluid pair of 18% CsCl and benzyl alcohol mixture. V_1 and V_2 represent the volumes of Drop 1 and Drop 2 respectively. “Evolver density ratio min” indicates the largest simulation density ratio achieved for a minimum energy configuration while “Evolver density ratio max” indicates the smallest simulation density ratio achieved for a maximum energy configuration. The Evolver critical density ratio is the average of “Evovler density ratio min” and “Evolver density ratio max”. The analytical critical density ratio is the value obtained through the zero Bond number approximation. The experimental density ratio is the density ratio of the two separated phases.

V_1 (μL)	V_2 (μL)	Drop 1 Bond number	Evolver density ratio min	Evolver density ratio max	Evolver critical density ratio	Analytic. critical density ratio	Experi. density ratio
100	15.0	5.9	0.877	0.886	0.882	0.865	0.892
100	17.5	5.9	0.876	0.885	0.880	0.862	0.892
60	7.5	4.2	0.873	0.883	0.878	0.868	0.892
60	10.0	4.2	0.870	0.880	0.875	0.863	0.892
20	1.5	2.0	0.867	0.879	0.873	0.875	0.892
20	2.5	2.0	0.863	0.876	0.870	0.868	0.892

Table A.2.3.2 Simulation and experimental data for the fluid pair of 22% CsCl and benzyl alcohol mixture. Notations are the same as described in Table A.2.3.1

V_1 (μL)	V_2 (μL)	Drop 1 Bond number	Evolver density ratio min	Evolver density ratio max	Evolver critical density ratio	Analytic. critical density ratio	Experi. density ratio
80	65	5.2	0.833	0.847	0.840	0.823	0.860
80	70	5.2	0.833	0.841	0.837	0.822	0.860
40	25	3.3	0.831	0.841	0.836	0.829	0.860
40	30	3.3	0.827	0.839	0.833	0.824	0.860

Chapter 3 Gravity Driven Flow during Drop Coalescence[2]

3.1 Introduction

When two drops composed of the same material touch, surface tension drives a motion to form a fused drop with smaller surface area. This dynamic behavior of drop coalescence is important to numerous natural and technological processes.[2, 3] Analysis based on photographic and visual observations of water drop collisions illustrates the dynamics of raindrop growth, which are mainly attributed to drop coalescence.[82] Another classic process caused by drop coalescence is sintering, i.e. the merging of particles into homogeneous materials is induced by heating.[83] Other technological applications involving drop coalescence include spray coating[84, 85], ink-jet printing[86], etc. A comprehensive list of drop coalescence applications can be found in the book *Dynamics of Droplets* by Frohn and Roth[2].

Because of the gravitational and frictional forces, the coalescence behaviors of drops in air are typically observed for rain drops with different velocities and accelerations, as the control of physical parameters is difficult.[82, 87–89] To gain a better understanding of the dynamic coalescence behavior, the coalescence of drops suspended in a fluid medium has been examined extensively[83, 90–93]. However, it was found that the coalescence for two drops does not start spontaneously if the drops are surrounded in another fluid phase. This retardation behavior is attributed to the presence of a thin film of the surrounding fluid between the two drops.[92, 93] To avoid the complexity of singular motion in the film drainage during drop coalescence[94, 95], an alternate way

[2] Adapted with permission from Ying Zhang, Samuel D. Oberdick, Ellen R. Swanson, Shelley L. Anna and Stephen Garoff. Gravity driven current during the coalescence of two sessile drops. Phys. Fluids 27, 022101 (2015).

is to study the coalescence of sessile drops where at least one drop is resting on a solid surface. The coalescence of two sessile drops on a solid surface adds the feature that the contact lines of the drops must move during the merging process.[17] Thus, contact line dynamics add richness and complexity to the coalescence of sessile drops discussed in this chapter.

The stability analysis of axisymmetric compound sessile drops in Chapter 2 demonstrated that the critical density ratio is larger for smaller interfacial tension systems. In the limit of zero interfacial tension and equal surface tension for both drops, the critical density ratio reaches the limiting value of 1. This suggests that axisymmetric configurations can be stable as long as the top drop is just slightly less dense for ultralow interfacial tension system. The relative low interfacial tension system is achieved by mixing two partially miscible liquids in Chapter 2. If the fluids obtained are fully miscible, hypothetically, the interfacial tension if defined would be even lower. A natural question arises whether the axisymmetric configuration of one drop resting on top of another drop can be realized by the side-to-side coalescence which was not observed in Chapter 2. In this chapter, we examine the dynamic behavior of coalescence of miscible fluid drops on a solid surface, and analyze the final configurations formed after drop coalescence.

3.2 Background

Coalescence of sessile drops of identical fluids shows a rapid bridge healing process (Figure 3.1) and a slow contact line relaxation. In the rapid process, which is controlled by the interplay of inertia, viscosity and capillarity[96, 97], the drops touch and a bridge rapidly forms and heals while the contact line away from the bridge doesn't move appreciably[17, 22, 23, 98]. In the slow process, contact lines move and the drop relaxes to a circular shape over longer time scales, slowed by the dissipation at the moving contact lines and the fluid flow.[22, 23, 99]

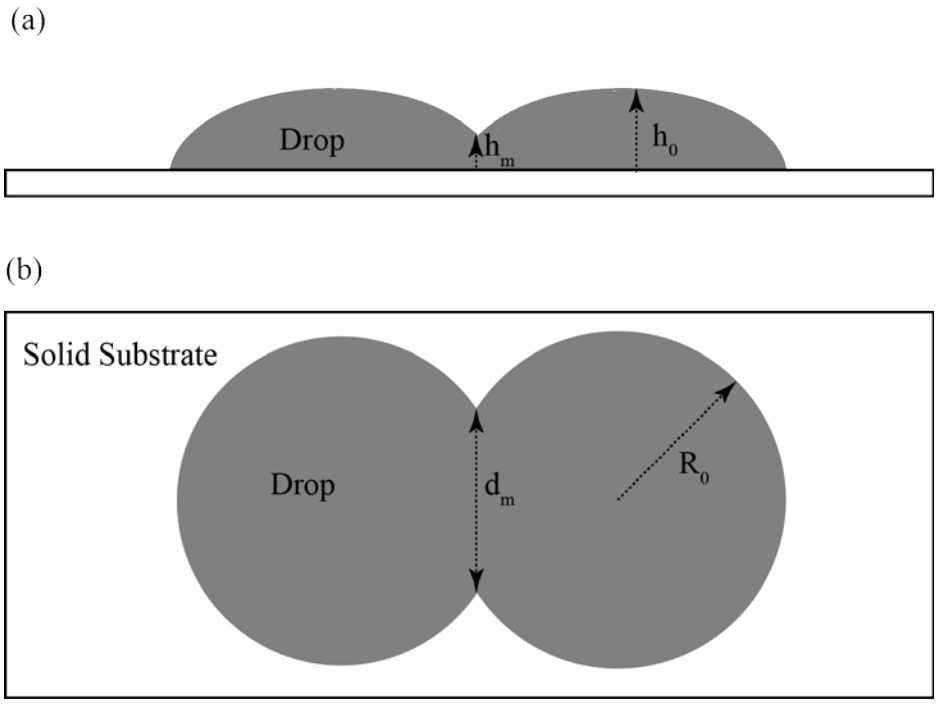

Figure 3.1.Schmatics of two thin drops of identical fluids coalescing on a solid substrate at the bridge healing process. (a) Side view. (b) Top view. d_m and h_m are the width and height of the bridge respectively, h_0 is the characteristic height of the drop while R_0 is the footprint radius of one drop.

Experimentally, the initial bridge healing of sessile drops has been probed using high speed video microscopy of fluids including mercury,[15] silicone oils,[96] water[100–103] and other organic fluids[98, 104–106]. Different mechanisms have been applied to cause the drops to touch and coalesce. Drops are allowed to spread spontaneously into one another,[96, 105] one drop is deposited using a syringe pump onto another,[15, 104, 106] or one drop is blown using pressurized air into another [103] on a surface until they contact and merge. In other cases, drops are forced to grow into one another due to an external supply of liquid[100, 101] or condensing vapor[22, 23, 98, 102]. In still other cases, drops are forced to collide due to wettability gradients on the surface,[107–109] where wettability gradients cause the merging drops to exhibit different contact angles just prior to coalescence even when the drops contain identical liquids.

Analyses of the initial bridge healing have included scaling arguments as well as numerical simulation based on a lubrication approximation.[101, 110] More detailed numerical simulations have used the volume-of-fluid method[111] and lattice Boltzmann method[104]. These studies demonstrate two main features of the initial stage of coalescence. First, the flow during bridge healing can be divided into two regimes: visco-capillary regime and inertio-capillary regime[14–16, 83, 98, 105, 112–116] depending on the relative importance of viscosity, inertia and capillarity. Second, the height and width of the bridge grow with power law behavior in time, where the power law exponents depend on whether viscous stresses or inertia are comparable to capillarity. Coalescence begins in a viscous regime where the surface tension force is balanced by the viscous force, the bridge width (see Figure 3.1) following a scaling relation $d_{m(viscous)} \sim \gamma\tau / \mu$, where γ is the surface tension and μ is the viscosity, τ is time after initial contact.[83, 115–117] In the other limit, where inertial forces balance surface tension, the bridge width follows a different power law $d_{m(inertia)} \sim (\gamma R_0 / \rho)^{1/4} \tau^{1/2}$, where ρ is the density of the fluid, R_0 is the radius of footprint of one drop as shown in Figure 3.1.[83, 115] The crossover time between these two regimes was estimated to be in the range of 1 ns to 2 μs for water drop coalescence with radius $R_0 = 2\text{mm}$ based on different characteristic lengths of coalescence.[115, 116] Even though high speed imaging experiments are able to capture the motion at a frame rate of $10^6\,\text{Hz}$[90, 118–120], limited spatial and temporal resolutions prevent the study of the initial viscous regime in detail.[115] Thus improved measurements of the bridge healing process for low viscosity fluids were performed using a method based on the conductivity of fluids with salt added, where viscosity can be independently varied over two decades by adding glycerol[115, 116]. The sets of drop coalescence experiments based on conductivity established the scaling rule of the crossover

time from viscous regime to inertial regime as $\tau_c \sim \mu^2 (R_0 / \rho\gamma^3)^{1/2}$.[115]

During the slow process following bridge healing, contact line relaxation plays a larger role and so the details of the surface chemistry and physical roughness significantly affect the process.[24, 121] Beysens and coworkers found that the relaxation of the composite drop to a spherical shape after bridge healing is usually five or six orders of magnitude slower than coalescence of drops in a bulk fluid because of the contact line motion.[17, 22, 23] This slow relaxation process is attributed to a very small Arrhenius factor resulting from a liquid-vapor phase change in the vicinity of the contact line. [22, 23]

Studies of coalescence of sessile drops have always examined drops of the same fluid until the recent work by Riegler and collaborators, who studied the coalescence of drops of miscible fluids of different surface tensions with very low vapor pressures.[28, 29, 31, 32] In this case, the coalescence is strongly delayed by Marangoni stresses.[30, 122] In contrast to the quick bridge healing process for the coalescence of identical fluid drops, for miscible drops with large surface tension differences (>3mN/m), the two drops after the initial contact remain well separated for a much longer period, connected by a neck region of very shallow bridge height. Through the shallow neck region, fluid flows from the low surface tension region to the high surface tension region due to Marangoni stresses. The Marangoni stresses counteract the capillary forces in healing the bridge between the two drops, thus inducing the delayed behavior of coalescence[28, 31]. The bridge finally heals and droplets merge to form a single drop after the fluid flow sufficiently reduces the surface tension gradient as the composition difference becomes negligible. The delayed coalescence behavior is also observed in the merging process of ethanol and water drops, where ethanol evaporation leads to self-propelling drops[123]. Delayed coalescence behaviors are unique to situations involving significant Marangoni stresses and do not occur when the shape

asymmetry (e.g., different contact angles upon initial contact) is due to different deposition times for the same fluid.[124]

In applications for drop coalescence in microfluidic devices, advective mixing during coalescence is used to control chemical reactions and physical dispersions.[8, 125–128] As suggested by Ottino and coworkers,[129, 130] the design of chaotic micromixers can enable effective mixing even at low Reynolds number. In the confined geometries of microfluidic devices, advective mixing after coalescence has been achieved using herringbone structures in the channels[131] as well as using electro-wetting[132] or electro-kinetic based mixing[133]. In contrast, the efficiency of mixing in open geometries such as sessile drops is not as well investigated. Experiments examining coalescence of sessile drops, supplemented by simulations, show little mixing without applying special wetting conditions or external forces.[134] A wettability gradient on the surface drives one drop toward another, inducing advective mixing.[107–109] Electro-wetting induced sessile drop oscillation using an external AC field can also enhance mixing.[135]

The dynamic mechanism of drop coalescence is of interest in both deepening the fundamental understanding for the roles of the gravitational force and the capillary forces for drops as well as the technological applications for better mixing devices in microfluidic devices. In this chapter, we investigate the side-to-side coalescence of two sessile drops containing fluids with different densities and viscosities, but nearly the same surface tension, contact angle and volume, which results in the drops having the same shape just before they coalesce. Adapting a laser induced fluorescence method first used to visualize a drop coalescing with a bulk fluid,[136] we track the mobile interface between the two merging drops as well as the composite drop/air interface during the coalescence process. With simultaneous side and top views, the contact line shape is also tracked. Similar to previous studies, a rapid bridge healing process is observed,

which we term Stage 1. This stage of the coalescence process is governed by minimization of the capillary energy for drops with either the same or different densities. During the slower contact line relaxation process, we see that there is internal fluid motion that occurs despite imperceptible changes in the shape of the external interface. The internal interface formed between the two initial liquid volumes demonstrates an advective motion for initial drops with density difference as small as 1%. This advective motion occurs over significantly longer timescales compared with the initial bridge healing, and we term this part of the process Stage 2. The advective motion observed in Stage 2 of the coalescence process is driven by a gravity current, similar to that observed in other two phases flows involving liquids of different densities [35–37, 137–141]. While the rapid bridge healing process has been studied in detail before, internal advective motion over longer timescales has not. The advective motion observed in Stage 2 of the coalescence process is the primary focus of this chapter. Using dimensional analysis as well as lubrication approximation, we identify the characteristic time scale and the dimensionless groups controlling the intermediate, gravity-driven fluid motion of Stage 2. We also note that there is a final stage of coalescence, Stage 3, in which diffusive motion leads to complete mixing of the fluid within the merged drop. For the systems we examine, the timescales for the three stages of coalescence are well separated. During Stages 1 and 3, there is little advective motion for the systems we examine, while the bulk of the advective fluid motion occurs during Stage 2.

3.3 Materials Preparation and Characterization

The solid substrates are fabricated from polydimethylsiloxane (PDMS) using a standard mixture ratio of 10:1 for the silicone elastomer base and the elastomer curing agent (Dow Sylgard 184). The PDMS is first mixed and defoamed using a centrifugal mixer (Thinky AR100)

before pouring the mixture into Petri dishes to cure and form a flat surface. Once poured, the mixture is degassed in the Petri dish for about 10 min and cured in a 60ºC oven overnight. The PDMS sample is removed from the Petri dish and the flat surface is used as the solid substrate surface for the coalescence experiment. Before experiments are performed, the solid PDMS substrate is rinsed with ethanol, acetone and distilled water. The measured advancing and receding water contact angles on the PDMS surfaces are θ_a = 105 ± 9 ° and θ_r = 62 ± 10 °, respectively. These contact angle values are in agreement with previously reported measurements on similar surfaces, and where a ridge (~1 μm) forms in the soft PDMS at the contact line.[142, 143] Even though Teflon surface has the flexibility of achieving various contact angles (up to 150º) with water simply by a sanding procedure using different grit sized sandpapers[144], the PDMS surface provides a waterproof connection with syringe needles to accurately control the size of drops needed in the experiments.

The fluids tested are composed of mixtures of purified water (Milli-Q, 18MΩcm, organic content < 10ppb) with varying concentrations of glycerol (Sigma-Aldrich ≥ 99.5%), allowing the adjustment of the mixture viscosity with minimal change in surface tension. Salt sodium chloride NaCl (Sigma-Aldrich ≥ 99.5%) and cesium chloride CsCl (Sigma-Aldrich ≥ 99%) are used to adjust the density of the glycerol/water mixtures with minimal viscosity and surface tension changes. In preparing the fluid samples, the salt is always added to the purified water and dissolved before the addition of glycerol to speed up the mixing. Fluorescein dye (0.05mM, Acros Organics) is used as a fluorescent marker in one of the fluid drops to be merged in the coalescence experiments. The solutions carrying the fluorescein are buffered to pH = 9.00 ± 0.02 (pHydrion Buffers, Micro Essentials) to maintain a high quantum yield of the dye[145, 146]. To ensure that the buffer salt does not alter the fluid properties with and without dye, all the aqueous

Table 3.1 Fluid properties of glycerol solutions

Sample	Mass Fraction (pH 9 Buffer % / Glycerol % / Salt %)	Density (g/ml)	Dynamic Viscosity (mPa s)	Surface Tension Without Dye (mN/m)	Surface Tension With Dye (mN/m)
A	21.4 / 78.6 / 0	1.200 ± 0.004	41.0 ± 0.2	66.2 ± 0.3	64.7 ± 0.8
B	45.5 / 54.5 / 0	1.145 ± 0.004	6.64 ± 0.06	66.3 ± 0.6	67.3 ± 0.3
C	70.9 / 29.1 / 0	1.071 ± 0.004	3.15 ± 0.11	66.9 ± 1.0	66.9 ± 0.8
D	50.0 / 50.0 / 0	1.124 ± 0.002	5.84 ± 0.07	66.4 ± 0.3	66.2 ± 0.4
G*	45.0 / 45.0 / 10.0	1.191 ± 0.002	7.61 ± 0.13	65.6 ± 0.3	
H	30.6 / 23.2 / 46.2	1.629 ± 0.004	4.87 ± 0.12	65.1 ± 1.0	
I	42.2 / 23.3 / 34.5	1.432 ± 0.005	3.95 ± 0.06	63.1 ± 1.0	
J	44.9 / 52.0 / 3.1	1.157 ± 0.004	7.13 ± 0.05	66.0 ± 0.8	
K	43.1 / 52.0 / 4.9	1.175 ± 0.003	7.52 ± 0.14	66.5 ± 0.5	

*Only G solution is formulated with NaCl. The four solutions H, I, J and K are formulated with CsCl. The A, B, C and D solutions do not contain salt.

fluids are prepared using the same pH 9 buffer solution. Even though pure glycerol is hygroscopic, the further absorption of water in the prepared solutions is observed to be slow. We store the solutions in capped beakers and periodically measure the densities, which do not change for weeks.

Table 3.2. Asymmetric properties of fluid drop pairs in coalescence experiments.

Fluid Pair	$\Delta\rho$ (g/ml)	$\lambda=\mu_t/\mu_b$	Bond Number
BJ	0.012	0.93	2.6 — 3.5
BK	0.030	0.88	2.3 — 2.6
BA	0.055	0.16	1.0 — 5.1
DG	0.067	0.76	0.9 — 5.9
CB	0.074	0.47	1.2 — 7.3
CG	0.12	0.42	1.7 — 4.5
AI	0.23	10	1.8 — 6.7
AH	0.43	8.4	1.2 — 6.5

The density, viscosity and surface tension of each solution used is listed in Table 3.1. Densities are determined by measuring the mass using a scale (Denver Instrumental Company Balance, Model XE-100A, accuracy 10^{-4} g) of a known volume contained in a volumetric flask (Pyrex No. 5640, 25 ± 0.03 ml). The viscosities of the solutions are determined using a Cannon-Fenske viscometer (Model K655-450) following the standard procedure.[147]

Surface tension is measured using a Wilhelmy pin connected to a balance on a MicroTroughX Langmuir trough.[148] The Pt pin is washed following a standard cleaning protocol and burned with a Bunsen burner to remove residual organics, after which the Pt pin is placed back on the Langmuir trough balance and the balance is zeroed in the air environment. The

apparatus is calibrated using the known PDMS surface tension (19.8mN/m) to obtain the calibration constant, and again checked for consistency by measuring the surface tension of distilled water. The uncertainties in the surface tension values reported in Table 3.1 arise from statistical fluctuation in the measurement of both the fluid surface tension and the calibration factor.

To probe the influence of asymmetric properties on the coalescence behavior, we select fluid pairs with various density differences as well as different viscosities. The fluid pairs used in the experiments are listed in Table 3.2. The characteristic parameters are: density difference $\Delta\rho = |\rho_b - \rho_t|$ and viscosity ratio $\lambda = \mu_t / \mu_b$ where the subscript *t* denotes the fluid property of the smaller density fluid and the subscript *b* denotes the fluid property of the larger density fluid. The Bond number, $Bo = \rho_t g L^2 / \gamma$, describing the relative importance of gravity versus surface tension, is also listed in Table 3.2, the range of values corresponding to those observed for the composite drop after coalescence. Here the characteristic length *L* is the length of the composite drop. (This is slightly different from Chapter 2, where we used $L = V^{1/3}$ for the ease of calculation.) The surface tensions of the two fluids are similar. To be consistent, we use the surface tension of the lighter fluid to calculate the Bond number. As seen in Table 3.2, density differences range from 1% to almost 40%, and the viscosity ratio varies from 0.2 to 10 such that the larger density fluid can be either more or less viscous than the smaller density fluid. Bond numbers range from 1 to 10, suggesting that gravity will flatten the external interface of the composite drop.

3.3 Experimental Methods

The fluid feed system is shown schematically in Figure 3.2a. Flat-tipped syringe needles

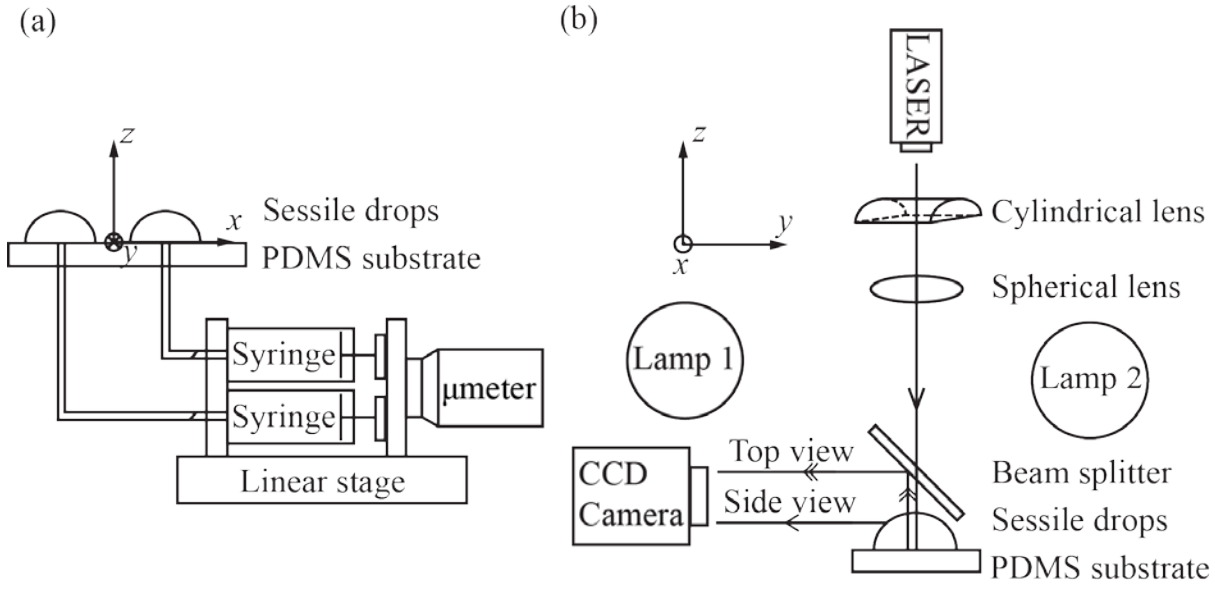

Figure 3.2.Experimental setup. (a) Schematic diagram of droplet feed system. (b) Schematic diagram of optical train.

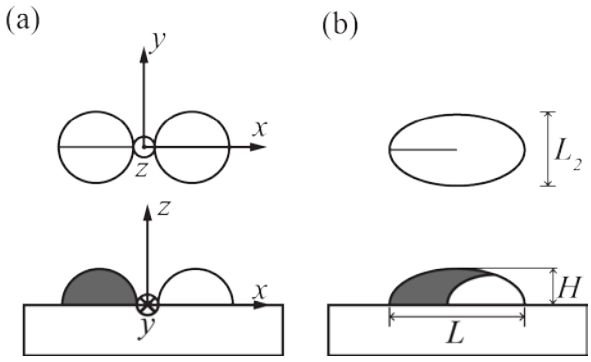

Figure 3.3. Definition of coordinates. (a) Schematic view of two sessile drops prior to coalescence. (b) Schematic view of composite merged drop after coalescence. The height *H* and length *L* of the composite drop is used to scale the system variables relevant to fluid flow.

(B-D PrecisionGlide needle, gauge 20G1½) are pushed through the PDMS substrate, with the spacing between two feed points controlling the sizes of the initial drops just prior to coalescence. Fluid drops are pumped from underneath the substrate into the syringe needles which are connected with two syringes (BD 1ml syringe, Luer-Lok Tip) by Polyvinyl chloride tubes

(Fisherbrand, manifold pump tubing, inner diameter 0.89mm). The syringes are attached to the same micrometer stage, ensuring that the two initial drops are of nearly equal volume as they touch and merge. The rate of drop formation is controlled manually by the micrometer at approximately 5 – 20 μL/min, producing contact line speeds of approximately 0.02 – 0.05 mm/s. These contact line speeds are maintained until just before the drops touch, and then the final contact of drops is achieved by natural relaxation of the contact lines after pumping has ceased.

The optical train is shown in Figure 3.2b. All images are captured using a CCD camera (Q-See, Anaheim CA, model no. QPSCDNV, 30 fps mounted with a 55mm telecentric lens from Edmund Optics). The resolution of the camera is calibrated to be 0.045mm per pixel. The coalescing drops are illuminated by two lighting systems. Using two incandescent lamps, the drops are illuminated from the front and the back. A blue laser (405 ± 10 nm, 5mW) focused through convex cylindrical and spherical lenses forms a laser light sheet inside the drops. Images of the light sheet locate the fluid containing the fluorescent dye. This light sheet can be translated in the *y* direction to illuminate different cross sections of the drop. Using a beam splitter placed above the drop, the drop is simultaneously imaged from the side and from above.

As shown in Figure 3.3, the side view allows measurement of the shape of the drop as well as the location of the dyed fluid within the cross section illuminated by the laser light sheet. The top view allows monitoring of the lateral location of the light sheet as well as measurement of the contact line location and the location of the point where the dyed and undyed fluids meet along the top external interface of the drop.

3.4 Experimental Results

Observations of coalescence of the fluid drop pairs listed in Table 3.2 are captured using the

optical setup and video capture system described in the previous section. The resulting image sequences (Figure 3.4) demonstrate that there are three primary stages of coalescence, with each stage governed by different forces and phenomena. In Figure 3.4, frames a.1 through a.5 show coalescence of two drops with the same density. One of the initial drops contains fluorescent dye. In Figure 3.4, frames b.1 through b.5 show coalescence of two drops with a density difference of 0.074g/ml. The lighter fluid contains fluorescent dye. In both sequences, the first frame shown is just prior to contact between the drops. The second frame shown corresponds to t = 0.03s after the drops touch. By this time, the rapid bridge healing process is nearly complete in all experiments. In some experiments, we observe capillary waves resulting from the rapid bridge healing process. Frames a.3 and b.3 capture the end of the Stage 1 bridge healing process, after which any capillary waves observed have decayed and the exterior shape of the merged drop no longer changes. The internal interface between the two merged fluids at the end of Stage 1 is sharp and nearly vertical. The density differences do not change the bridge healing process during Stage 1. Based on the fluorescence imaging, we see no evidence of twisting of streamlines and therefore conclude that no advective mixing of the two initial fluids has occurred. Following the end of Stage 1, frames a.3 through a.5 show that there is no internal flow within the merged drops of fluid pair BB within the first 3 s after the drops contact one another. Frames b.3 through b.5 show that the internal interface between fluid pair CB evolves over the first 3 s after contact until the interface is nearly horizontal, with the lighter, fluorescently dyed fluid stratified in the top layer. These two experiments taken together suggest that two fluids of different densities stratify due to a gravity current during stage 2 of the coalescence process. In Stage 2, the gravity driven flow proceeds in timescales of the order of seconds until full stratification occurs, as shown in frame b.5. At this late time in Stage 1, the interface between the two initial

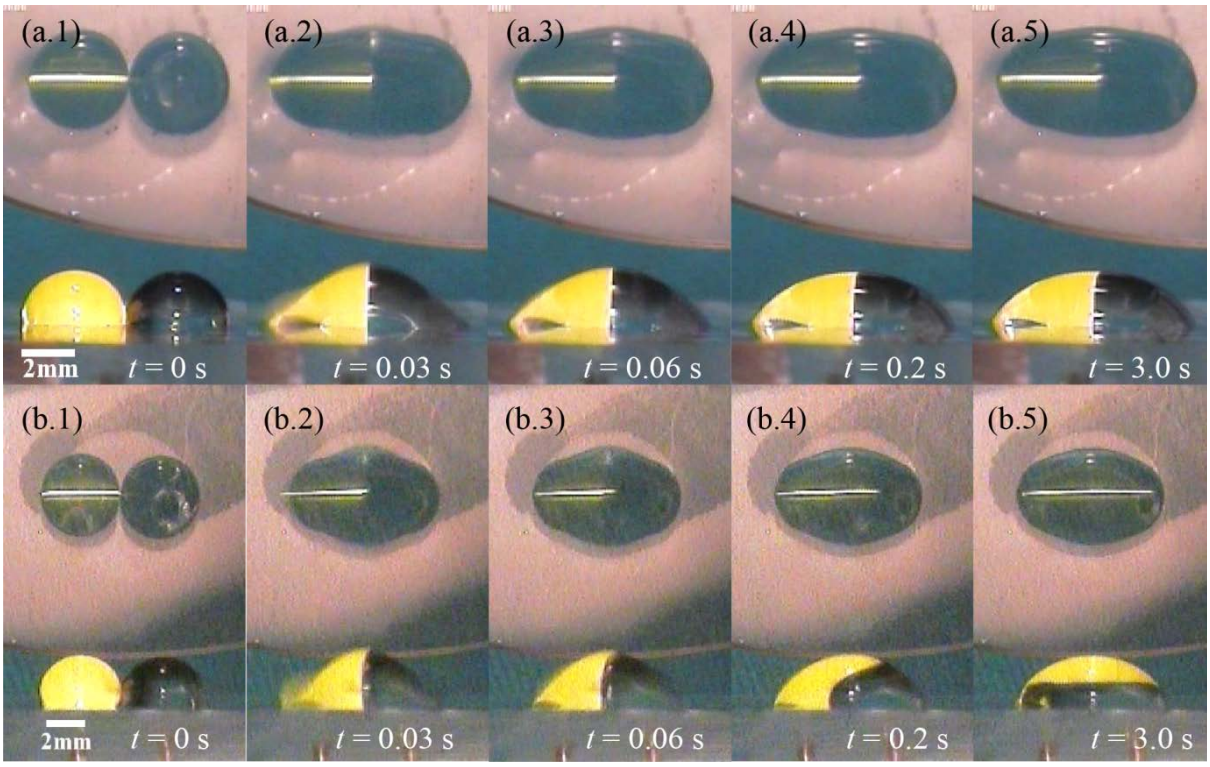

Figure 3.4. Time sequence of images of the coalescence process for two experiments with different fluid pairs. (a) Fluid pair BB for initial drop volumes of 20.2 µL. Both the fluorescent dyed fluid and the undyed fluid have a density of 1.145 g/ml (b) Fluid pair CB for initial drop volumes of 22.7 µL. The fluorescent dyed fluid has a density of 1.071 g/ml while the undyed fluid has a greater density of 1.145 g/ml.

fluid volumes is still sharp. As we will discuss later, at longer times, of the order of several minutes, Stage 3 of the coalescence process occurs, in which diffusion blurs the interface and the two fluids mix. Throughout both Stages 2 and 3 of coalescence, the relatively minor motion of the contact lines, due to residual contact angle hysteresis, inhibits the composite drop from attaining the circular contact line footprint that surface tension alone would produce.

3.4.1 Stage 1 – Bridge healing

For drop coalescence, the flow during bridge healing can be divided into two regimes: a

visco-capillary and an inertio-capillary regime[14, 15, 98, 105]. A simple estimate for visco-capillary timescale can be obtained combining the dimensional parameters, where $\tau_v \sim \mu^3 / \rho\gamma^2$ is 70 ns for a typical composite drop (μ ~ 7 mPa s, ρ ~ 1.2 g/ml, γ ~ 70 mN/m) and ranges from 10 ns to 12 μs for all the experiments we performed. The inertio-capillary timescale is estimated balancing capillarity and inertia, where $\tau_i = \sqrt{\rho R_0^3 / \gamma}$ is approximately 50 ms for a typical composite drop (ρ ~ 1.2 g/ml, R_0 ~ 5 mm, γ ~ 70 mN/m) and ranges from 10 ms to 250 ms for the fluid pairs we considered. In contrast to previous experiments on coalescence of drops with identical densities,[98] the fluids we examine are 20 times less viscous, resulting in a visco-capillary time 8000 times shorter than the previous experiments. Thus the initial bridge-healing regime is dominated by capillarity and viscosity up to about 70 ns, which is significantly shorter than the camera frame rate and thus is not captured in our experiments. Beyond about 70 ns, the flow enters the inertio-capillary regime for timescales up to about 50 ms for drops a few millimeters in radius. Consistent with this estimate of the characteristic timescale, for most of our experimental conditions, the bridge between the coalescing drops heals and any capillary waves that appear on the drop surface decay within the first two video frames ($\approx$ 60 ms). As pointed out in a recent experiment by Eddi[112], capillary waves are observed for low viscosity drops which implies that the observations take place in the inertio-capillary regime. For very large drops and for the case with the largest density difference, observation of the side view of the merged droplet shows that drop shape oscillation can persist as long as 0.5 s.

During Stage 1, the contact line at the bridge moves outward from the contact point while the contact lines along the long axis of the drop move slightly inward. At this time, the interface

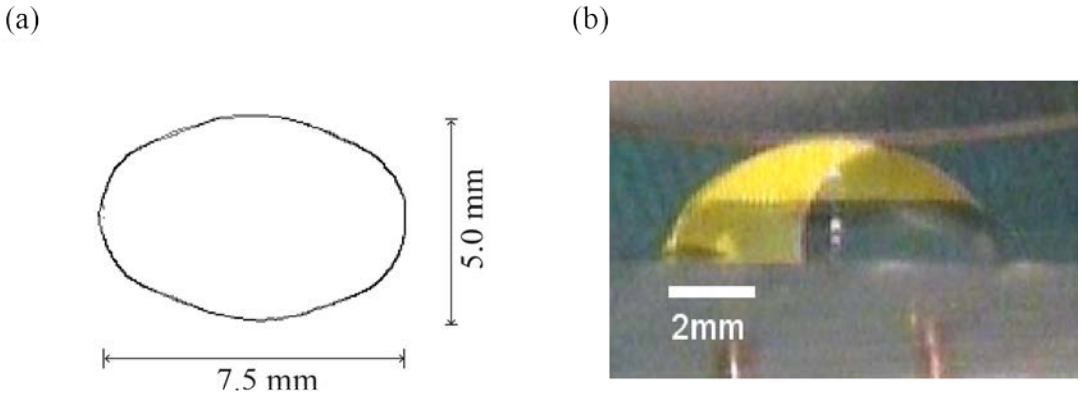

Figure 3.5. a) Overlay of edge profiles from top view images showing the position of the contact lines at two different times: just after the end of Stage 1 (t = 0.13 s) and toward the end of Stage 2 (t = 3 s) for fluid pair CB at a volume of 22.7 µL. The difference in contact line locations for these selected times is small and obscured by image resolution. b) Overlay of two side view images at 0.13 s and 3 s.

between the fluids is sharp and tilts at most about 2º away from vertical (frame 3b.3). The conditions at the end of Stage 1 set the initial condition for the gravity driven flow that occurs during Stage 2 of the coalescence process.

3.4.2 Stage 2 – Gravity current

In Stage 2 of the coalescence process, the lighter fluid layer flows over the top of the denser fluid layer, even for fluid pairs AI and AH where the surface tension differences between these two fluids would have led to an initial Marangoni force opposing the gravity-driven flow, and for fluid pair BJ where the density difference is only 1%. Experimentally, for all but the fluid pairs with the largest density differences, the shape of the external interface of the composite drop does not change appreciably after the end of Stage 1 (see frame 3b.3 and later frames).

Figure 3.5a overlays edge profiles extracted from top view images near the beginning and

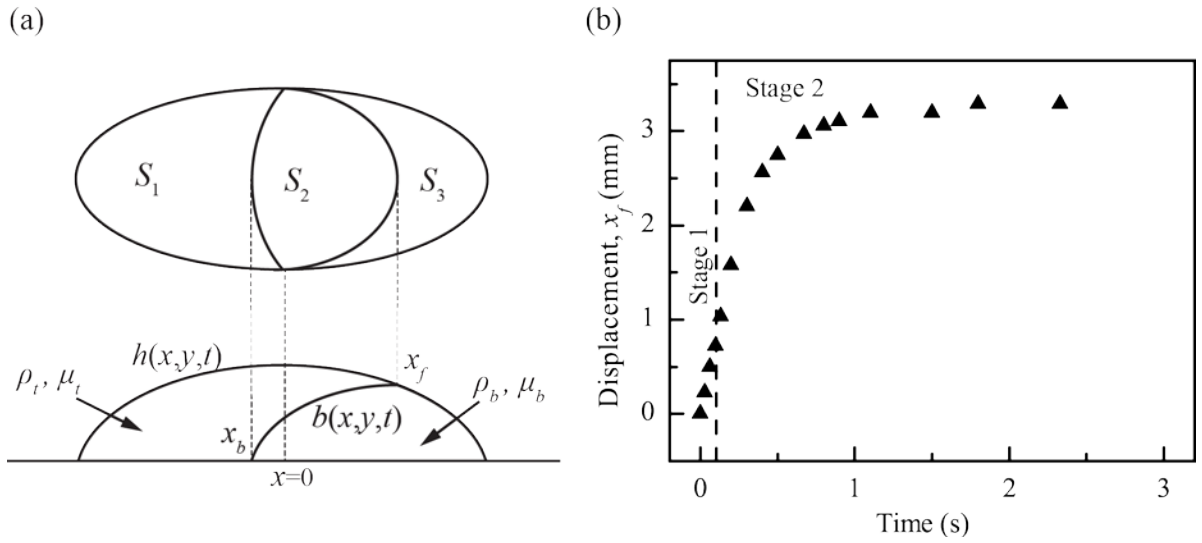

Figure 3.6 (a) Schematic diagram of the internal interface within the composite drop. The position $x = 0$ is where the vertical internal interface located at the end of Stage 1, x_b is the internal interface point in contact with the solid surface at time t, x_f is the external interface point where the two fluids meet at the top of the drop at time t. (b) Measured x_f as a function of time. The vertical line indicated on the plot at right corresponds to $t = 0.1$ s and represents the beginning of the gravity-driven flow of Stage 2 of the coalescence process. (Fluid pair CB; volume 22.7 μL) For clarity, the error bars are not shown in figures since the uncertainties for values of x_f at different times are identically 0.045mm due to the camera resolution, which falls within the symbols if drawn.

end of Stage 2. The nearly complete overlap of these edge profiles shows that the contact lines are pinned throughout Stage 2, exhibiting only very minor local adjustments of the order of 0.05 mm to 0.15 mm for the duration of this stage of the process. Figure 3.5b overlays side view images for the same experiment and the same times, showing that the internal interface has moved as stratification progresses, and demonstrating that any changes in the external drop shape are visually undetectable throughout Stage 2. Changes in the composite drop shape are visually discernable in the extreme cases of the fluid pairs with the largest density difference (20 – 40%) and for the largest drops.

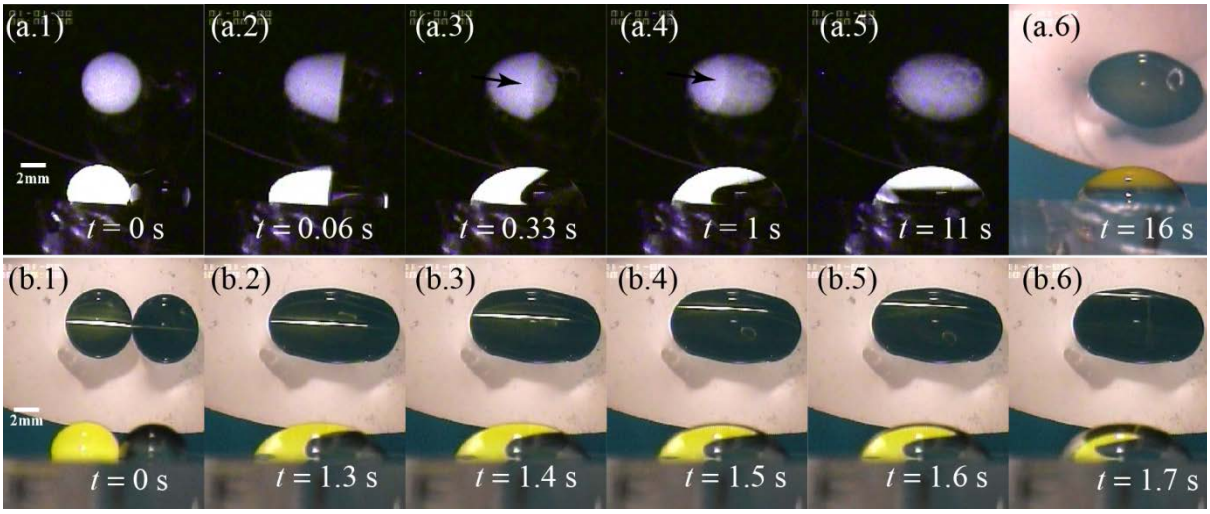

Figure 3.7 Image sequence depicting the internal fluid flow leading to stratification within the composite drop. Images show fluid pair BJ with volume 24.2 µL and 25.8 µL respectively. (a) The entire composite drop illuminated by a large laser spot located above the drop. (b) The composite drop illuminated from above by the laser light sheet, translated in the *y* direction. The image sequence depicts the location of the internal dyed (lighter) fluid at different cross-sections in the third dimension of the drop, captured at timesteps significantly smaller than the flow timescales.

The motion of the gravity current can be quantified by tracking the interface point where the dyed and undyed fluids meet at the top external interface, denoted x_f in Figure 3.6a. The position of this interface point is not distorted by refraction through the air/liquid interface of the drop when viewed from the top or the side. Figure 3.6b shows the horizontal coordinate of the interface point as it moves during the gravity driven flow. The velocity of the horizontal gravity current at the beginning of Stage 2 interpolated from Figure 3.6b is 0.002 m/s. Thus the Reynolds number $Re = 1$ for the gravity current at early times in Stage 2. At later times in Stage 2, the horizontal coordinate approaches a constant value, indicating that the velocity of the interface gradually decreases with time and vanishes when full stratification has occurred. During this later part of Stage 2, the Reynolds number becomes very small; therefore, gravity and viscous

forces balance.

Although refraction of the internally emitted fluorescent light as it leaves the drop may distort the perceived internal interface shape, we obtain a qualitative impression of the full three dimensional fluid movement during Stage 2 by varying the lighting conditions. In Figure 3.7a, frames a.1 through a.5 show the coalescence of drops when the spherical convex lens in Figure 3.2b is replaced with a concave lens, leading to a large laser light spot exciting fluorescein throughout the entire drop. In frame a.6, the drop contact line is shown by illuminating the back light Lamp 1. The stratification is complete after 11 s, and a comparison of the upper images in frame a.5, showing the extent of dyed, lighter fluid, and frame a.6, showing the extent of the undyed, heavier fluid, demonstrates that the lighter fluid forms a layer occupying the top portion of the composite drop after stratification. It is evident that the dyed fluid flows in the *y* direction during the stratification process and that coalescence requires three-dimensional flow. Under the modified lighting conditions, in frames a.1 to a.5, the observed intensity represents an integration of the light passing through the entire drop from the side and top. The bright line in the top view image, indicated by the arrows shown in frames a.3 and a.4, aligns with the position of the bottom contact line of the internal interface. This suggests that the heavier fluid has flowed under the lighter fluid but has not proceeded further to the left than the contact line in any cross section of the composite drop.

Figure 3.7b shows an image sequence of the coalescence process illuminated by the laser light sheet. In these images, the laser light sheet is scanned rapidly in the *y* direction, illuminating different three-dimensional cross sections of the drop during the internal flow of Stage 2. The scanning occurs at ≈ 8 mm/s, a speed that is much faster than the speed of the fluid motion. Thus, the frames shown represent cross-sectional views of the fluid motion at essentially the

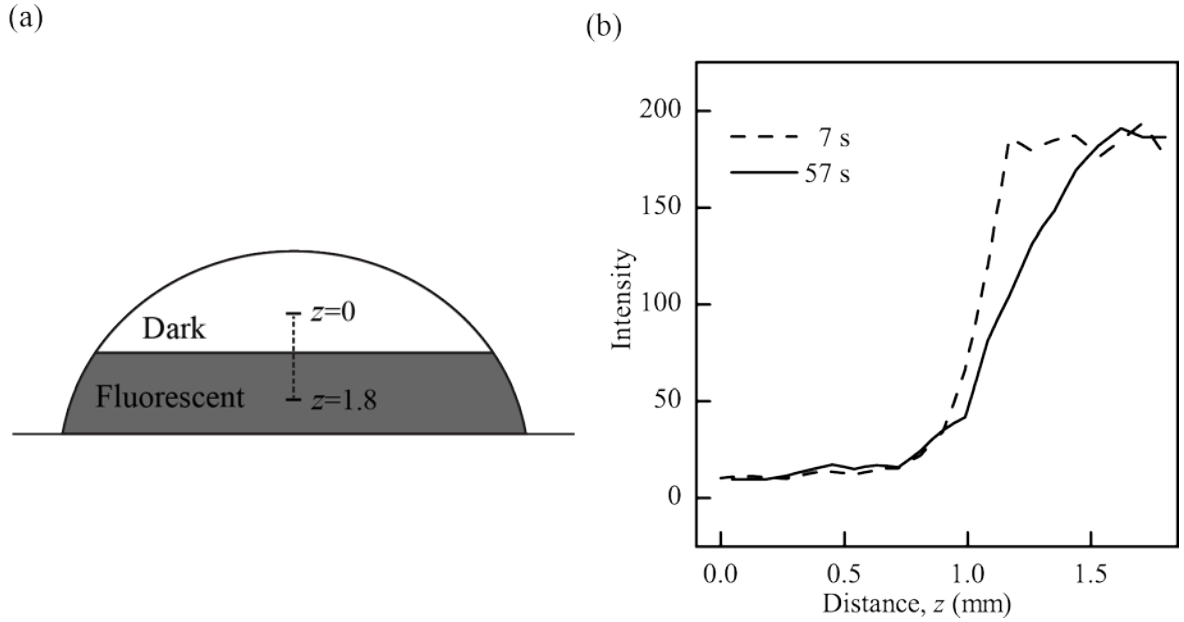

Figure 3.8. a) Schematic diagram depicting the location of the line scan used to estimate the broadening of the interface. b) Line scans of intensity across the internal interface for fluid pair CB with volume 8 μL, taken at t = 7 s and 57 s after the onset of coalescence.

same time point in the evolution of the stratification. The image sequences shown in Figure 3.7a (frames a.3 and a.4) and Figure 3.7b taken together show that fluid in the central cross section moves at a faster velocity than the fluid occupying the cross sections closer to the drop edge.

3.4.3 Stage 3 – Diffusive mixing

After the internal contents of the composite drop have become fully stratified at the end of Stage 2, diffusion drives the final mixing of the initial fluid volumes. Figure 3.8 demonstrates the diffusive mixing of the fluids. The interface between the two fluids becomes visually blurred some time after stratification is complete. Line scans of intensity taken along a line perpendicular to the interface show that the composition gradient broadens diffusively. In a typical case, the width of the interface broadens about 450 μm over 50 s, where the width is defined as the

distance between the locations along the line scan where the intensity is 10% and 90% of the maximum intensity. Using this broadening width and timescale, we estimate a diffusion coefficient of $D \approx 4\times10^{-6}\text{cm}^2/\text{s}$ using the relationship $D = l_{broaden}^2 / 2t_D$, where $l_{broadening}$ is the broadened width and t_D is the time over which broadening occurs. Using this value of diffusion coefficient along with the measured velocity *u* during the initial stages of motion of the gravity current, and the drop size *L* as the characteristic length scale, results in an estimated Peclet number (Peclet number compares advective motion with diffusion) during Stage 2 of $Pe=Lu/D \approx$ 2500. The large value of Peclet number suggests that diffusion has negligible impact on the flow during Stage 2 before stratification is complete, consistent with our observations.

3.5 Scaling analysis and comparison with experimental results

The experimental observations described above strongly suggest that fluid motion within the composite drop during Stage 2 proceeds via a gravity current, promoting stratification of the initial fluid volumes into two layers. To verify the hypothesis that the fluid motion is a gravity current, we first conduct dimensional analysis to determine the scaling of the internal interface velocity with fluid properties and flow conditions. We assume that the hydrostatic pressure variation driving flow within the composite drop scales as $\Delta\rho gH$, and that the viscous stress resisting motion scales as $\mu_b L / TH$ where *T* is the characteristic time (use of the viscosity of the heavier fluid is suggested by Huppert[35]). Equating the driving pressure gradient and the viscous stress, we obtain a characteristic time $T \approx \mu_b L / \Delta\rho gH^2$. Noting that inertia has decayed by the end of Stage 1 and therefore the Reynolds number is small during Stage 2, and also noting that the composite drops always exhibit aspect ratios *H*/*L* less than unity, we anticipate a time scaling typical of those used in lubrication analyses of thin film geometries. Thus, we modify the

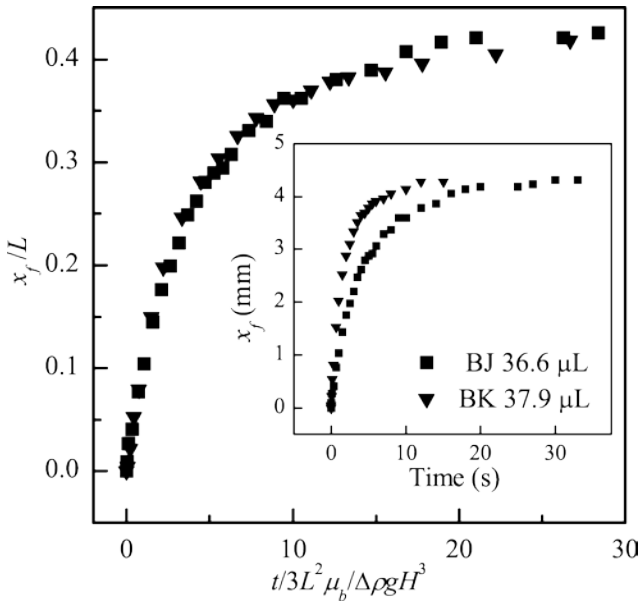

Figure 3.9. Displacement of the internal fluid interface as a function of time for varying density differences and similar composite drop size and viscosity. The inset shows unscaled displacement versus time for fluid pairs BJ and BK. The main figure shows the displacement versus time scaled with the characteristic timescale given in Equation (3.1).

characteristic timescale by a factor of the aspect ratio, such that

$$T_c \approx \mu_b L^2 / \Delta\rho g H^3 . \tag{3.1}$$

To verify the timescale indicated by dimensional analysis, we examine experimental data from various fluid pairs, isolating changes in density difference, drop geometry, and viscosities. Figure 3.9 compares the displacement of the top point on the internal interface, x_f, for two fluid pairs with similar viscosities and sizes, but different density differences $\Delta\rho$. Figure 3.9 inset shows the unscaled displacement as a function of time. The larger density difference drives faster displacement of the interface, leading to a more rapid approach to the final stratified interface position. Figure 3.9 shows the displacement of the internal interface, scaled by the length of the composite drop, as a function of the time scaled by the characteristic time T_c given in Equation

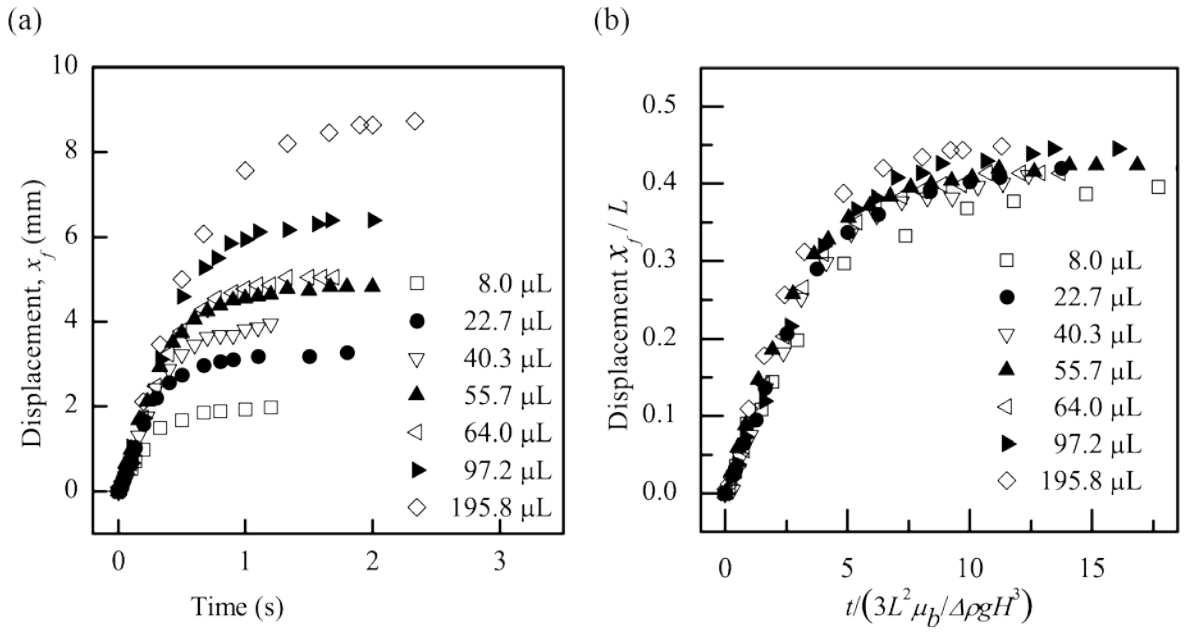

Figure 3.10. a) Displacement versus time for varying drop volumes of fluid pair BC, with density difference and viscosity held fixed. b) Displacement normalized by the length of the composite drop versus time normalized by the characteristic time given in Equation (3.1).

(3.1). On normalized axes, the experimental curves collapse, suggesting that the data scales with density difference in a manner consistent with that expected for a gravity current.

Figure 3.10 compares several displacement curves for a single fluid pair, varying the initial drop volumes and therefore varying the composite drop dimensions *H* and *L*. Figure 3.10a shows the displacement of the top point x_f on the internal interface as a function of time for different drop volumes. While the approach to the final displacement occurs at approximately the same initial rate for all of the cases shown, the final displacement is larger and the time at which final displacement is reached is later for larger volumes. The final displacement of the internal interface depends on drop volume because the less dense fluid occupies a different layer thickness within the composite drop at the end of stratification. The final position of the interface depends on the three-dimensional composite drop shape, and thus the Bond number, as well as

the drop volume. These factors render it difficult to determine a well-defined analytical expression for the final interface displacement. Figure 3.10b shows the normalized interface displacement scaled by the composite drop length L, as a function of time normalized by the characteristic timescale given in Equation (3.1). The dimensionless curves of Figure 3.10b collapse to nearly a single curve with some spread in the shoulder region, indicating that the geometric dependence of the timescale given above works well, including the extra factor of the aspect ratio H/L. However the value in the plateau region varies monotonically with drop volume or Bond number. The normalization with L accounts for the major effect of drop volume but does not account for the flattening of the drop with increasing Bond number. This residual effect of Bond number causes the observed spread in plateau values.

Figure 3.11 considers a wide variety of fluid pairs with varying density difference and fluid viscosities, keeping volume and thus the Bond number nearly fixed. Figure 3.11a shows that the displacement of the top point on the internal interface, x_f, approaches a similar final value, as a result of the similar composite drop volumes. However, the rates of approach to the final displacement values vary considerably for the eight fluid pairs considered. While the data sets are not clearly ranked in terms of any individual fluid property, it is notable that the data set corresponding to the slowest approach to equilibrium corresponds to fluid pair BJ, which has the smallest density difference of the group. The data set with the fastest approach to equilibrium corresponds to fluid pair AH, which has the largest density difference. These observations are consistent with expectations for the gravity current scaling given by Equation (3.1). For the data sets exhibiting intermediate timescales, it is clear that both fluid viscosities also play a role in the rate of approach to equilibrium.

Figure 3.11b shows the result of normalizing the displacement with the maximum

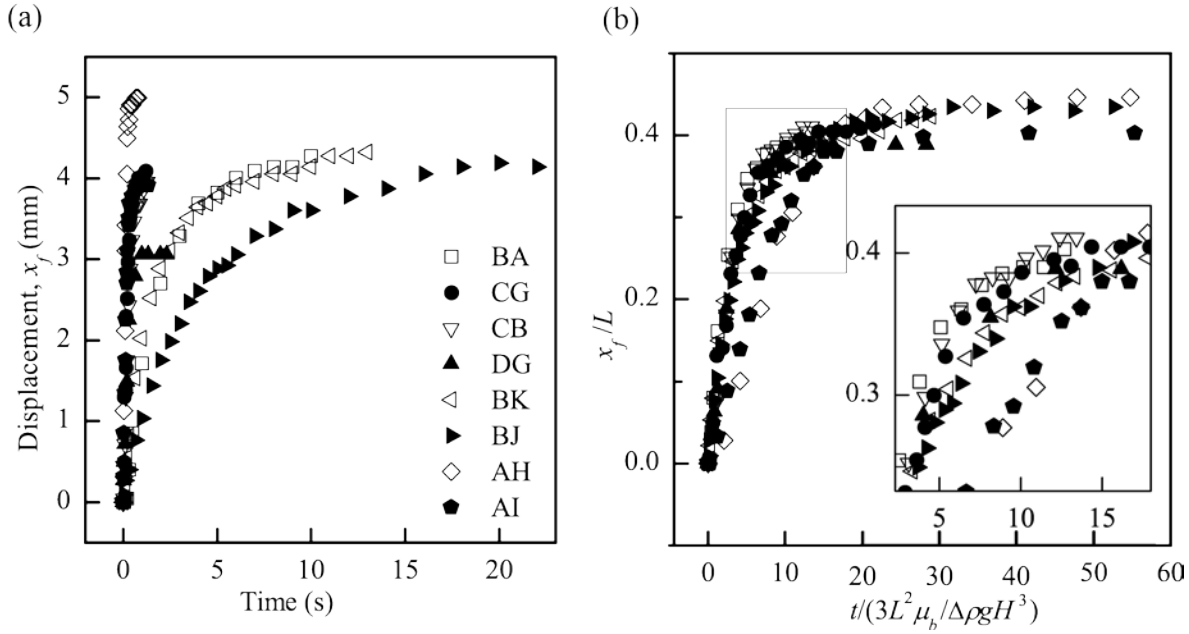

Figure 3.11. a) Displacement versus time for several fluid pairs with different viscosities and density differences, keeping drop volume nearly constant. b) Displacement normalized by the maximum extent of the internal interface versus time normalized by the characteristic time given in Equation (3.1). Inset shows an expanded view of the transition region from a rapid gravity current to fully stratified layers.

displacement of the stratified interface, plotted as a function of time normalized by the characteristic timescale given by Equation (3.1). The data sets collapse considerably to occupy nearly a single curve, indicating that the motion of the internal interface is well described by the expected scaling for a simple gravity current. However, the collapse of the data is not as good as in Figure 3.9 and Figure 3.10, which considered only density difference and composite drop geometry. Specifically, examining the transition region from a rapidly advancing gravity current to complete stratification of the two layers, we see that the data sets deviate monotonically with viscosity ratio. The leftmost data set showing the fastest approach to equilibrium corresponds to fluid pair AB with viscosity ratio $\lambda = \mu_t / \mu_b = 0.16$, while the rightmost data set showing the slowest approach to equilibrium corresponds to fluid pair AH with viscosity ratio $\lambda = 10$. The

monotonic variation with viscosity ratio is notable, since the viscosity of the heavier fluid in most of the fluid pairs considered is similar, falling between $\mu_b \approx 4:8$ mPa s for all cases except fluid pair BA, in which $\mu_b = 41$ mPa s. Unlike in previous analyses of gravity currents, in which the characteristic timescale depends only on the heavier fluid viscosity[35]; it appears that the stratification of two fluid layers in a merging sessile drop is also influenced by the viscosity of the lighter fluid layer, which can also play a role in retarding the flow.

For the experiments of density difference being as low as 1%, the drops after coalescence all form a stratified configuration after the gravity driven period, which resembles the behavior of stable axisymmetric configuration as described in Chapter 2. In Chapter 2, we never observe the formation of axisymmetric compound sessile drop after side-to-side coalescence for the low interfacial tension system, probably due to the fact that Janus configuration is of lower energy than the axisymmetric configuration. Now in this smallest density difference case where $\rho_t / \rho_{b(\exp)} = 0.99$, the stable axisymmetric configuration requires the experimental density ratio to be smaller than the critical density ratio $\rho_t / \rho_{b(\exp)} \le \rho_t / \rho_{\text{bcritical}}$. Based on Equation (2.18) and $\rho_t / \rho_{\text{b critical}} \ge 0.99$, the upper bound of the interfacial tension is obtained, $\gamma_{\text{transient}} / \gamma_b \le 0.012$; therefore the transient surface tension is $\gamma_{\text{transient}} \le 0.8$ mN/m. This side-to-side coalescence technique allows the estimation for the upper bound value of transient interfacial tensions, which cannot be measured using typical interfacial tensiometers[149, 150], due to the transient interface between miscible fluids.

3.6 Lubrication Approximation Based Modeling

Motivated in part by the lack of complete collapse of the displacement curves with the

scaling corresponding to a simple gravity current shown in Figure 3.11b, we seek a more detailed description of the internal fluid flow within the composite sessile drop during Stage 2 using the lubrication approximation to simplify the governing equations. The lubrication approximation has been previously applied to model similar phenomena including the internal interface motion for two layer systems[151, 152] and gravity driven flow models. For gravity currents, the lubrication has been applied to flows on a solid surface[37], at the bottom in a tank[35, 153], on top of another fluid phase[36] or in a closed long tube geometry[137–141]. The two main assumptions of the lubrication approximation are: 1) the reduced Reynolds number is small, $Re(H/L) = 1$, and 2) the square of geometric aspect ratio is small, $(H/L)^2 << 1$.[154] In our experiments, the aspect ratio of the composite drop H/L ranges from 0.2 to 0.4. The Reynolds number is maximum at the beginning of Stage 2 and ranges from 0.1 to 1.5 for different experimental fluids considered here. Thus the two conditions are satisfied: 1) the reduced Reynolds number varies from $0.03 < Re(H/L) < 0.6$ and 2) the square of the aspect ratio in the range $0.04 < (H/L)^2 < 0.16$. Experimentally, we observe that the external and internal interfaces meet the solid substrate at a high angle, potentially violating the lubrication approximation. To mitigate the complication of wedge flow when the internal interface approaches the corner region of the solid contact line, we examine the interface evolution only at early times, when the internal interface is far away from the corner and the impact of the wedge flow is negligible. Even though the internal interface itself meets the solid substrate at a high angle, the lubrication approximation is still expected to yield good qualitative results for gravity driven flows. In cases similar to ours[37, 155–157], it has been shown that a violation of the lubrication approximation near the contact line does not contaminate the interface shape and propagation speed of the overall gravity current. In Section 3.7, we will use the numerical results to explicitly assess the validity of the lubrication

approximation at the internal interface in our case.

Based on experimental observations, we fix the contact line position and assume that the shape of the external interface of the composite drop does not vary with time. Because the fluids are miscible aqueous solutions and the measured air/liquid surface tensions are very similar, we assume the interfacial tension of the internal interface is zero. If the concept of interfacial tension is extended to fully miscible fluids, based on the observation of persistent shape of interface for some time, transient surface or interfacial tension can be defined.[158–160] Fully miscible fluids are determined to have very low transient interfacial tension, for example, the upper bound value of interfacial tension between glycerol and water is estimated to be 0.5 mN/m[160, 161] and our estimation at the end of section 3.5 shows the interfacial tension has an upper bound of 0.8 mN/m. This assumption of almost zero interfacial tension is reasonable compared with surface tension about 70mN/m. We seek a differential equation describing the time evolution of the internal interface profile.

Since inertial effects are negligible after Stage 1 compared with the gravity current, we formulate the lubrication analysis of the internal flow during Stage 2 by first writing the Stokes and continuity equations for both the upper and lower fluids,

$$-\frac{\partial p_t}{\partial x}+\mu_t\frac{\partial^2 u_t}{\partial z^2}=0, \tag{3.2a}$$

$$-\frac{\partial p_t}{\partial y}+\mu_t\frac{\partial^2 v_t}{\partial z^2}=0, \tag{3.2b}$$

$$-\frac{\partial p_t}{\partial z}+\rho_t g=0, \tag{3.2c}$$

$$\frac{\partial u_t}{\partial x}+\frac{\partial v_t}{\partial y}+\frac{\partial w_t}{\partial z}=0, \tag{3.2d}$$

$$-\frac{\partial p_b}{\partial x}+\mu_b\frac{\partial^2 u_b}{\partial z^2}=0\,, \tag{3.3a}$$

$$-\frac{\partial p_b}{\partial y}+\mu_b\frac{\partial^2 v_b}{\partial z^2}=0\,, \tag{3.3b}$$

$$-\frac{\partial p_b}{\partial z}+\rho_b g=0\,, \tag{3.3c}$$

$$\frac{\partial u_b}{\partial x}+\frac{\partial v_b}{\partial y}+\frac{\partial w_b}{\partial z}=0\,, \tag{3.3d}$$

where the subscript *t* denotes the upper, lighter fluid, and the subscript *b* denotes the bottom, heavier fluid. The pressure is denoted by *p*; *u*, *v* and *w* are the velocity components in the *x*, *y* and *z* directions respectively; μ is the viscosity; *g* is the gravitational acceleration constant and ρ is the fluid density. Equations (3.2) and (3.3) show that in the lubrication formulation, in both the upper and lower fluid layers, the pressure variation in the vertical direction is given solely by the hydrostatic pressure. Further, if Equations (3.2) and (3.3) are integrated assuming $\partial p_t/\partial x$, $\partial p_t/\partial y$, $\partial p_b/\partial x$ and $\partial p_b/\partial y$ do not vary across the thin film, the flow in the horizontal *x* and *y* directions exhibits a characteristic parabolic velocity profile[154].

As shown in Figure 3.6a, the internal interface profile is denoted by $b(x, y, t)$, and the external interface of the drop is described by $h(x, y, t)$. The boundary conditions for the two fluid layers are given by a shear free condition at the external air/liquid interface (Equation (3.4a)), velocity continuity (Equation (3.4b)) and tangential stress balance (Equation (3.4c)) at the internal interface, and no slip at the solid surface (Equation (3.4d)). Applying the no slip condition up to and including the contact line will result in a non-integrable stress singularity at the contact line[162, 163]. The Bond number for the internal interface is large in our system due to zero interfacial tension assumption, and therefore the details of contact line dynamics will not

impact the gravity driven spreading of an interface[25]. Thus we, like Tanner[164] and Huppert [37], do not need to specify the mechanism that alleviates the stress singularity.

$$\frac{\partial u_t}{\partial z} = 0, \frac{\partial v_t}{\partial z} = 0 \qquad \text{at } z = h, \tag{3.4a}$$

$$u_t = u_b, v_t = v_b, w_t = w_b \qquad \text{at } z = b, \tag{3.4b}$$

$$\mu_t \frac{\partial u_t}{\partial z} = \mu_b \frac{\partial u_b}{\partial z} \qquad \text{at } z = b, \tag{3.4c}$$

$$u_b = 0, v_b = 0 \qquad \text{at } z = 0, \tag{3.4d}$$

The normal stress boundary condition is given by $(p_t - p_{air}) - [\hat{\boldsymbol{n}} \cdot \boldsymbol{\tau}^{\boldsymbol{I}} \cdot \hat{\boldsymbol{n}}] = (\frac{1}{R_1} + \frac{1}{R_2})\gamma$ [165] for the external interface, where R_1 and R_2 are the principal radii of curvature of the external drop shape, $\hat{\boldsymbol{n}}$ is the normal direction and $\hat{\boldsymbol{\tau}}$ is the stress tensor. The tangential stress balance for the internal interface is given by $\hat{\boldsymbol{n}} \cdot \boldsymbol{\tau}^{\boldsymbol{I}} \cdot \hat{\boldsymbol{n}} = 2\mu_t \frac{\partial w}{\partial z}$ where $\hat{\boldsymbol{n}} = \hat{\boldsymbol{z}}$ in the lubrication approximation. In the lubrication approximation, the term of capillary pressure jump can be approximated $(\frac{1}{R_1} + \frac{1}{R_2})\gamma = -\gamma \frac{\partial^2 h}{\partial x^2} - \gamma \frac{\partial^2 h}{\partial y^2}$. Using Equation (3.2c) to obtain the pressure at the top layer p_t and employing an assumption commonly used in thin film spreading problems that the product of the aspect ratio and the capillary number must be small, $\frac{\mu U}{\gamma} \cdot \frac{L}{H} << 1$,[154] the Laplace pressure jump dominates the viscous stress term. Therefore the normal stress boundary condition becomes

$$p_t = p_{atm} + \rho_t g h - \gamma \frac{\partial^2 h}{\partial x^2} - \gamma \frac{\partial^2 h}{\partial y^2}. \tag{3.5a}$$

The ratio $\frac{\mu U}{\gamma}\cdot\frac{L}{H}$ is $5\times10^{-4}\sim5\times10^{-3}$ in our experiments, fulfilling the assumed condition. Combining Equation (3.5a) with Equation (3.2c) and Equation (3.3c), the pressure in the bottom layer is given by

$$p_b = p_{atm} + \rho_t g h + \Delta\rho g b - \gamma\frac{\partial^2 h}{\partial x^2} - \gamma\frac{\partial^2 h}{\partial y^2}. \tag{3.5b}$$

The integration of Equations (3.2a), (3.2b), (3.3a) and (3.3b), and the application of boundary conditions gives the parabolic velocity profiles,

$$u_t(x,y,z,t) = \frac{1}{2\mu_t}\frac{\partial p_t}{\partial x}z(z-2h) + \frac{1}{2\mu_t}\frac{\partial p_t}{\partial x}b(2h-b+2\lambda(b-h)) - \frac{1}{2\mu_b}\frac{\partial p_b}{\partial x}b^2, \tag{3.6a}$$

$$u_b(x,y,z,t) = \frac{1}{2\mu_b}\frac{\partial p_b}{\partial x}z(z-2b) + \frac{1}{2\mu_b}\frac{\partial p_t}{\partial x}(2b-2h)z, \tag{3.6b}$$

$$v_t(x,y,z,t) = \frac{1}{2\mu_t}\frac{\partial p_t}{\partial y}z(z-2h) + \frac{1}{2\mu_t}\frac{\partial p_t}{\partial y}b(2h-b+2\lambda(b-h)) - \frac{1}{2\mu_b}\frac{\partial p_b}{\partial x}b^2, \tag{3.7a}$$

$$v_b(x,y,z,t) = \frac{1}{2\mu_b}\frac{\partial p_b}{\partial y}z(z-2b) + \frac{1}{2\mu_b}\frac{\partial p_t}{\partial y}(2b-2h)z. \tag{3.7b}$$

The internal interface is given by $z = b(x,y,t)$. The kinematic condition requires that the difference between z and $b(x,y,t)$ be equal to zero at all times,

$$F_{\text{int}} \equiv z - b(x,y,t) = 0.$$

Applying the material derivative to the kinematic condition yields

$$\frac{DF_{\text{int}}}{Dt} = \frac{\partial F_{\text{int}}}{\partial t} + u_{\text{int}}\frac{\partial F_{\text{int}}}{\partial x} + v_{\text{int}}\frac{\partial F_{\text{int}}}{\partial y} + w_{\text{int}}\frac{\partial F_{\text{int}}}{\partial z} = 0,$$

which gives the equation of motion for the interface $b(x, y, t)$

$$-\frac{\partial b}{\partial t}+u_{int}(-\frac{\partial b}{\partial x})+v_{int}(-\frac{\partial b}{\partial y})+w_{int}=0\,. \tag{3.8}$$

Integrating the continuity equation from 0 to $b(x, y, t)$ and applying the Leibniz rule for the z-direction velocity yields

$$w_{int}(x,y,b,t)+\frac{\partial}{\partial x}\int_0^{b(x,y,t)}u_b dz-u_{\text{int}}(x,y,b,t)\frac{\partial b}{\partial x}+\frac{\partial}{\partial y}\int_0^{b(x,y,z,t)}v_b dz-v_{\text{int}}(x,y,b,t)\frac{\partial b}{\partial y}=0\,. \tag{3.9}$$

Combining Equation (3.8) and Equation (3.9) gives

$$\frac{\partial b}{\partial t}=-\frac{\partial}{\partial x}\int_0^{b(x,y,t)}u_b dz-\frac{\partial}{\partial y}\int_0^{b(x,y,z,t)}v_b dz\,. \tag{3.10}$$

The temporal evolution of the internal interface can be obtained by combining Equation (3.6b) and Equation (3.7b), to give

$$\begin{aligned}\frac{\partial b}{\partial t}=&-\frac{\partial}{\partial x}[\frac{1}{2\mu_b}\frac{\partial p_t}{\partial x}(\frac{b^3}{3}-hb^2)+\frac{-1}{3\mu_b}\frac{\partial b}{\partial x}(\Delta\rho g b^3)]\\&-\frac{\partial}{\partial y}[\frac{1}{2\mu_b}\frac{\partial p_t}{\partial y}(\frac{b^3}{3}-hb^2)+\frac{-1}{3\mu_b}\frac{\partial b}{\partial y}(\Delta\rho g b^3)]\end{aligned}\,. \tag{3.11a}$$

Similarly, the temporal evolution of the external interface obtained from application of the material derivative is given by

$$\frac{\partial h}{\partial t}=-\frac{\partial}{\partial x}(\int_0^{b(x,y,t)}u_b dz+\int_{b(x,y,t)}^{h(x,y,t)}u_t dz)-\frac{\partial}{\partial y}(\int_0^{b(x,y,z,t)}v_b dz+\int_{b(x,y,t)}^{h(x,y,t)}v_t dz)\,.$$

Using the velocity profiles obtained from Equations (3.6a) – (3.7b), we obtain the differential equation for external interface

$$\begin{aligned}\frac{\partial h}{\partial t}=&-\frac{\partial}{\partial x}[\frac{-1}{3\mu_t}\frac{\partial p_t}{\partial x}(h-b)^3+\frac{1}{2\mu_b}\frac{\partial p_t}{\partial x}b(b-h)(2h-b)+\frac{1}{2\mu_b}\frac{\partial p_b}{\partial x}(\frac{1}{3}b^3-b^2h)]\\&-\frac{\partial}{\partial y}[\frac{-1}{3\mu_t}\frac{\partial p_t}{\partial y}(h-b)^3+\frac{1}{2\mu_b}\frac{\partial p_t}{\partial y}b(b-h)(2h-b)+\frac{1}{2\mu_b}\frac{\partial p_b}{\partial y}(\frac{1}{3}b^3-b^2h)]\end{aligned}\,. \tag{3.11b}$$

Nondimensionalizing Equation (3.11a) using $b = Hb^*, h = Hh^*, x = Lx^*, y = L_2 y^*, z = Hz^*$, where L is the composite drop length, L_2 is the drop width, and H is the height of the composite drop as shown in Figure 3.3, yields the following equation after dropping the tilde for the dimensionless variables:

$$\frac{H}{T_c}\frac{\partial b}{\partial t} = \frac{\Delta\rho g}{3\mu_b}\frac{H^4}{L^2}\{\frac{\partial}{\partial x}(b^3\frac{\partial b}{\partial x}) - \frac{\rho_t}{2\Delta\rho}\frac{\partial}{\partial x}[(\frac{\partial h}{\partial x} - \frac{\gamma}{\rho_t g L^2}\frac{\partial^3 h}{\partial x^3} - \frac{\gamma}{\rho_t g L^2}\frac{\partial^3 h}{\partial x \partial y^2})(b^3 - 3b^2 h)]\}$$
$$+ \frac{\Delta\rho g}{3\mu_b}\frac{H^4}{L_2^2}\{\frac{\partial}{\partial y}(b^3\frac{\partial b}{\partial y}) - \frac{\rho_t}{2\Delta\rho}\frac{\partial}{\partial y}[(\frac{\partial h}{\partial y} - \frac{\gamma}{\rho_t g L^2}\frac{\partial^3 h}{\partial x^3} - \frac{\gamma}{\rho_t g L^2}\frac{\partial^3 h}{\partial y \partial x^2})(b^3 - 3b^2 h)]\}.$$

The necessity of a second length scale L_2 is discussed by Szeri[154] in deriving three dimensional lubrication theory. This equation suggests a time scaling of $T_c = 3\mu_b L^2 / \Delta\rho g H^3$ for the internal interface motion, which is identical to Equation (3.1) except for the factor of three. The resulting dimensionless governing equation for the interface motion is given by Equation (3.l2).

$$\frac{\partial b}{\partial t} = \{\frac{\partial}{\partial x}(b^3\frac{\partial b}{\partial x}) - \frac{\rho_t}{2\Delta\rho}\frac{\partial}{\partial x}[(\frac{\partial h}{\partial x} - \frac{\gamma}{\rho_t g L^2}\frac{\partial^3 h}{\partial x^3} - \frac{\gamma}{\rho_t g L^2}\frac{\partial^3 h}{\partial x \partial y^2})(b^3 - 3b^2 h)]\}$$
$$+ \frac{L^2}{L_2^2}\{\frac{\partial}{\partial y}(b^3\frac{\partial b}{\partial y}) - \frac{\rho_t}{2\Delta\rho}\frac{\partial}{\partial y}[(\frac{\partial h}{\partial y} - \frac{\gamma}{\rho_t g L^2}\frac{\partial^3 h}{\partial x^3} - \frac{\gamma}{\rho_t g L^2}\frac{\partial^3 h}{\partial y \partial x^2})(b^3 - 3b^2 h)]\} \quad (3.12)$$

The internal interface profile $b(x, y, t)$ depends on the external interface profile $h(x, y, t)$ (see Figure 3.6), the density of the lighter fluid ρ_t, the density difference between the two fluids $\Delta\rho$, the surface tension of the lighter fluid γ and the viscosity of the heavier fluid μ_b. In addition to the evolution equation given by Equation (3.12), mass conservation of the fluids in the top and bottom components of the composite drop must be invoked (see Figure 3.6a for the definition of the relevant domain),

$$\rho_t(\iint_{S_1} h(x,y,t)dxdy + \iint_{S_2}(h(x,y,t) - b(x,y,t))dxdy = m_t, \text{ and} \quad (3.13a)$$

$$\rho_b(\iint_{S_2} b(x,y,t)dxdy + \iint_{S_3} h(x,y,t)dxdy) = m_b\,, \tag{3.13b}$$

where m_t and m_b are the masses of the lighter and heavier fluids respectively, and $V_1 = \iint_{S_2} b(x,y,t)dxdy$ and $V_2 = \iint_{S_3} h(x,y,t)dxdy$ indicate the volumes occupied by the heavier fluid under the internal interface in the central portion of the composite drop and under the external interface in the end portion of the drop where the fluids do not overlap.

Equation (3.12) shows that the flow behavior in the *x* and *y* direction is similar if we permute the role of *x* and *y* in the right hand side of the equation. For the flow in the *x* direction, the first term on the right hand side $\frac{\partial}{\partial x}(b^3\frac{\partial b}{\partial x})$ corresponds to the gravity current and the second term $-\frac{\rho_t}{2\Delta\rho}\frac{\partial}{\partial x}[(\frac{\partial h}{\partial x} - \frac{\gamma}{\rho_t g L^2}\frac{\partial^3 h}{\partial x^3} - \frac{\gamma}{\rho_t g L^2}\frac{\partial^3 h}{\partial x \partial y^2})(b^3 - 3b^2 h)$ represents the coupling of the evolution of the external interface, *h*, to the internal interface, *b*. If the external interface is in static equilibrium, then the second term is identically zero, as shown by taking the first order derivative of the Young-Laplace equation for the equilibrium drop shape: $h - \frac{\gamma}{\rho_t g L^2}\frac{\partial^2 h}{\partial x^2} - \frac{\gamma}{\rho_t g L^2}\frac{\partial^2 h}{\partial y^2} = 0$. In cases where the composite drop shape deviates from equilibrium, then depending on the extent of the deviation from the equilibrium shape and the value of $\rho_t / \Delta\rho$, the coupling term can have a significant impact on the evolution of the internal interface. Our observation that the external interface does not change during Stage 2 beyond our detection limits for almost all the fluid pairs suggests that the second term is negligible in these experiments. However, as the density difference becomes as large as 20%, we observe more significant changes in the external interface, which may influence the internal fluid motion. In later comparisons between experimental data and analysis, we neglect this small change.

Equation (3.12) shows that there are several relevant dimensionless groups, including a fractional density difference $\rho_t / \Delta\rho$, a Bond number $\gamma / \rho_t g L^2$, and an aspect ratio L / L_2 (the ratio of length by width as shown in Figure 3.3). The time scale for the evolution of the internal interface, *b*, does not explicitly depend on the viscosity of the upper, lighter fluid as suggested by the experiments shown in Figure 10b. However, the evolution of the external interface shape *h*(*x*, *y*, *t*) depends on both the heavier fluid viscosity and the lighter fluid viscosity, thus causing the evolution of the internal interface to implicitly depend on both viscosities through the coupling given in Equation (3.12). Thus, the simplification that the external interface is in static equilibrium effectively removes any dependence on the lighter fluid viscosity. This suggests that the lack of full collapse shown in Figure 3.11b is a direct result of motion of the external interface, even though this motion may be smaller than our ability to detect it. We note in particular that the fluid pairs AH and AI shown in Figure 3.11 have the largest density differences. These cases exhibited measurable changes in the external interface shape, leading to a more prominent coupling between the internal interface *b*(*x*,*y*,*t*) and the external interface *h*(*x*,*y*,*t*), and the most prominent deviation from a simple gravity current.

3.7 Simulation Results and Comparison with Experiments

3.7.1 Simulation method

Since the drops we examine are neither axisymmetric nor planar symmetric, modeling the complete situation would require solving Equation (3.12) for a fully three dimensional flow. Simulations of free-surface flows with fully three-dimensional flow are computationally intensive[110], and so we chose to solve the two-dimensional version of Equation (3.12) for ease of simulation. A two dimensional simulation still provides qualitative information that can be

compared with the experimental observations of the evolution of the displacement of the internal interface, The two-dimensional assumption simplifies the problem by reducing the aspect ratio for the characteristic lengths in the *x* and *y* directions to zero, as well as removing the complication of coupled flow in the *x*, *y* and *z* directions due to mass conservation. The resulting governing equation is

$$\frac{\partial b}{\partial t} = \frac{\partial}{\partial x}(b^3 \frac{\partial b}{\partial x}) - \frac{\rho_t}{2\Delta\rho}\frac{\partial}{\partial x}[(\frac{\partial h}{\partial x} - \frac{\gamma}{\rho_t g L^2}\frac{\partial^3 h}{\partial x^3})(b^3 - 3b^2 h)]. \qquad (3.12')$$

We assume a constant external composite drop shape $h(x,t) = \tilde{h}_{eqm}(x)$, consistent with the experimental observations of Figure 3.5. This simplification decouples the mutual dependence of the internal interface $b(x,t)$ and external interface $h(x,t)$. We assume an equilibrium shape for the external interface given by the two-dimensional Young-Laplace equation subject to the lubrication approximation, $\gamma \tilde{h}''_{eqm} = \rho g \tilde{h}_{eqm}$. After scaling with the height and length of the composite drop such that $\tilde{h}_{eqm} \sim H h_{eqm}$, $\tilde{x} \sim L x$, the dimensionless equilibrium drop shape is

$$h_{eqm} = \frac{\cosh(Bo^{1/2}) - \cosh(x \cdot 2Bo^{1/2})}{\cosh(Bo^{1/2}) - 1}, \qquad (3.14)$$

where $Bo = \rho_t g L^2 / \gamma$ defines the Bond number for the composite drop. In the simulation, choosing the equilibrium shape for the external interface means the second term on right hand side of Equation (3.12') is zero and the internal interface equation then reduces to

$$\frac{\partial b}{\partial t} = \frac{\partial}{\partial x}(b^3 \frac{\partial b}{\partial x}) = \frac{\partial^2}{\partial x^2}(\frac{1}{4}b^4). \qquad (3.12^*)$$

We require an initial condition for the internal interface at the beginning of Stage 2. As suggested by the nearly vertical internal interface configuration at the end of Stage 1 in our experiments

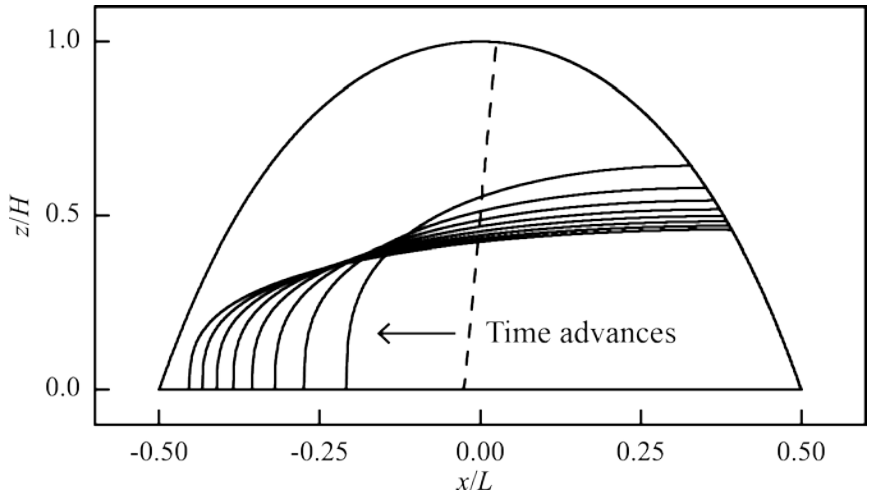

Figure 3.12. Evolution of the dimensionless internal interface profile for a two-dimensional composite drop assuming an equilibrium composite drop shape. Internal interface profiles are shown for dimensionless timesteps from 0 to 8 time units with 1

(Figure 3.4), we choose a steeply sloped linear profile given by $b = 19.964x + 0.499$, which is the line connecting the two points (-0.025, 0) and (0.025, $h_{eqm}(0.025)$). We use a slightly tilted line since a vertical line presents difficulties in taking derivatives of the interface profile. The initial interface for the simulation is shown by the dashed line in Figure 3.12.

Since Equation (3.12*) is a second order nonlinear diffusion equation, in addition to the initial condition $b(x,0)$ as specified above, we set the boundary condition as $b(x_f,t) = h_{eqm}(x_f)$ and $b(x_b,t) = 0$ for all time. The coordinates $x_f(t)$ and $x_b(t)$ are defined as the contact positions of the internal and external interfaces, respectively, as shown in Figure 3.6a. The specification of initial and boundary conditions along with the mass conservation condition, Equation (3.13), guarantees the existence and uniqueness of the solution of Equation (3.12*)[37,166]. The positions $x_f(t)$ and $x_b(t)$ are determined by this unique solution to the evolution equation. The position $x_b(t)$ is taken to be the mesh point at which the interface intersects the solid substrate. The position $x_f(t)$ is taken to be the mesh point at which the interface intersects the

external interface, adjusted to conserve the volume of the heavier drop $\int_{x_b(t)}^{x_f(t)} b(x,y,t)dxdy = V_b$.

For the simulation, the conservation of mass conditions that depend on h_{eqm} (see Equation. (3.14)), become requirements for area conservation for each fluid component in two dimensions. As the differential equation will be discretized by a co-volume method as discussed later, this area conservation method is satisfied automatically. The interface height at the left boundary point $b(x_b,t)$ is set to zero as the interface propagates, whereas the right boundary point $b(x_f,t)$ is forced to be on the external boundary h_{eqm} at discretized mesh points. This results in an error in area conservation of $\Delta x^2/2$, where Δx is the mesh size for the discretization.

The differential equation Equation (3.12*) is a type of degenerate parabolic problem which can be solved numerically using a co-volume method suggested by Baughman *et al*[167]. We use the explicit finite difference scheme to discretize the interface profile $b(x, t)$ as b_j^n, where j denotes the spatial index and n denotes the temporal index. The temporal derivative of b is given by $\frac{\partial b}{\partial t} = \frac{b_j^{n+1} - b_j^n}{\Delta t}$ in the explicit scheme, where Δt is the time step. The second order derivative for b^4 can be written symmetrically using the scheme analyzed by Baughman *et al*[167] for this type of problem, $\frac{\partial^2}{\partial x^2}(b^4) = \frac{(b_{j+1}^n)^4 - 2(b_j^n)^4 + (b_{j-1}^n)^4}{\Delta x^2}$. The final discretized expression for Equation (3.12*) is then given by

$$\frac{b_j^{n+1} - b_j^n}{\Delta t} = \frac{1}{4}\frac{(b_{j+1}^n)^4 - 2(b_j^n)^4 + (b_{j-1}^n)^4}{\Delta x^2}, \tag{3.15}$$

For this type of second order nonlinear diffusion equation, the stability criterion for the numerical scheme is given by an expression of the form $\Delta t \sim (\Delta x)^2$ [167, 168]. In addition to this stability criterion, b_j^n must be nonnegative to be in the physical subspace. Since the value of b_j^n

is nonnegative from the initial condition in our simulation, this requirement is satisfied. Thus Equation (3.15) is solved by iteration of time steps to obtain the time evolution of the interface profile *b* using the above explicit scheme. In our simulation, we calculate the evolution of interface from time $t = 0$ to $t = 8$. The time steps are determined using the stability criterion, once the spatial interval Δx is selected using the relationship $\Delta x = 1/n_x$, where n_x is the number of grid points. Figure 3.12 shows the evolution from $t = 0$ to $t = 8$ using a uniform grid $\Delta x = 1/1280 = 7.81\times10^{-4}$ and time step $\Delta t = 1.22\times10^{-7}$ with equilibrium external interface shape of h_{eqm}. For times beyond t = 8.8, the left hand side of the internal interface begins to collide with the external interface, where the recirculation in the wedge must be considered and Equation (3.15) is rendered invalid, thus we terminate the simulation after $t = 8$.

3.7.2 Evaluation of the simulation and convergence

As shown in Figure 3.12, the internal interface has a high slope at the contact point x_b which brings the lubrication approximation into question. For the lubrication approximation to be valid, the dimensional terms $\mathrm{Re}(u\frac{\partial u}{\partial x})$, $\mathrm{Re}(w\frac{\partial u}{\partial z})$ and $\frac{\partial^2 u}{\partial x^2}$ must be small compared with $\frac{\partial^2 u}{\partial z^2}$, where u and w are the horizontal and vertical components of the velocity, respectively. From the numerical solution of the evolution equation, Equation (3.12*), we calculate the velocities and relevant derivatives at an early time in the evolution of the gravity current. These comparisons show that the ratio of $\mathrm{Re}(u\frac{\partial u}{\partial x})$ to $\frac{\partial^2 u}{\partial z^2}$ is smaller than 0.001 over the entire domain. The ratio of $\mathrm{Re}(w\frac{\partial u}{\partial z})$ to $\frac{\partial^2 u}{\partial z^2}$ is smaller than 0.6 over the entire domain, and

declines quickly to smaller than 0.1 within 0.0006 spatial units (5 spatial grid points out of 6400). Unlike the other two ratios, the ratio of $\frac{\partial^2 u}{\partial x^2}$ to $\frac{\partial^2 u}{\partial z^2}$ is large at the contact point x_b due to the large slope; however, the ratio of these two terms declines quickly to smaller than 0.1 within 0.002 spatial units (15 spatial grid points out of 6400). Therefore, the lubrication assumption fails very near the corner and is satisfied away from the contact point x_b.

The governing equation of motion Equation (3.12*) is of the same form as that derived in the gravity current of Huppert[37], with different boundary conditions. The solution obtained by Huppert also has a high slope at the front of the current, and the lubrication approximation is also violated near the moving contact line. Nevertheless, the lubrication solution describes the experimentally observed shape of the gravity current well and it describes the propagation speed of the gravity front very well. Gratton *et al*[169] and Betelú *et al*[170] address in more detail the agreement of the gravity current profiles with experiments even though the lubrication approximation fails at the corner. These prior results and our examination of our numerical results justify the use of the lubrication approximation to qualitatively describe the experimental observations of the evolution of the shape and propagation speed of the internal interface.

To examine convergence, we first maintain a spatial mesh size of $\Delta x = 1/1280 = 7.81\times10^{-4}$ and vary the temporal step from $\Delta t = 9.77\times10^{-7}$ to $\Delta t = 6.10\times10^{-8}$ to check the error dependence on time steps[171]. As this nonlinear diffusion equation does not have an analytical solution, we define the global error comparing the interface profile at t = 1 with the finest case where $\Delta x = 7.81\times10^{-4}$ and $\Delta t = 3.05\times10^{-8}$ using the square norm

$$E_{\Delta t} = [\frac{1}{n_x}\sum_{j=1}^{n_x}(b_j^{t=1}|_{\Delta t} - b_j^{t=1}|_{\Delta t=3.05\times10^{-8}})^2]^{1/2}, \qquad (3.16)$$

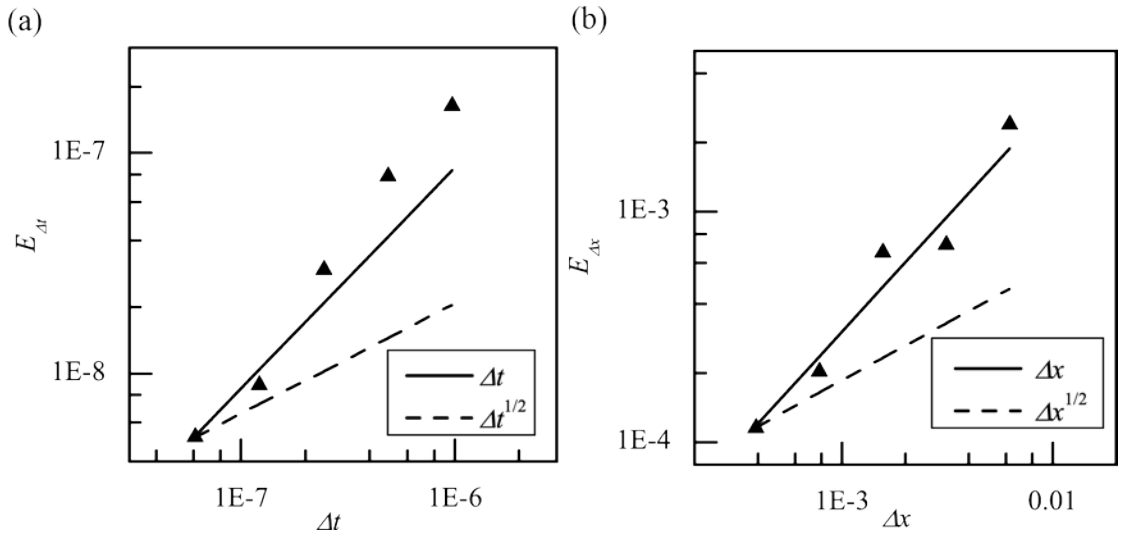

Figure 3.13. a) Global error as a function of time step (solid triangles represents the error defined by Equation (3.16) at different time steps). b) Global error as a function of spatial discretization (solid triangles represents the error defined by Equation (3.17) at various grid sizes).

where $b_j^{t=1}|_{\Delta t}$ is the calculated interface height with the time step Δt, and $b_j^{t=1}|_{\Delta t=3.05\times10^{-8}}$ represents the interface height with the finest time step. Due to the finite propagation speed of the nonlinear diffusion equation, functions at corners are not as smooth compared to the linear diffusion equation, thus the errors at the corners are the leading error in the numerical simulation[167]. Baughman *et al*[167] proved that for equations of this form, the estimated error approaches zero at least as rapidly as $C(\Delta x^{1/2}+\Delta t^{1/2})$, where C is a constant depending on the structure of the equation and boundary conditions.

Figure 3.13a shows that the global error for our simulation decreases with first order behavior in the time step, which agrees with the convergence criteria. Similarly, to examine the convergence with grid size, we calculate the global error for cases in which $\Delta t = 6.10\times10^{-8}$ is held fixed, but the grid varies from $\Delta x = 6.25\times10^{-3}$ to $\Delta x = 3.91\times10^{-4}$ while the stability

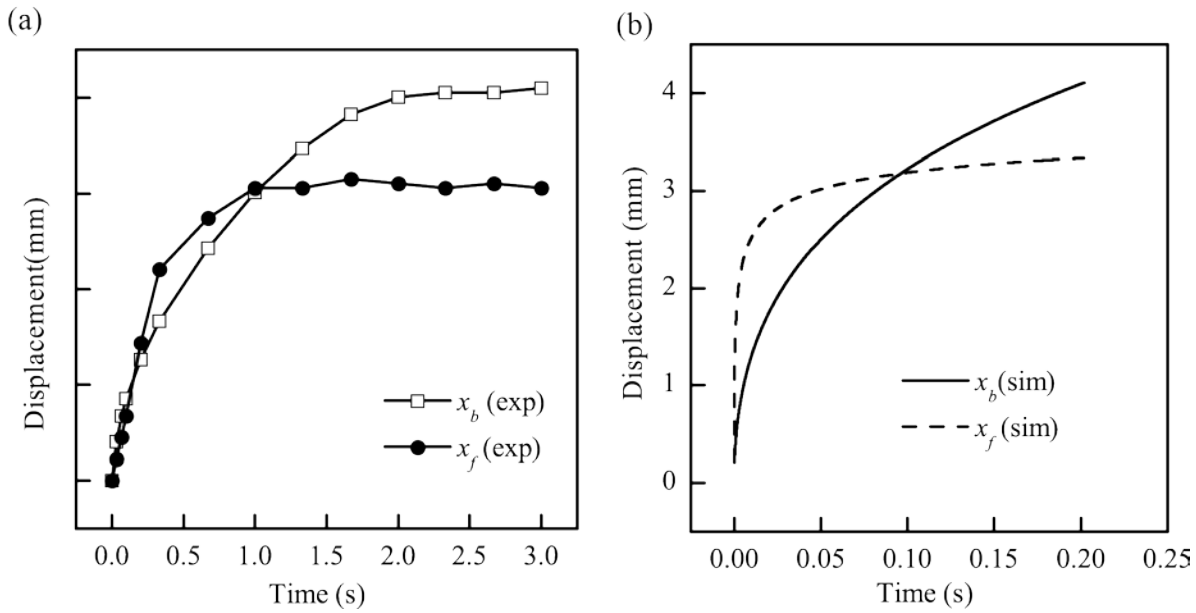

Figure 3.14. a) Measured Evolution of the two interface points in the composite drop. b) Simulation tracking the intersections of the internal interface with the rigid substrate and the external interface. Experiments and simulations both correspond to fluid pair DG with $\lambda = 1$, $Bo = 8$. The time scale for these two graphs differs by a factor of 10.

criterion $\Delta t \sim \Delta x^2$ is satisfied. In this case, the global error is computed by comparing each result with the finest discretization of $\Delta x = 1/5120 = 1.95 \times 10^{-4}$

$$E_{\Delta x} = [\frac{1}{n_x} \sum_{j=1}^{n_x} (b_j^{t=1}|_{\Delta x=\frac{1}{n_x}} - b_{jk}^{t=1}|_{\Delta x=\frac{1}{5120}})^2]^{1/2}, \tag{3.17}$$

where $k = 5120/n_x$ allows us to restrict the difference calculation at coarser grids to occur at the same x coordinate for different grid sizes. Figure 3.13b shows that the error of the simulation also decreases with nearly first order dependence on grid size. Convergence with spatial discretization is indicated for the numerical scheme with the same reasoning as for temporal discretization.

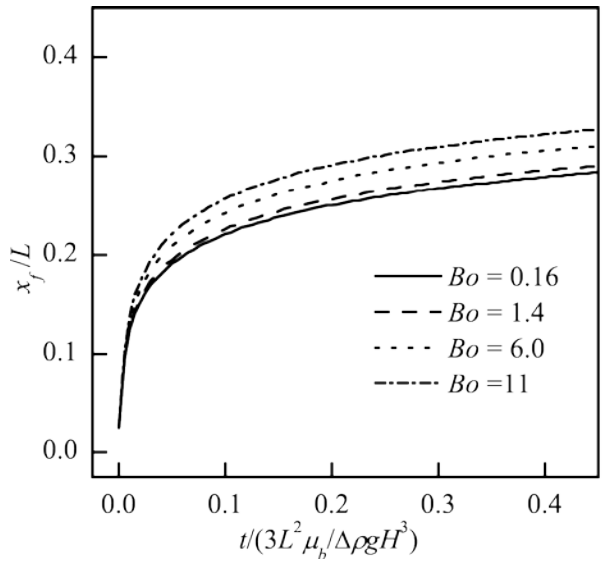

Figure 3.15 Displacement of the internal interface given by simulation of fluid pair DG with viscosity ratio $\lambda = 1$, for several values of Bond number.

3.7.3 Comparison of simulation results with experiment results

Figure 3.14a shows a typical result of a converged simulation for values of fluid properties taken from the experiments. The displacement of the interface is qualitatively similar to that observed in experiments as shown in Figure 3.4 and Figure 3.5b. The simulation only tracks the gravity current until the bottom point on the interface reaches the intersection of the external interface and the solid surface (the contact line).

As shown in Figure 3.14, the simulation qualitatively captures the displacement of the internal interface both at the top intersection with the external interface and at the bottom intersection with the solid surface. In both the experiment and simulation, the displacement of the point intersecting the external interface advances faster than that of the point intersecting the rigid substrate as would be expected from the contact line motion at a liquid or solid surface. In both the simulation and experiment, the intersection with the substrate moves farther than the intersection with the top interface before the gravity current reaches the external interface.

Since the external interface shape sets the initial and also boundary condition for the internal interface evolution, the gravity flattening of the external interface shape due to the Bond number variation (see Equation (3.14)) will also affect the internal interface motion.

Figure 3.15 shows the simulation examining the Bond number dependence of the top point of internal interface. As seen in experiments of Figure 3.10b, the simulation shows that the interface point evolves with almost the same initial rate while the displacement within the plateau region increases monotonically with respect to the Bond number.

Although the simulation results qualitatively agree with the experiments, the dimensional timescale in simulation is faster by about an order of magnitude. This discrepancy may arise from the quantitative comparison of the lubrication solution with experiments for a highly sloped interface[155, 156] but more likely arises because the simulation is two dimensional, while the experiments show three dimensional flow as seen in Figure 3.6. Similar to our results, in other studies of gravity driven currents, the observed characteristic velocity in three dimensional experiments is always smaller than that predicted by a two dimensional analysis because of the outer geometry and boundary conditions[138, 172, 173]. Despite the discrepancy in the magnitudes of the timescales, the scaling of the characteristic timescales for the gravity current with fluid properties and drop geometry agree well with the observed behavior, suggesting that the lubrication model captures most of the essential physics in the problem.

3.8 Summary

We have examined the coalescence of two sessile drops of miscible fluids with similar surface tensions and equal volumes. The fluid pairs can have different viscosities and densities, and the overall drop volumes vary. The fluid systems examined exhibit surface tensions of the

order of 60 to 70 mN/m, viscosities from about 4 to 41 mPa s, density differences from 0.01 to 0.43 g/cm^3, Bond numbers from 1 to 8, and contact angles of about 90º. The substrates consist of crosslinked PDMS, which is known to form a ridge beneath the contact line. The ridges do not completely pin contact lines but do inhibit their motion.

The coalescence of the two initial sessile drops occurs in three stages of motion: (1) bridge healing, (2) a gravity current, and (3) long-term diffusive mixing. Stage 1 is governed by minimization of capillary energy with coincident movement of the contact lines. The bridge healing of Stage 1 ends with a smooth external interface of the composite drop and no apparent twisting of streamlines that would cause advective mixing. The external interface achieves a nearly static shape within the resolution of our measurement for the remainder of the coalescence process, for density differences smaller than 0.2 g/cm^3. The timescale for Stage 1 is well separated from that of Stage 2 and thus the end of this stage forms an initial condition for the subsequent stages. Stage 2 is controlled by gravity and viscosity even for density differences as small as 1%. The fluids move toward a simple stratified configuration with no advective mixing and little to no diffusive mixing, consistent with the estimated Peclet number $Pe \approx 2500$. A three-dimensional lubrication analysis indicates that the predominant timescale for Stage 2 is $T_c = 3\mu_b L^2 / \Delta\rho g H^3$ as long as the external interface is very near equilibrium. Our analysis suggests that even small deviations of the external interface from equilibrium may cause the flow to have significant contributions from capillarity as well. The flow in Stage 2 is also governed by the additional dimensionless groups $\rho / \Delta\rho$ and $\gamma / \rho_t g L^2$. The experiments are in good agreement with the time scaling predicted by the analysis. The presence of small motions of the external interface leads to additional coupling with the flow of the upper, lighter fluid layer, and resistance due to the viscosity of this layer contributes to the motion of the internal interface. Thus, a

systematic deviation of the scaled displacement curves is observed to monotonically vary with the viscosity ratio. These conclusions are also supported by numerical solutions of a two-dimensional version of the equations developed in the analysis. However, the two-dimensional numerical solutions overestimate the characteristic speeds of the flow. This is likely due to the fact that the flow is in reality three-dimensional as shown by experiments. It is also possible that the high contact angle results in an aspect ratio of the composite drop that is too large to be accurately treated by the lubrication approximation.

Stage 2 concludes with the complete stratification of the two fluids after timescales of the order of tens of seconds. Finally in Stage 3, diffusive mixing occurs in the composite drop over timescales of the order of several minutes.

Experiments and simulations both show that once the initial bridge healing is complete, internal motion proceeds at low Reynolds number over very long timescales, even when the external interface appears to have long reached a static equilibrium. The fluid motion follows a well-defined gravity current even for very small density differences. These results show that external imaging of merging sessile drops is not sufficient to ensure that mixing of two fluid volumes is complete, and that such mixing often occurs only over much longer timescales than expected.

Appendix 3.1 Matlab code for the two dimensional gravity driven current

```
%%Difine grid structures, time steps, spatial discretization
I=640; xMax=1;%(length in unit of Length)
N=1024000; % time discretization units
q1=4000;      % save the profile every q1 units of    time
N1=N/q1;
tMax=1; % the total simulation time, dimensionlessly
Dt=tMax/N;% the temporal unit, dimensionless
Dx=2*xMax/I; % the spatial unit of x axis
b=zeros(I+1,1); % start with matrix with all elements being zero
bbuffer=zeros(I+1,1);
h=zeros(I+1,1);
rhot=1124.00; % the density of the top drop
rhob=1191.00; % the density of the bottom drop
g=9.78; % gravitational accelearation
gamma=0.066;
x0=0.05*xMax;
Length=0.5; % dimensional length in unit of cm
Height=0.30; % dimenaional heigh in unit of cm
capillary=sqrt(rhot*g/gamma)/100;% capillary in unit of cm^-1
bondnumber=capillary*Length;
rhotdeltarho=rhot/(rhob-rhot);
gammadeltarho=gamma/(rhob-rhot)/g*10000/Length^2; % the term gamma delta rho
```

```
x=(-xMax:Dx:xMax)';
%initial boundary condition xl0=-0.1, xr0=+0.1
xl0= -x0; xr0= x0; x0= 0.05;
h0=cosh(bondnumber)/(cosh(bondnumber)-1); % equilibrium shape of drop in 2 dimensions
C1=1/(cosh(bondnumber)-1);
Il0=I/2+xl0/(2*xMax)*I+1;
Ir0=I/2+xr0/(2*xMax)*I+1;
h=h0-C1*cosh(x.*bondnumber);
hprime=-C1*bondnumber*sinh(x.*bondnumber); % first order derivative of height
h2prime=-C1*(bondnumber^2)*cosh(x.*bondnumber);
h3prime=-C1*(bondnumber^3)*sinh(x.*bondnumber);
h4prime=-C1*(bondnumber^4)*cosh(x.*bondnumber); % fourth order derivative of height
%% initialization of the internal interface
for j=1:Il0
    b(j)=0;
end
for j=Il0+1:Ir0
    b(j)=h(Ir0)/(Ir0-Il0)*(j-Il0);
end
for j=Ir0+1:I+1
    b(j)=h(j);
end
%% initialization for the volume (area in 2D) of the bottom drop
```

```
Sarea=0; Newarea=0;
for j=1:I
      Sarea=Sarea+b(j);%Sarea is the real area multiplied by I/xMax
end
breakpoint=Ir0; leftbreakpoint=2;    bshow=zeros(I+1,q1+1);
breakpointhistory=zeros(q1+1,1);
leftbreakpointhistory=zeros(q1+1,1);
bprime=zeros(I+1,1);
b2prime=zeros(I+1,1);
term2=zeros(I+1,1);

bshow(:,1)=b; bbuffer=b; sumareajudge=0;
 sumareajudge1=0; % This sumareajudge will be used to judge volume conservation
leftindex=1;
 for n=1:N
    for i=leftbreakpoint:breakpoint %check to see how b changes with large slope?
          term2(i)=(b(i-1)^4-2*b(i)^4+b(i+1)^4)/4/Dx^2;
          bbuffer(i)=(term2(i))*Dt+b(i);
    end
 b=bbuffer;
      for index1=1:I
          Newarea=Newarea+b(index1); %Newarea is multiplied by I/xMax
      End
```

```
            index2=breakpoint;
        while (h(breakpoint)-b(breakpoint))/2*(index2-breakpoint)<(Newarea-Sarea)
          index2=index2+1;
        end
    if index2~= breakpoint
          for index3=breakpoint:index2
b(index3)=b(breakpoint)+(b(index2)-b(breakpoint))/(index2-breakpoint)*(index3-breakpoint);
          end
    end
        breakpoint=index2;
        Newarea=0;
%% identify the intersection of the internal interface with the external interface
        if h(leftbreakpoint)<b(leftbreakpoint)
                    leftindex=leftbreakpoint;
            while (h(leftindex)<b(leftindex))
                  b(leftindex)=h(leftindex);
                  leftindex=leftindex+1;
            end
           leftbreakpoint=leftindex;
        end
%% only record the position of internal interface at N1 unit of time to save memory
       if mod(n,N1)==0;
```

```
            k=n/N1;% changed k
            bshow(:,k+1)=b;
            breakpointhistory(k+1)=breakpoint;
            leftbreakpointhistory(k+1)=leftbreakpoint;
        end
    end
%% plot of the intersection of internal interface with the solid surface
front=zeros(q1+1,1);
    for r=1:q1
        for p=1:I
            if bshow(p,r)>=0.000005
            front(r)=p;
            break
            end
        end
    end
t=0:tMax/q1:tMax;
plot(t,front)
```

Appendix 3.2 Matlab code for the velocity at different positions

```
% set all the velocities and gradients as zero to start with
dbdx=zeros(I,1); d2bdx2=zeros(I,1); uvel=zeros(I,1); uvel2=zeros(I,1); vvel=zeros(I,1);
ududx=zeros(I,1); vdudy=zeros(I,1); dudx=zeros(I,1); dudy=zeros(I,1); dudx2=zeros(I,1);
db3xx=zeros(I,1); db4xx=zeros(I,1); d2udx2=zeros(I,1); d2udy22=zeros(I,1);
diff2=zeros(I,1); diff=zeros(I,1); vvel2=zeros(I,1); b2average=zeros(I,1);
%vectors have to be defined as 9600*1, so that vector(I) can be parametrized.
%% verib to store all the internal interface profile obtained from the gravity current case.
verib=bshow(:,4001);
newnumber=5250;
dbdx(2:I-1)=(-verib(1:I-2)+verib(2:I-1))*I/2;
dbdx(newnumber-1:I)=0;
d2bdx2(2:I-1)=(-dbdx(1:I-2)+dbdx(2:I-1))*I/2;
db2dx2(newnumber-1:I)=0;
uvel(2:I-1)=-1/3*(verib(2:I-1).^3-verib(1:I-2).^3)*I/2;
uvel(newnumber-1:I)=0;
db3xx(3:I)=(verib(3:I).^3+verib(1:I-2).^3-2*verib(2:I-1).^3)*I^2/4; % the second order
derivative of b^3
db4xx(3:I)=(verib(1:I-2).^4+verib(3:I).^4-2*verib(2:I-1).^4)*I^2/4;
vvel(2:I-1)=-db4xx(2:I-1)/12+1/3*verib(2:I-1).*db3xx(2:I-1);
% is much better in the sense of smoothness than
% vvel(2:I-1)=2/3*verib(2:I-1).^3.*d2bdx2(2:I-1)+verib(2:I-1).^2.*dbdx(2:I-1).^2;
vvel(newnumber-1:I)=0;
```

```
figure
hold on
plot(1700:2100,uvel(1700:2100),'k-','LineWidth',1.5)
plot(1700:2100,vvel(1700:2100),'b-.','LineWidth',1.5)
legend('u','v')
dudx(2:I-1)=(uvel(2:I-1)-uvel(1:I-2))*I/2;
dudx(newnumber-1:I)=0;
ududx(2:I-1)=uvel(2:I-1).*dudx(2:I-1);
for index=2:newnumber-1
    if abs(verib(index)-verib(index-1))>=1e-5
        dudy(index)=(uvel(index)-uvel(index-1))/(verib(index)-verib(index-1));
    end
end
dudy(newnumber-1:I)=0;
vdudy(2:I-1)=vvel(2:I-1).*dudy(2:I-1);
vdudy(newnumber:I)=0;
figure
hold on
plot(1700:2100,dudx(1700:2100),'k-','LineWidth',1.5);
plot(1700:2100,dudy(1700:2100),'b-','LineWidth',1.5);
legend('dudx','dudy');
d2udy2=dbdx;
d2udy2(newnumber-1:I)=0;
```

```
d2udx2(2:I-1)=(dudx(2:I-1)-dudx(1:I-2))*I/2;
d2udy22(2:I-1)=(dudy(2:I-1)-dudy(1:I-2))*I/2;
d2udx2(newnumber-1:I)=0;
d2udy22(newnumber-1:I)=0;
figure
  hold on
  plot(1700:2100,d2udy2(1700:2100),'k-','LineWidth',1);
  plot(1700:2100,d2udx2(1700:2100),'r:','LineWidth',1);
  legend('d2udy2','d2udx2');
  figure
    hold on
    plot(1:I-1,abs(ududx(1:I-1)./d2udy2(1:I-1)),'k-','LineWidth',1);
    plot(1:I-1,abs(vdudy(1:I-1)./d2udy2(1:I-1)),'b-.','LineWidth',1);
    plot(1:I-1,abs(d2udx2(1:I-1)./d2udy2(1:I-1)),'r:','LineWidth',1);
    legend('ratio ududx','ratio vdudy','ratio d2udx2');
```

Chapter 4 Conclusion

In this thesis, we study both the static and dynamic aspects of sessile drop coalescence. The first part of the thesis examines the stability of compound sessile drops at the axisymmetric configurations, where theoretical analysis, Surface Evolver simulations and experimental results are presented. The second part examines the dynamics of sessile drop coalescence with different densities and viscosities, where scaling analysis, gravity current modeling and experimental results are discussed. This thesis adds several new findings to the study of drop coalescence.

The equilibrium shape of an axisymmetric compound sessile drop is governed by seven dimensionless numbers using the Laplace equations in the presence of gravity. In the limit of zero gravity effects, the seven governing parameters reduce to only four parameters: the two ratios of interfacial tensions, the volume ratio of the two drops and the contact angle with the solid surface. These four parameters agree with other results in literature based on the assumption of negligible gravity effects.

A stability criterion for the axisymmetric compound sessile drop is determined through a perturbation approach where interfaces are assumed to be of Laplacian shapes. A direct result of this criterion states that a more dense drop resting on top of a less dense drop is not stable at the axisymmetric configuration. This contrasts with the experimental observation of a more dense drop floating on top of a flat less dense fluid surface, where the configuration possesses translational symmetry.

The stability criterion can be numerically evaluated in the limit of zero Bond number: to form a stable axisymmetric compound sessile drop, the density ratio must be smaller than a critical density ratio. The critical density ratio depends on the two ratios of interfacial tensions, the ratio of drop volumes and the contact angle at the solid surface. Qualitatively, the critical

density ratio is small for a high interfacial tension system, and large for a low interfacial tension system. Thus, stable axisymmetric drop configurations are rarely observed for organic/inorganic compound sessile drops in air because of the low critical density ratio. This stability criterion is verified using both Surface Evolver simulations and experiments for both high and low interfacial tension systems.

We experimentally realized stable axisymmetric compound sessile drops using a low interfacial tension system. The phase-separated system, obtained after mixing partially miscible fluids of benzyl alcohol and aqueous cesium chloride solutions, demonstrates a low interfacial tension of 3 to 6 mN/m. By varying the cesium chloride concentration, the resulted two phase systems have different density ratios but similar interfacial tensions. This low interfacial tension system allows experimental transitions from a stable axisymmetric configuration to an unstable axisymmetric configuration by varying the density ratio. The three approaches, the zero Bond number model, the Surface Evolver simulations and the experiments, in determining the stability criterion agree well at small Bond number. In larger Bond number cases, the modeling results made at the zero Bond number limit shows a small deviation from both the simulation and the experimental results.

The coalescence of two sessile drops is examined for miscible fluids with similar surface tensions and equal volumes. The fluids are prepared by mixing salt, water and glycerol, which have different viscosities and densities. The coalescence of the two drops can be divided by three stages of motion with well separated time scales: (1) bridge healing, (2) a gravity current, and (3) long-term diffusion. Stage 1 is governed by capillarity, after which the external interface achieves a nearly static shape for fluid pairs with density differences smaller than 0.2 g/cm^3 and the internal interface is almost vertical within the composite drop. The fluid motion after Stage 1 resembles a

gravity current for density difference as small as 1%. The motion during Stage 2 evolves toward a final stratified configuration and is controlled by gravity and viscosity. During Stage 2, the advective motion dominates the diffusion, consistent with the estimate of large value of Peclet number. Stage 2 lasts over timescales of seconds, and concludes with the complete stratification of the two fluids. During the final stage, Stage 3, diffusion occurs in the composite drop over timescales of minutes.

A lubrication analysis suggests that the fluid motion is characterized by a timescale $T_c = 3\mu_b L^2 / \Delta\rho g H^3$ during Stage 2 of the sessile drop coalescence, when the external interface is close to the equilibrium shape. The flow in Stage 2 is also governed by the additional dimensionless parameters $\rho / \Delta\rho$ and $\gamma / \rho_t g L^2$. The experimental results of drop coalescence for the internal motion agree with the time scaling predicted by the lubrication analysis. If the external interface is deviated from the equilibrium shape, both the upper and lower fluid layer cause resistance to the motion of the internal interface. Thus, a systematic deviation of the scaled displacement is observed to vary with the viscosity ratio monotonically. A two-dimensional lubrication analysis was evaluated numerically to compare with the flow during Stage 2. The numerical solutions agree qualitatively with the fluid flow, but overestimate the characteristic speeds of the flow. This is likely due to the discrepancy between simplified two dimensional solutions and the three-dimensional flow in experiments. It is also possible that the aspect ratio of the composite drop at high contact angle is too large to be accurately treated by the lubrication approximation.

The stability analysis of axisymmetric compound sessile drop provides a preliminary investigation in understanding the floatability at microdroplet scales, even though the results are limited by the assumption of Laplacian shape perturbations. The low interfacial tension system

proposed may also help to probe the floatability at large scales with varying density ratio with almost constant surface and interfacial tensions. The dynamic aspect of drop coalescence shows that merging sessile drops alone is not sufficient to ensure the mixing of two fluids. The side-to-side drop coalescence results in a stratified configuration for miscible fluids but not for the low interfacial tension system of separated phases. The difference suggests a more detailed analysis integrating the adhesion energy with the surface can determine the global energy minimum between Janus configurations and axisymmetric configurations.

References

[1] P.-G. de Gennes, F. Brochard-Wyart, and D. Quéré, *Capillarity and Wetting Phenomena: Drops, Bubbles, Pearls, Waves* (Springer, New York, 2004).

[2] A. Frohn and N. Roth, *Dynamics of Droplets* (Springer, New York, 2000).

[3] J.C. Berg, *An introduction to interfaces & colloids: the bridge to nanoscience* (World Scientific, 2010).

[4] J.S. Rowlinson and B. Widom, *Molecular Theory of Capillarity*, Reprint (Dover Publications, 2003).

[5] P. Tabeling, *Introduction to Microfluidics*, Reprint Ed (Oxford University Press, 2010).

[6] T.M. Squires and S.R. Quake, "Microfluidics: Fluid physics at the nanoliter scale," Rev. Mod. Phys. **77**(3), 977–1026 (2005).

[7] S.T. Thoroddsen, T.G. Etoh, and K. Takehara, "High-Speed Imaging of Drops and Bubbles," Annu. Rev. Fluid Mech. **40**(1), 257–285 (2008).

[8] H.A. Stone, A.D. Stroock, and A. Ajdari, "Engineering flows in small devices," Annu. Rev. Fluid Mech. **36**, 381 (2004).

[9] J. Berthier and K.A. Brakke, *The Physics of Microdroplets* (John Wiley & Sons, Hoboken, NJ, 2012).

[10] T. Thorsen, R.W. Roberts, F.H. Arnold, and S.R. Quake, "Dynamic pattern formation in a vesicle-generating microfluidic device," Phys. Rev. Lett. **86**(18), 4163–4166 (2001).

[11] S.L. Anna, N. Bontoux, and H.A. Stone, "Formation of dispersions using 'flow focusing' in microchannels," Appl. Phys. Lett. **82**(3), 364–366 (2003).

[12] J.D. Tice, H. Song, A.D. Lyon, and R.F. Ismagilov, "Formation of Droplets and Mixing in Multiphase Microfluidics at Low Values of the Reynolds and the Capillary Numbers," Langmuir **19**(22), 9127–9133 (2003).

[13] J. Eggers, “Drop formation - an overview,” Zamm **85**(6), 400–410 (2005).

[14] S.T. Thoroddsen and K. Takehara, “The coalescence cascade of a drop,” Phys. Fluids **12**(6), 1265 (2000).

[15] A. Menchaca-Rocha, A. Martínez-Dávalos, R. Núñez, S. Popinet, and S. Zaleski, “Coalescence of liquid drops by surface tension,” Phys. Rev. E **63**, 046309 (2001).

[16] L. Duchemin, J. Eggers, and C. Josserand, “Inviscid coalescence of drops,” **487**, 167–178 (2002).

[17] C. Andieu, D.A. Beysens, V.S. Nikolayev, and Y. Pomeau, “Coalescence of sessile drops,” J. Fluid Mech. **453**, 427 (2002).

[18] H.P. Kavehpour, “Coalescence of Drops,” Annu. Rev. Fluid Mech. **47**(1), 245–268 (2015).

[19] S. Torza and S. Mason, “Three-phase interactions in shear and electrical fields,” J. Colloid Interface Sci. **33**(1), 67 (1970).

[20] R. Johnson and S. Sadhal, “Fluid mechanics of compound multiphase drops and bubbles,” Annu. Rev. Fluid Mech. **17**, 289–320 (1985).

[21] S.S. Sadhal, P.S. Ayyaswamy, and J.N. Chung, *Transport Phenomena with Drops and Bubbles* (Springer-Verlag, New York, 1997).

[22] R. Narhe, D. Beysens, and V.S. Nikolayev, “Contact line dynamics in drop coalescence and spreading,” Langmuir **20**, 1213 (2004).

[23] D.A. Beysens and R.D. Narhe, “Contact line dynamics in the late-stage coalescence of diethylene glycol drops,” J. Phys. Chem. B **110**, 22133 (2006).

[24] P.G. DeGennes, “Wetting: statics and dynamics,” Rev. Mod. Phys. **57**, 827 (1985).

[25] D. Bonn, J. Eggers, J. Indekeu, and J. Meunier, “Wetting and spreading,” Rev. Mod. Phys. **81**, 739–805 (2009).

[26] L. Mahadevan, M. Adda-Bedia, and Y. Pomeau, “Four-phase merging in sessile compound drops,” J. Fluid Mech. **451**, 411–420 (2002).

[27] M.J. Neeson, R.F. Tabor, F. Grieser, R.R. Dagastine, and D.Y.C. Chan, “Compound sessile drops,” Soft Matter **8**(43), 11042 (2012).

[28] H. Riegler and P. Lazar, “Delayed coalescence behavior of droplets with completely miscible liquids,” Langmuir **24**, 6395 (2008).

[29] S. Karpitschka and H. Riegler, “Quantitative experimental study on the transition between fast and delayed coalescence of sessile droplets with different but completely miscible liquids,” Langmuir **26**, 11823 (2010).

[30] R. Borcia, S. Menzel, M. Bestehorn, S. Karpitschka, and H. Riegler, “Delayed coalescence of droplets with miscible liquids: lubrication and phase field theories.,” Eur. Phys. J. E **34**, 24 (2011).

[31] S. Karpitschka and H. Riegler, “Noncoalescence of sessile drops from different but miscible liquids: hydrodynamic analysis of the twin drop contour as a self-stabilizing traveling wave,” Phys. Rev. Lett. **109**, 066103 (2012).

[32] S. Karpitschka and H. Riegler, “Sharp transition between coalescence and non-coalescence of sessile drops,” J. Fluid Mech. **743**, R1 (2014).

[33] C.M. Phan, B. Allen, L.B. Peters, T.N. Le, and M.O. Tade, “Can water float on oil?,” Langmuir **28**(10), 4609–13 (2012).

[34] C.M. Phan, “Stability of a floating water droplet on an oil surface.,” Langmuir **30**(3), 768–73 (2014).

[35] H.E. Huppert and J.E. Simpson, “The slumping of gravity currents,” J. Fluid Mech. **99**, 785 (1980).

[36] N. Didden and T. Maxworthy, “The viscous spreading of plane and axisymmetric gravity currents,” J. Fluid Mech. **121**, 27 (1982).

[37] H.E. Huppert, “The propagation of two-dimensional and axisymmetric viscous gravity currents over a rigid horizontal surface,” J. Fluid Mech. **121**, 43 (1982).

[38] J.E. Simpson, *Gravity currents: In the environment and the laboratory*, 2nd ed. (Cambridge University Press, 1999).

[39] S. Rienstra, “The shape of a sessile drop for small and large surface tension,” J. Eng. Math. 193–202 (1990).

[40] A.W. Adamson and A.P. Gast, *Physical Chemistry of Surfaces*, 6th ed. (Wiley, New York, 1997).

[41] P. Pujado and L. Scriven, “Sessile lenticular configurations: translationally and rotationally symmetric lenses,” J. Colloid Interface Sci. **40**, (1972).

[42] L. Boruvka and A.W. Neumann, “Generalization of the classical theory of capillarity,” J. Chem. Phys. **66**, 5464 (1977).

[43] R. Aveyard and J. Clint, “Liquid lenses at fluid/fluid interfaces,” J. Chem. Soc. Faraday Trans. **1**(4), 1397–1403 (1997).

[44] D. Chatain, P. Wynblatt, M. De Ruijter, J. De Conninck, and C. Carter, “Shape of two-phase drops in the presence of perfect wetting,” Acta Mater. **47**, 3049–3056 (1999).

[45] M. Seo, C. Paquet, Z. Nie, S. Xu, and E. Kumacheva, “Microfluidic consecutive flow-focusing droplet generators,” Soft Matter **3**(8), 986 (2007).

[46] A. Abate and D. Weitz, “High-order multiple emulsions formed in poly(dimethylsiloxane) microfluidics.,” Small **5**(18), 2030–2 (2009).

[47] O. Río and A. Neumann, “Axisymmetric Drop Shape Analysis: Computational Methods for the Measurement of Interfacial Properties from the Shape and Dimensions of Pendant and Sessile Drops.,” J. Colloid Interface Sci. **196**(2), 136–147 (1997).

[48] M. Ben Said, M. Selzer, B. Nestler, and D. Braun, “A phase-field approach for wetting phenomena of multiphase droplets on solid surfaces,” Langmuir (2014).

[49] S.G. Krantz and H.R. Parks, *The Geometry of Domains in Space* (Springer, 1999).

[50] V. Lubarda, “Mechanics of a liquid drop deposited on a solid substrate,” Soft Matter 10288–10297 (2012).

[51] J.F. Padday and A.R. Pitt, *The Stability of Axisymmetric Menisci*, Philos. Trans. R. Soc. A Math. Phys. Eng. Sci. **275**, 489–528 (1973).

[52] J.H. Snoeijer and B. Andreotti, “A microscopic view on contact angle selection,” Phys. Fluids **20**(5), 057101 (2008).

[53] S.R. Majumdar and D.H. Michael, *The Equilibrium and Stability of Two Dimensional Pendent Drops*, Proc. R. Soc. A Math. Phys. Eng. Sci. **351**, 89–115 (1976).

[54] P.T. Sumesh and R. Govindarajan, “The possible equilibrium shapes of static pendant drops.,” J. Chem. Phys. **133**(14), 144707 (2010).

[55] R.T. Rockafellar, *Convex Analysis* (Princeton University Press, Princeton, New Jersey, 1970).

[56] L. Landau and E. Lifshitz, *Mechanics, Vol. 1 of Course of Theoretical Physics*, 3rd Editio (Butterworth-Heinemann, 1976).

[57] H. Goldstein, P.C. Poole, and J.L. Safko, *Classical Mechanics* (Pearson, 2002).

[58] A. Demond and A. Lindner, “Estimation of interfacial tension between organic liquids and water,” Environ. Sci. Technol. **27**(12), 2318–2331 (1993).

[59] J. Gibbs, *The Scientific Papers of J Willard Gibbs. Vol 1, Thermodynamics* (Dover, New York, 1961).

[60] I. Ivanov, P.A. Kralchevsky, and A.D. Nikolov, “Film and line tension effects on the attachment of particles to an interface,” J. Colloid Interface Sci. **112**(1), 97 (1986).

[61] M. Rayner, G. Trägårdh, C. Trägårdh, and P. Dejmek, “Using the Surface Evolver to model droplet formation processes in membrane emulsification,” J. Colloid Interface Sci. **279**(1), 175–185 (2004).

[62] K. Brakke, “The surface evolver,” Exp. Math. **1**(2), 141–165 (1992).

[63] K.A. Brakke, *The Surface Evolver and the Stability of Liquid Surfaces*, Philos. Trans. R. Soc. A Math. Phys. Eng. Sci. **354**, 2143–2157 (1996).

[64] J. Guzowski, P.M. Korczyk, S. Jakiela, and P. Garstecki, *The structure and stability of multiple micro-droplets*, Soft Matter **8**, 7269 (2012).

[65] W.. Haynes, *CRC Handbook of Chemistry and Physics*, 81st ed. (Taylor & Francis group, New York, 2000).

[66] Y. Zhang, S.D. Oberdick, E.R. Swanson, S.L. Anna, and S. Garoff, “Gravity driven current during the coalescence of two sessile drops,” Phys. Fluids **27**(2), 022101 (2015).

[67] R. David, S.M. Dobson, Z. Tavassoli, M.G. Cabezas, and A.W. Neumann, “Investigation of the Neumann triangle for dodecane liquid lenses on water,” Colloids Surfaces A Physicochem. Eng. Asp. **333**(1-3), 12–18 (2009).

[68] H.-J. Butt, K. Graf, and M. Kappl, *Physics and Chemistry of Interfaces* (Wiley-VCH Verlag GmbH & Co. KGaA, Weinheim, 2003).

[69] D.J. Donahue, F.E. Bartell, U. Michigan, and A. Arbor, “The boundary tension at water-organic liquid interfaces,” J. Phys. Chem. **56**, 480–484 (1952).

[70] E.H.A. de Hoog and H.N.W. Lekkerkerker, “Measurement of the Interfacial Tension of a Phase-Separated Colloid−Polymer Suspension,” J. Phys. Chem. B **103**(25), 5274–5279 (1999).

[71] D.G.A.L. Aarts, M. Schmidt, and H.N.W. Lekkerkerker, “Direct visual observation of thermal capillary waves.,” Science **304**, 847–850 (2004).

[72] D.G.A.L. Aarts, R.F.A. Dullens, and H.N.W. Lekkerkerker, “Interfacial dynamics in demixing systems with ultralow interfacial tension,” New J. Phys. **7**, (2005).

[73] H.N.W. Lekkerkerker *et al.*, “Life at ultralow interfacial tension: Wetting, waves and droplets in demixed colloid-polymer mixtures,” Eur. Phys. J. B **64**, 341–347 (2008).

[74] J.O. Indekeu, D.G.A.L. Aarts, H.N.W. Lekkerkerker, Y. Hennequin, and D. Bonn, "Thermal fluctuation forces and wetting layers in colloid-polymer mixtures: Derivation of an interface potential," Phys. Rev. E - Stat. Nonlinear, Soft Matter Phys. **81**(4), (2010).

[75] M.C. van Loosdrecht, J. Lyklema, W. Norde, G. Schraa, and A.J. Zehnder, "The role of bacterial cell wall hydrophobicity in adhesion.," Appl. Environ. Microbiol. **53**(8), 1893–1897 (1987).

[76] Y. Liu, R. Lipowsky, and R. Dimova, "Concentration dependence of the interfacial tension for aqueous two-phase polymer solutions of dextran and polyethylene glycol," Langmuir **28**(8), 3831–3839 (2012).

[77] O. Olabisi, L.M. Robeson, and M.T. Shaw, *Polymer–Polymer Miscibility* (Academic Press, New York, 1979).

[78] F.S. Bates, "Polymer-polymer phase behavior," Science **251**(4996), 898–905 (1991).

[79] T.M. Duncan and J.A. Reimer, *Chemical Engineering Design and Analysis: An Introduction* (Cambridge University Press, Cambridge, 1998).

[80] E.B. Munday, J.C. Mullins, and D.D. Edie, "Vapor pressure data for toluene, 1-pentanol, 1-butanol, water, and 1-propanol and for the water and 1-propanol system from 273.15 to 323.15," J. Chem. Eng. Data **25**, 191–194 (1980).

[81] D. Ambrose and N.B. Ghiassee, "Vapour pressures, critical temperatures, and critical pressures of benzyl alcohol, octan-2-ol, and 2-ethylhexan-1-ol," J. Chem. Thermodyn. **22**, 307–311 (1990).

[82] D.M. Whelpdale and R. List, *The Coalescence process in raindrop growth*, J. Geophys. Res. **76**(12), 2836 (1971).

[83] J. Eggers, J.R. Lister, and H.A. Stone, "Coalescence of liquid drops," J. Fluid Mech. **401**, 293 (1999).

[84] D. Beysens and C.M. Knobler, "Growth of breath figures," Phys. Rev. Lett. **57**, 1433 (1986).

[85] J. Stringer and B. Derby, “Formation and stability of lines produced by inkjet printing,” Langmuir **26**, 10365 (2010).

[86] W.T. Pimbley, “Drop Formation from a Liquid Jet: A Linear One-dimensional Analysis Considered as a Boundary Value Problem,” IBM J. Res. Dev. **20**(2), 148–156 (1976).

[87] Z. Hu and R.C. Srivastava, *Evolution of Raindrop Size Distribution by Coalescence, Breakup, and Evaporation: Theory and Observations*, J. Atmos. Sci. **52**(10), 1761–1783 (1995).

[88] T.B. Low and R. List, *Collision, Coalescence and Breakup of Raindrops. Part I: Experimentally Established Coalescence Efficiencies and Fragment Size Distributions in Breakup*, J. Atmos. Sci. **39**(7), 1591–1606 (1982).

[89] T.B. Low and R. List, *Collision, Coalescence and Breakup of Raindrops. Part II: Parameterization of Fragment Size Distributions*, J. Atmos. Sci. **39**(7), 1607–1619 (1982).

[90] D.G.A.L. Aarts, H.N.W. Lekkerkerker, H. Guo, G.H. Wegdam, and D. Bonn, “Hydrodynamics of droplet coalescence,” Phys. Rev. Lett. **95**, 164503 (2005).

[91] G.. Charles and S.. Mason, “The mechanism of partial coalescence of liquid drops at liquid/liquid interfaces,” J. Colloid Sci. **15**(2), 105–122 (1960).

[92] G.. Charles and S.. Mason, “The coalescence of liquid drops with flat liquid/liquid interfaces,” J. Colloid Sci. **15**(3), 236–267 (1960).

[93] A.H. BROWN and C. HANSON, *Drop Coalescence in Liquid–Liquid Systems*, Nature **214**(5083), 76–77 (1967).

[94] A.F. Jones and S.D.R. Wilson, *The film drainage problem in droplet coalescence*, J. Fluid Mech. **87**(02), 263 (1978).

[95] D.Y.C. Chan, E. Klaseboer, and R. Manica, *Film drainage and coalescence between deformable drops and bubbles*, Soft Matter **7**(6), 2235 (2011).

[96] W.D. Ristenpart, P.M. McCalla, R. V. Roy, and H.A. Stone, “Coalescence of spreading droplets on a wettable substrate,” Phys. Rev. Lett. **97**, 064501 (2006).

[97] A. Oron, S.H. Davis, and S.G. Bankoff, “Long-scale evolution of thin liquid films,” Rev. Mod. Phys. **69**, 931 (1997).

[98] R.D. Narhe, D.A. Beysens, and Y. Pomeau, “Dynamic drying in the early-stage coalescence of droplets sitting on a plate,” Europhys. Lett. **81**, 46002 (2008).

[99] S.J. Gokhale, S. DasGupta, J.L. Plawsky, and P.C. Wayner, “Reflectivity-based evaluation of the coalescence of two condensing drops and shape evolution of the coalesced drop,” Phys. Rev. E **70**, 051610 (2004).

[100] N. Kapur and P.H. Gaskell, “Morphology and dynamics of droplet coalescence on a surface,” Phys. Rev. E **75**, 056315 (2007).

[101] M. Sellier and E. Trelluyer, “Modeling the coalescence of sessile droplets,” Biomicrofluidics **3**, 22412 (2009).

[102] J.B. Boreyko and C.-H. Chen, “Self-propelled dropwise condensate on superhydrophobic surfaces,” Phys. Rev. Lett. **103**, 184501 (2009).

[103] M.A. Nilsson and J.P. Rothstein, “The effect of contact angle hysteresis on droplet coalescence and mixing,” J. Colloid Interface Sci. **363**, 646 (2011).

[104] J.R. Castrejón-Pita, E.S. Betton, K.J. Kubiak, M.C.T. Wilson, and I.M. Hutchings, “The dynamics of the impact and coalescence of droplets on a solid surface,” Biomicrofluidics **5**, 14112 (2011).

[105] M.W. Lee, D.K. Kang, S.S. Yoon, and A.L. Yarin, “Coalescence of two drops on partially wettable substrates.,” Langmuir **28**, 3791 (2012).

[106] R. Li, N. Ashgriz, S. Chandra, J.R. Andrews, and S. Drappel, “Coalescence of two droplets impacting a solid surface,” Exp. Fluids **48**, 1025 (2010).

[107] Y.-H. Lai, M.-H. Hsu, and J.-T. Yang, “Enhanced mixing of droplets during coalescence on a surface with a wettability gradient,” Lab Chip **10**, 3149 (2010).

[108] Q. Liao, X. Zhu, S.M. Xing, and H. Wang, “Visualization study on coalescence between pair of water drops on inclined surfaces,” Exp. Therm. Fluid Sci. **32**, 1647 (2008).

[109] H. Wang, Q. Liao, X. Zhu, J. Li, and X. Tian, “Experimental studies of liquid droplet coalescence on the gradient surface,” J. Supercond. Nov. Magn. **23**, 1165 (2010).

[110] J.A. Diez and L. Kondic, “Computing three-dimensional thin film flows including contact lines,” J. Comput. Phys. **183**, 274 (2002).

[111] H. Wang, X. Zhu, Q. Liao, and P.C. Sui, “Numerical simulation on coalescence between a pair of drops on homogeneous horizontal surface with volume-of-fluid method,” J. Supercond. Nov. Magn. **23**, 1137 (2010).

[112] A. Eddi, K.G. Winkels, and J.H. Snoeijer, “Influence of Droplet Geometry on the Coalescence of Low Viscosity Drops,” Phys. Rev. Lett. **111**(14), 144502 (2013).

[113] A.U. Chen, P.K. Notz, and O. a Basaran, “Computational and experimental analysis of pinch-off and scaling.,” Phys. Rev. Lett. **88**(17), 174501 (2002).

[114] J.D. Paulsen, J.C. Burton, S.R. Nagel, S. Appathurai, M.T. Harris, and O. a Basaran, “The inexorable resistance of inertia determines the initial regime of drop coalescence.,” Proc. Natl. Acad. Sci. U. S. A. **109**(18), 6857–61 (2012).

[115] J.D. Paulsen, J.C. Burton, and S.R. Nagel, “Viscous to inertial crossover in liquid drop coalescence,” Phys. Rev. Lett. **106**(11), 1–4 (2011).

[116] S. Case and S. Nagel, “Coalescence in Low-Viscosity Liquids,” Phys. Rev. Lett. **100**(8), 084503 (2008).

[117] J. Eggers, *Nonlinear dynamics and breakup of free-surface flows*, Rev. Mod. Phys. **69**(3), 865–930 (1997).

[118] S.T. Thoroddsen, K. Takehara, and T.G. Etoh, “The coalescence speed of a pendent and a sessile drop,” J. Fluid Mech. **527**, 85–114 (2005).

[119] M. Wu, T. Cubaud, and C.M. Ho, “Scaling law in liquid drop coalescence driven by surface tension,” Phys. Fluids **16**(7), (2004).

[120] K. Fezzaa and Y. Wang, “Ultrafast X-ray phase-contrast imaging of the initial coalescence phase of two water droplets,” Phys. Rev. Lett. **100**(10), (2008).

[121] E. Ramé, S. Garoff, and K.R. Willson, “Characterizing the microscopic physics near moving contact lines using dynamic contact angle data,” Phys. Rev. E **70**, 031608 (2004).

[122] R. Borcia and M. Bestehorn, “Different behaviors of delayed fusion between drops with miscible liquids,” Phys. Rev. E **82**(3), 036312 (2010).

[123] M. Sellier, V. Nock, and C. Verdier, “Self-propelling coalescing droplets,” Int. J. Multiph. Flow **37**, 462 (2011).

[124] J.F. Hernández-Sánchez, L.A. Lubbers, A. Eddi, and J.H. Snoeijer, “Symmetric and asymmetric coalescence of drops on a substrate,” Phys. Rev. Lett. **109**, 184502 (2012).

[125] T.J. Johnson, D. Ross, and L.E. Locascio, “Rapid microfluidic mixing,” Anal. Chem. **74**(1), 45–51 (2002).

[126] C.Y. Lee, C.L. Chang, Y.N. Wang, and L.M. Fu, “Microfluidic mixing: A review,” Int. J. Mol. Sci. **12**(5), 3263–3287 (2011).

[127] H.E.H. Meijer, M.K. Singh, T.G. Kang, J.M.J. Den Toonder, and P.D. Anderson, “Passive and active mixing in microfluidic devices,” Macromol. Symp. **279**(1), 201–209 (2009).

[128] H. Song, M.R. Bringer, J.D. Tice, C.J. Gerdts, and R.F. Ismagilov, “Experimental test of scaling of mixing by chaotic advection in droplets moving through microfluidic channels,” Appl. Phys. Lett. **83**(22), 4664–4666 (2003).

[129] J.M. Ottino and S. Wiggins, “Designing optimal micromixers,” Science **305**, 485 (2004).

[130] J.M. Ottino and S. Wiggins, “Introduction: mixing in microfluidics,” Philos. Trans. R. Soc. A **362**, (2004).

[131] A.D. Stroock, S.K.W. Dertinger, A. Ajdari, I. Mezić, H.A. Stone, and G.M. Whitesides, “Chaotic mixer for microchannels,” Science **295**, 647 (2002).

[132] P. Paik, V.K. Pamula, M.G. Pollack, and R.B. Fair, “Electrowetting-based droplet mixers for microfluidic systems,” Lab Chip **3**, 28 (2003).

[133] C.-C. Chang and R.-J. Yang, “Electrokinetic mixing in microfluidic systems,” Microfluid. Nanofluidics **3**, 501 (2007).

[134] J.R. Castrejón-Pita, K.J. Kubiak, A.A. Castrejón-Pita, M.C.T. Wilson, and I.M. Hutchings, “Mixing and internal dynamics of droplets impacting and coalescing on a solid surface,” Phys. Rev. E **88**, 023023 (2013).

[135] F. Mugele, J.-C. Baret, and D. Steinhauser, “Microfluidic mixing through electrowetting-induced droplet oscillations,” Appl. Phys. Lett. **88**, 204106 (2006).

[136] A. V. Anilkumar, C.P. Lee, and T.G. Wang, “Surface-tension-induced mixing following coalescence of initially stationary drops,” Phys. Fluids A **3**, 2587 (1991).

[137] T. Séon, J.-P. Hulin, D. Salin, B. Perrin, and E.J. Hinch, “Buoyant mixing of miscible fluids in tilted tubes,” Phys. Fluids **16**(12), L103 (2004).

[138] T. Séon *et al.*, “Buoyancy driven miscible front dynamics in tilted tubes,” Phys. Fluids **17**(3), 031702 (2005).

[139] T. Séon, J. Znaien, D. Salin, J.P. Hulin, E.J. Hinch, and B. Perrin, “Transient buoyancy-driven front dynamics in nearly horizontal tubes,” Phys. Fluids **19**(12), 123603 (2007).

[140] S.M. Taghavi, T. Seon, D.M. Martinez, and I.A. Frigaard, “Buoyancy-dominated displacement flows in near-horizontal channels: the viscous limit,” J. Fluid Mech. **639**, 1 (2009).

[141] S.M. Taghavi, T. Séon, D.M. Martinez, and I.A. Frigaard, “Influence of an imposed flow on the stability of a gravity current in a near horizontal duct,” Phys. Fluids **22**, 031702 (2010).

[142] M.C. Lopes and E. Bonaccurso, “Evaporation control of sessile water drops by soft viscoelastic surfaces,” Soft Matter **8**, 7875 (2012).

[143] E.R. Jerison, Y. Xu, L.A. Wilen, and E.R. Dufresne, “Deformation of an elastic substrate by a three-phase contact line,” Phys. Rev. Lett. **106**(18), (2011).

[144] M.A. Nilsson, R.J. Daniello, and J.P. Rothstein, “A novel and inexpensive technique for creating superhydrophobic surfaces using Teflon and sandpaper,” J. Phys. D. Appl. Phys. **43**(4), 045301 (2010).

[145] J.H. Brannon and D. Magde, “Absolute Quantum Yield Determination by Thermal Blooming. Fluorescein,” J. Phys. Chem. **82**(6), 705–709 (1978).

[146] R. Sjöback, J. Nygren, and M. Kubista, “Absorption and fluorescence properties of fluorescein,” Spectrochim. Acta Part A Mol. Biomol. Spectrosc. **51**(6), L7–L21 (1995).

[147] P.C. Hiemenz and T.P. Lodge, *Polymer Chemistry* (Taylor & Francis group, New York, 2007).

[148] R. Sharma, R. Kalita, E.R. Swanson, T.E. Corcoran, S. Garoff, and T.M. Przybycien, “Autophobing on liquid subphases driven by the interfacial transport of amphiphilic molecules,” Langmuir **28**, 15212 (2012).

[149] N.J. Alvarez, L.M. Walker, and S.L. Anna, “A microtensiometer to probe the effect of radius of curvature on surfactant transport to a spherical interface,” Langmuir **26**(16), 13310–13319 (2010).

[150] N.J. Alvarez, L.M. Walker, and S.L. Anna, “A non-gradient based algorithm for the determination of surface tension from a pendant drop: Application to low Bond number drop shapes,” J. Colloid Interface Sci. **333**(2), 557–562 (2009).

[151] D. Merkt, a. Pototsky, M. Bestehorn, and U. Thiele, “Long-wave theory of bounded two-layer films with a free liquid–liquid interface: Short- and long-time evolution,” Phys. Fluids **17**(6), 064104 (2005).

[152] A. Pototsky, M. Bestehorn, D. Merkt, and U. Thiele, “Morphology changes in the evolution of liquid two-layer films.,” J. Chem. Phys. **122**(22), 224711 (2005).

[153] T. Maxworthy, J. Leilich, J.E. Simpson, and E.H. Meiburg, “The propagation of a gravity current into a linearly stratified fluid,” J. Fluid Mech. **453**, (2002).

[154] A.Z. Szeri, *Fluid Film Lubrication- Theory and Design* (Cambridge University Press, Cambridge, 1998).

[155] J.H. Snoeijer, "Free-surface flows with large slopes: Beyond lubrication theory," Phys. Fluids **18**(2), 021701 (2006).

[156] K. Mahady, S. Afkhami, J. Diez, and L. Kondic, "Comparison of Navier-Stokes simulations with long-wave theory: Study of wetting and dewetting," Phys. Fluids **25**(11), 112103 (2013).

[157] J.H. Snoeijer and B. Andreotti, "Moving Contact Lines: Scales, Regimes, and Dynamical Transitions," Annu. Rev. Fluid Mech. **45**(1), 269 (2013).

[158] L. Lacaze, P. Guenoun, D. Beysens, M. Delsanti, P. Petitjeans, and P. Kurowski, "Transient surface tension in miscible liquids," Phys. Rev. E - Stat. Nonlinear, Soft Matter Phys. **82**(4), 041606 (2010).

[159] M.S.P. Stevar and a. Vorobev, "Shapes and dynamics of miscible liquid/liquid interfaces in horizontal capillary tubes," J. Colloid Interface Sci. **383**(1), 184–197 (2012).

[160] A. Vorobev, "Dissolution dynamics of miscible liquid/liquid interfaces," Curr. Opin. Colloid Interface Sci. **19**(4), 300–308 (2014).

[161] P. Petitjeans and T. Maxworthy, *Miscible displacements in capillary tubes. Part 1. Experiments*, J. Fluid Mech. **326**, 37 (1996).

[162] C. Huh and L.. Scriven, *Hydrodynamic model of steady movement of a solid/liquid/fluid contact line*, J. Colloid Interface Sci. **35**, 85–101 (1971).

[163] E.B. Dussan V. and S.H. Davis, *On the motion of a fluid-fluid interface along a solid surface*, J. Fluid Mech. **65**, 71 (1974).

[164] L.H. Tanner, *The spreading of silicone oil drops on horizontal surfaces*, J. Phys. D. Appl. Phys. **12**(9), 1473–1484 (1979).

[165] R.B. Bird, W.E. Stewart, and E.N. Lightfoot, *Transport Phenomena* (John Wiley & Sons, New York, 2007).

[166] Z. Wu, J. Zhao, J. Yin, and H. Li, *Nonlinear Diffusion Equation* (World Scientific, Singapore, 2001).

[167] L.A. Baughman and N.J. Walkington, “Co-volume methods for degenerate parabolic problems,” Numer. Math. **64**, 45 (1993).

[168] L.E. Stillwagon and R.G. Larson, “Fundamentals of topographic substrate leveling,” J. Appl. Phys. **63**, 5251 (1988).

[169] J. Gratton and F. Minotti, *Self-similar viscous gravity currents: phase-plane formalism*, J. Fluid Mech. **210**, 155 (1990).

[170] S. Betelú, J. Diez, L. Thomas, R. Gratton, and B. Marino, “A boundary element method for viscous gravity currents,” Int. J. Numer. Methods Fluids **25**, 1–19 (1997).

[171] E.R. Peterson and M. Shearer, “Simulation of spreading surfactant on a thin liquid film,” Appl. Math. Comput. **218**, 5157 (2012).

[172] R.J. Cornish, “Flow in a pipe of rectangular cross-section,” Proc. R. Soc. A **120**, 691 (1928).

[173] M.E. Charles and L.U. Lilleleht, “Co-current stratified laminar flow of two immiscible liquids in a rectangular conduit,” Can. J. Chem. Eng. **43**, 110 (1965).